Department of Precision and Microsystems Engineering

OPTOTHERMALLY EXCITED PARAMETRIC RESONANCE IN MONOLAYER GRAPHENE NANODRUM RESONATORS

Abhilash Chandrashekar

Report no	: 2017.035
Coach	: Dr. Farbod Alijani & Ir. R.J.Dolleman
Professor	: Dr. Peter G. Steeneken
Specialisation	: Dynamics of Micro and Nano Systems
Type of report	: MSc Thesis
Date	: 28 August 2017

OPTOTHERMALLY EXCITED PARAMETRIC RESONANCE IN MONOLAYER GRAPHENE NANODRUM RESONATORS

by

Abhilash Chandrashekar

in partial fulfillment of the requirements for the degree of

Master of Science

in Mechanical Engineering

at the Delft University of Technology,

to be defended publicly on Monday August 28 at 11.30 a.m.

Supervisor:	Dr. ir. F. Alijani	
	Ir. R.J.Dolleman	
Thesis committee:	Prof. dr. P. G Steeneken,	TU Delft
	Prof.dr. A. V. Metrikine,	TU Delft
	Dr. ir. M. K. Ghatkesar	TU Delft

An electronic version of this thesis is available at `http://repository.tudelft.nl/`.

TU Delft Delft
University of
Technology

ABSTRACT

Ever since its inception, graphene has been the subject of research in many parts of the world. This is due to its exceptional mechanical and electrical properties, which makes it ideal for NanoElectroMechanical (NEMS) devices. The inherent nature of NEMS devices, includes low damping, large amplitudes of oscillation, resonant operating conditions, and the presence of nonlinear force fields. This sets an ideal stage for the appearance of nonlinear behavior. In this thesis, appearance of such nonlinear behavior in optothermally actuated graphene nanodrum resonators is studied. Frequency response arising from parametric excitation is explained based on, time modulated stiffness due to temperature variation in the membrane. Also, the response arising from direct excitation is discussed based on initial geometric imperfection present in the membrane. In order to explain the nonlinear response seen in graphene resonators, novel analytical models are developed and its corresponding limitations are discussed. A single differential equation is used to simulate the behavior of both directly and parametrically excited graphene nanoresonator. This equation is used to study the influence of nonlinear damping on response of the system. Then, an illustration is provided on characterization of graphene properties from the parametric response of the system. Finally, it is concluded that, alternative damping mechanism and other physical phenomena could be influencing the system dynamics. Therefore, modeling of these phenomena would lead to better matching of the experimental results.

CONTENTS

1

INTRODUCTION

1.1. ATOMICALLY THIN MATERIALS

The unexpected discovery of graphene in the year 2004 [1], changed the perception that, atomically thin materials could not be sustained in a free standing state. Today, Two dimensional (2D) topological materials, sometimes referred to as single layer materials, are defined as crystalline materials consisting of a single layer of atoms. Since the isolation of graphene, a large amount of research has been directed at isolating other 2D materials. The research interest stems from their unusual characteristics and the promise they show for applications as diverse as electronics, valleytronics, catalysis, water purification and biosensing [2–6].

Currently, graphene is at the helm of all the research on 2D materials. Due to its exceptional properties, it is one of the most extensively researched nanomaterial in the scientific community. It consists of sp^2 bonded monolayer of carbon atoms as shown in Figures 1.1 (a) & (b), which results in a honeycomb lattice. Graphene can exist as a free standing material because of the strong interatomic bonds. Also, crumpling of graphene in the third dimension reduces the overall free energy [7, 8]. Graphene possesses remarkable electronic properties [9], including ultrahigh electron mobility. The combination of its electronic properties and its two-dimensional geometry make it useful for a number of technologies, including chemical sensors, flexible and transparent electrodes and high-frequency analog transistors [2, 9–13]. In addition to its electronic properties, graphene has unique mechanical properties. It is the strongest material ever measured, with a breaking strain of nearly 25%, and it is among the stiffest known materials, with a Young's modulus of 1 TPa [14]. For graphene, electronics applications, sensor applications and nanomechanical device applications are at the forefront of ongoing research.
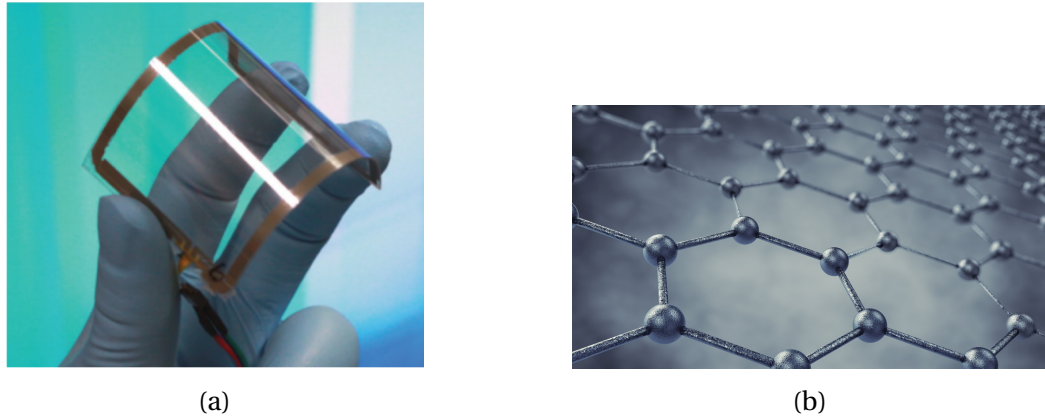
Figure 1.1: (a)A flexible touch panel made by patterning silver paste onto graphene [13] (b) An artists impression of honeycomb lattice in graphene [15]

1.2. APPLICATIONS OF GRAPHENE IN NEMS

Graphene has attracted great research interests in recent years for various potential applications due to its unique mechanical, electrical, optical and chemical properties. The large surface area-to volume ratio of graphene make them prime candidates for applications in MEMS and NEMS devices.

Specifically, graphene-based electromechanical resonators have been demonstrated by using suspended graphene structures over silicon oxide trenches as shown in Figure 1.2 (d). Figure 1.2 (a) illustrates this concept [16]. Similarly, graphene-based devices can be utilized as gas sensors to sense the frequency shift due to absorption of gases. This is illustrated in Figure 1.2 (c) . Other works have extended the investigations by using graphene resonators to electrically transduce signals to sense mass, tension and charge concurrently [17]. Specifically, the best experimental results in graphene-based mass sensor show good sensing capability of 1 zg (10^{-21} g), while the theoretical analyses indicate that graphene could achieve the sensitivity of yg (10^{-24} g) [18, 19]. Furthermore, there has been extensive research into graphene pressure sensors due to its near impermeability to gases [20], Figure 1.2 (b) shows a graphene based LSG pressure sensor. In addition to the aforementioned graphene sensors based on mechanical resonators, graphene-based chemiresistors and field effect transistors have also been utilized for gas sensing applications since, the resistance of graphene is sensitive to gas molecules.
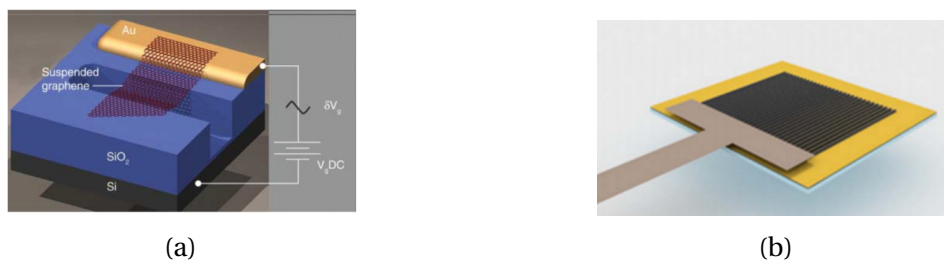
Figure 1.2: (a) Suspended graphene resonator [16] (b) Graphene pressure sensor [21] (c) Graphene based NO_2 gas sensor [22] (d) SEM image of suspended graphene resonator with electrical contacts [18]

1.3. Sources of Nonlinearity

In this section, the source of nonlinearities in MEMS and NEMS devices is discussed briefly [23]. It is important from modeling and experimental point of view to distinguish the origin of nonlinearities seen in the response curves. This helps in understanding the influence of nonlinearities on the system dynamics.

1. Material Nonlinearity
   The most straightforward nonlinearity encountered in the MEMS and NEMS devices is the material nonlinearity and it occurs when the relation between stress and strains are not linear anymore. Continuum solid mechanics dictates that for small deformations, stress and strain are related through the Young's modulus. However, when strain becomes larger, this ratio is modified and plasticity occurs [24]. When translated to macroscopic deformations, material nonlinearity implies that the stiffness of the structure will depend on the deformation and thus, the equation of motion will not be linear anymore.

2. Geometric Nonlinearity
   This is the most important nonlinearity that is seen in many MEMS and NEMS devices. It is associated with the geometry and boundary conditions of the resonator itself. This type of nonlinearity is seen mostly in devices operating in large amplitude flexural modes [25–27]. For example, in a clamped-clamped beam, the geometric nonlinearity arises in the form of effective stiffness of the mode, caused by an increase in the longitudinal tension due to motion [26]. In other type of flexural devices, e.g. clamped-free beams or cantilevers, it can be seen that there are also inertial nonlinear terms that affect the effective mass [28].

3. Actuation Nonlinearity
   The next source of nonlinearity to be analyzed here is the one emerging from a nonlinear dependence on the displacement of the actuation force[26, 29]. It can be understood from the point of view of an actuation force that modifies the potential well of the harmonic oscillator. This example is found quite commonly in MEMS/NEMS resonators as, it is inherent to electrostatic actuation.

4. Detection Nonlinearity
   A majority of MEMS and NEMS devices employ an electrostatic or optical detection setup to read the motion of the resonator. Naturally, due to optical transduction, cross talk between signals, circuit noise etc, it introduces a nonlinearity into the measured

signal. This nonlinearity does not affect the dynamics of the resonator. It affects the conversion of actual displacement and the measured signal (voltage or current) in the laboratory equipment. This type of nonlinearity becomes very important when determining the actual nonlinear parameters of the system [28, 30].

5. Nonlinear damping

   In many mechanical structures, the dissipation is considered linear, i.e a constant no matter the displacement. However, in reality there is no theoretical deterrent for the damping to be nonlinear in nature[18, 26, 31, 32]. The origins of nonlinearity are still unclear and remain as one of the most interesting field of fundamental research.

1.4. RESEARCH OBJECTIVE

As discussed in the previous sections, graphene is an extremely flexible material with exceptional material properties. This has piqued the interest of the research community to explore these properties and apply them in novel applications like sensing [17, 18], data storage [33], energy storage [34] etc. Due to geometric nonlinearities, the tension in circular graphene membranes is strongly amplitude dependent, which makes graphene susceptible to nonlinear behaviors. This thesis focuses on large amplitude response of the resonance modes in circular graphene nanodrum resonators. There are subharmonic and superharmonic resonances at twice and half the natural frequency as shown in Figure 1.3. While one of the explanation for the resonances could be parametric excitation due to changes in tension, they are not expected to be observed in a homodyne detection scheme. Furthermore, the source of direct excitation which is seen in Figure 1.3 is unknown. Therefore, this thesis aims at building analytical models to predict such nonlinear behavior in graphene resonators and carefully delineate the underlying physics causing this nonlinear phenomena.
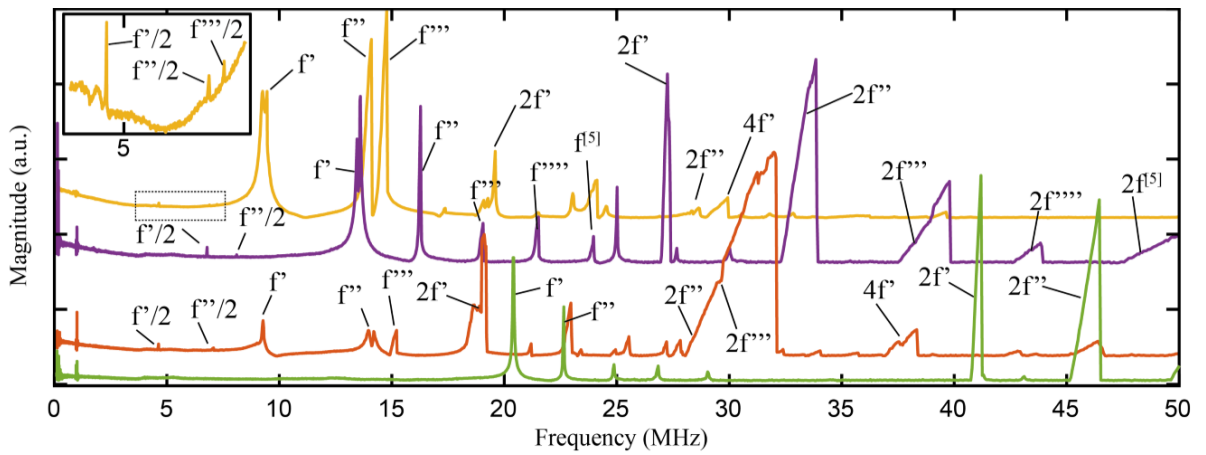
Figure 1.3: Experimental curves of 4 different graphene nanodrum resonators.

1.5. EXPERIMENTAL SETUP

To probe the motion of nanoscale mechanical devices such as graphene nanoresonators, an optical interferometer based on a Fabry-Perot cavity is used as a fast characterization tool [35]. The technique works as follows: the motion of suspended graphene in the cavity is

detected using a probe laser. A second intensity modulated driving laser is used to drive the graphene drums housed in a vacuum chamber as shown in Figure 1.4. The advantage of this probe configuration is a high frequency bandwidth and no need for on-chip electrodes for driving and detection of the drum motion. This is in contrast to an electrostatic mixing technique in which, each drum needs to be contacted separately and driven by a gate voltage underneath it [16, 36]. In this section, a brief explanation is given on the interferometer setup and the optothermal actuation technique. Figure 1.5 shows the experimental setup containing different optical elements that are used to form the interferometer setup and also the lasers used for actuating the graphene resonators. The optical read out is analyzed by a Vector Network Analyzer (VNA).
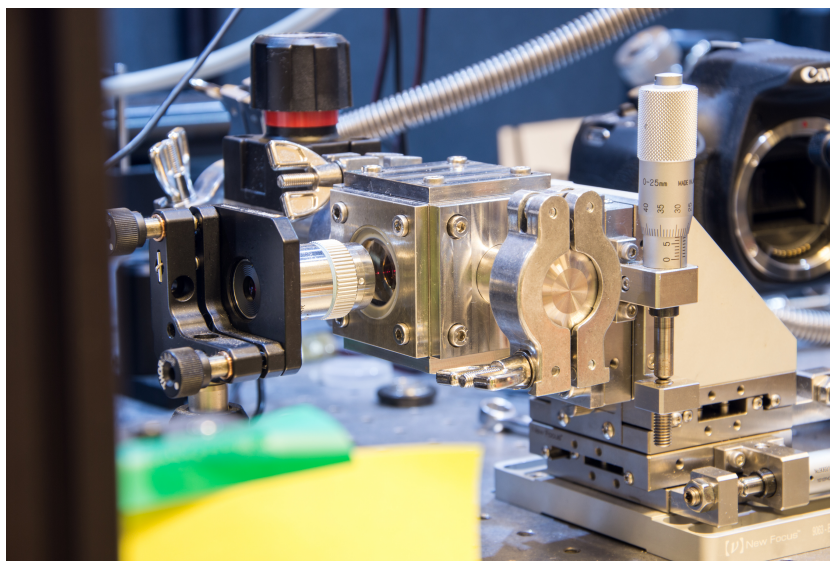
Figure 1.4: Vaccum chamber housing monolayer graphene nanodrum resonators at 10^{-6} milli bar pressure. The chamber is placed on a X-Y-Z translating stage.
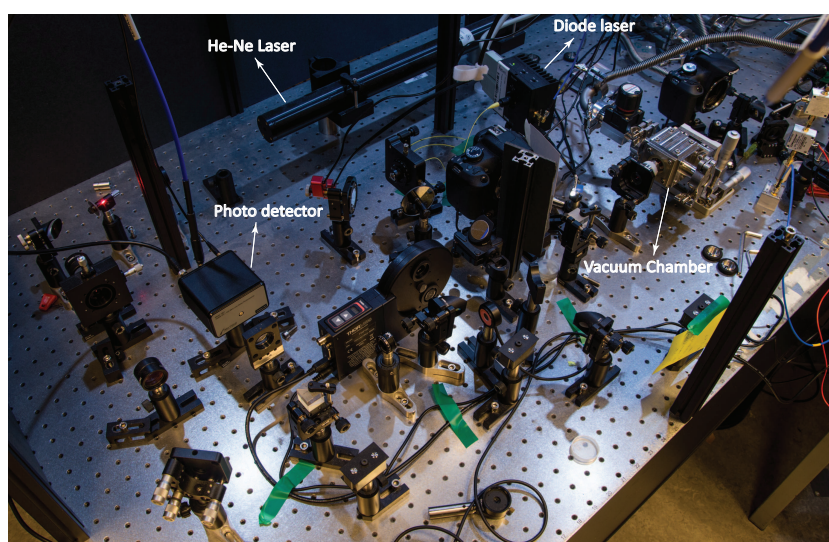
Figure 1.5: Experimental setup with labels indicating the major components. The other optical paraphernalia seen in the figure includes optical mounts, dichroic mirror, beam splitters which are not labelled. These are used for directing and reading the laser signal from the graphene membrane.

1.5.1. OPTOMECHANICAL CAVITY

The motion detection technique is based on the interference of two bundles of reflected light in a Faby-Perot interferometer setup. In this configuration, both mirrors are placed after each other in one path, forming an optical cavity. The first (front) mirror is partly reflective, such that part of the light passes to the second (back) mirror and part of the light is reflected by the first mirror. The part of the light that passed through the first mirror is now reflected from the second (back) mirror. The two rays of reflected light coming from the front mirror and back mirror then interfere with each other. Depending on the distance between both mirrors, the interference can be constructive, destructive or somewhere between these two extreme cases. In this configuration, the reflectivity of the Fabry-Perot interferometer depends on the distance between the two mirrors. By making the front mirror movable, the reflectivity is coupled to the motion of the front mirror, and becomes a displacement detector via the variation in reflectivity due to the movable mirror. Figure 1.6 shows the schematic of a Fabry-Perot cavity formed by a suspended 2D-layered graphene nanodrum (front mirror) on top of the silicon substrate (back mirror). The length of the optical cavity formed is approximately 300 nm.
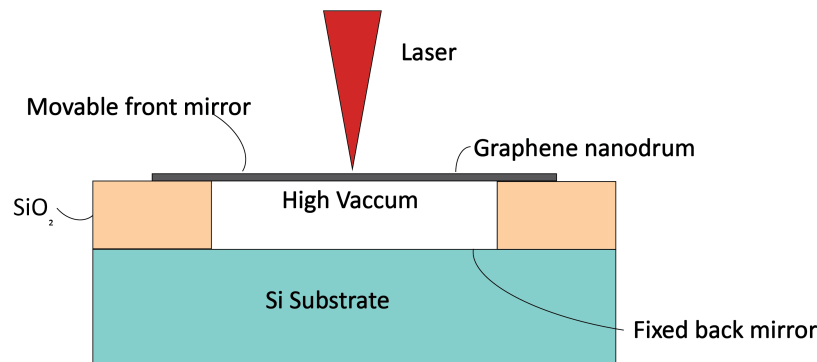
Figure 1.6: Optomechanical cavity showing the graphene membrane acting as a front mirror and Si substrate as back mirror. He-Ne red laser is used for motion readout.

1.5.2. INTERFEROMETER SETUP

Figure 1.7 shows a schematic overview of the interferometer setup used to detect the motion of graphene nanodrum resonators. Drum motion is probed using a 1.2 mW linearly polarized Helium Neon laser, λ = 633 nm, whose output power is attenuated by a neutral density filter (NDF). The beam is expanded (3x) using two lenses, to match the aperture of the objective lens. Before hitting the sample, the light passes through a polarizing beam splitter (PBS) and a quarter wave plate ($\lambda/4$). The reflected light passes again through the $\lambda/4$ plate and is directed by the PBS onto the photodetector. To drive the drum resonators at the resonance frequency, a photothermal excitation technique is used. To apply this technique, light from a blue diode laser of power 0.36 mW with an rf-modulated intensity, is coupled via the dichroic mirror (DM). The resonator is placed in a small vacuum chamber with a transparent window. The transmission gain of the blue laser modulation to the signal detected by the photodetector is measured by a Vector Network Analyzer (VNA). This VNA is equipped with the ability to perform frequency conversion measurements, hence both homodyne and

heterodyne detection schemes can be performed on this setup by directly connecting to the diode laser and photodetector. This is used to detect direct and parametric resonances. Finally, to enable positioning of the blue and red laser foci onto the nanodrum resonators, the vacuum chamber is mounted onto an xyz position manipulating stage. During the alignment, the position of the drums and laser spots are monitored using a CCD camera and LED illumination.
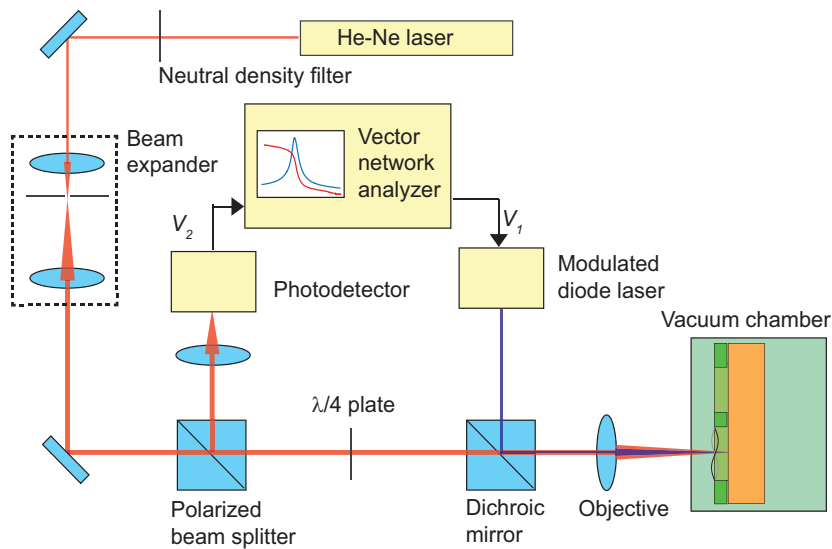
Figure 1.7: Schematic showing the interferometer setup. The setup shows the blue diode laser used for actuating the membrane and a red He-Ne laser used to detect the motion of the membrane.

1.5.3. OPTOTHERMAL ACTUATION

As discussed in the previous subsection, a blue diode laser is used for driving the drum resonators. The output power of the laser is modulated with an rf-signal. When the light is incident on the resonator, it results in a periodic heating and cooling of the drum, which yields a vibrational motion at the driving frequency. The limit of applicability of this technique is determined by the heat capacity of the drum resonator and the thermal conductivity. These parameters are connected via the thermal diffusivity, which tells how fast a temperature difference is smoothed out over the membrane.

1.6. SYNTHESIS OF GRAPHENE NANODRUMS

Single-layer graphene resonators are fabricated on top of 300 nm deep SiO_2 in the form of dumbbell-shaped cavities as shown in Figure 1.8 (a). Cavities are etched in a layer of silicon dioxide in a dumbbell shape, where the graphene is directly transferred on top 1.8 (b). Single layer graphene grown by chemical vapor deposition is transferred over both chips covered with a protective polymer 1.8 (c). This polymer is dissolved and the sample is dried using critical point drying (CPD) with liquid carbon dioxide. The fluid forces in this process break one half of the dumbbell, creating a resonator on the other half with a venting channel. This lets the gas below the membrane escape in the vacuum chamber when the sample is purged 1.8 (d). The graphene is further characterized by Raman spectroscopy and Atomic Force Microscopy (AFM) to confirm it as single layer. For more details on the fabrication

and transfer process, the reader is directed to reference [37]. Figure 1.8 (e) & (f) shows the SEM image of graphene nanodrum resonators with venting channel.
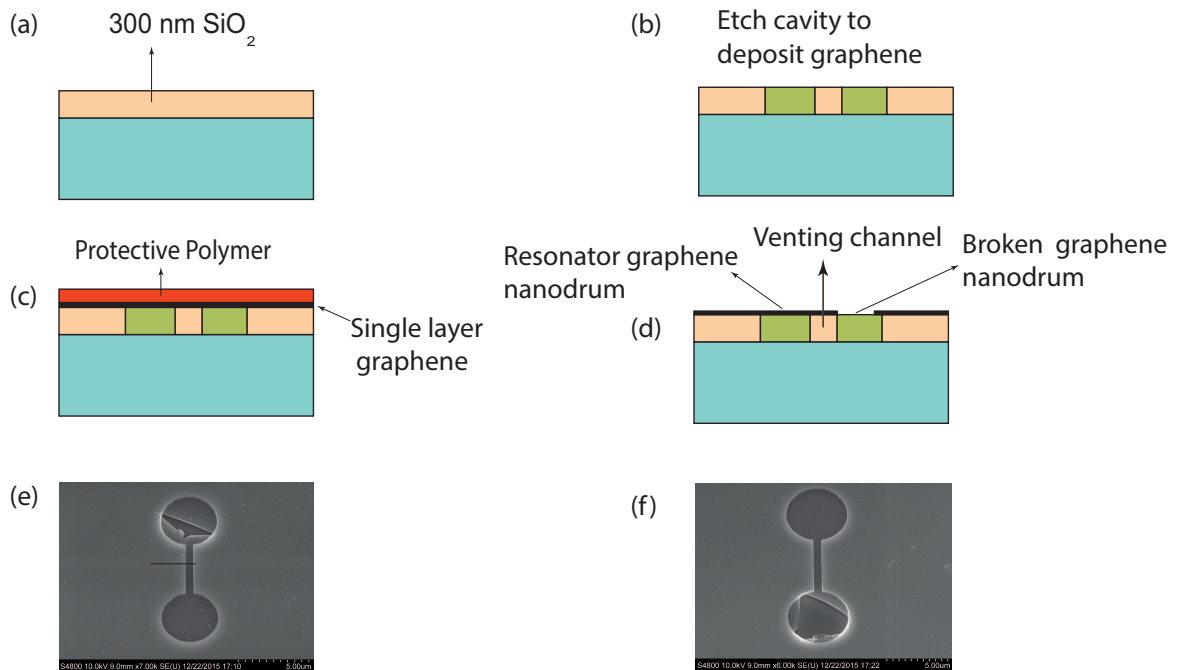
Figure 1.8: Steps involved in fabricating graphene circular nanodrum resonator.

1.7. CONCLUSION

In this chapter, the importance of graphene and its applications in nanomechanical devices were discussed briefly. The peculiar behavior of graphene nanodrum resonators subjected to opthothermal actuation is introduced and the corresponding experimental curves were discussed. The objective of the thesis is introduced based on the aforementioned experimental curves. Detailed explanation of the experimental setup and the type of actuation used for conducting experiments is provided. Furthermore, the physics and design of a optical interferometer to measure the motion of resonators based on two-dimensional materials like graphene is explained. Finally, a brief insight is provided into the synthesis of graphene nanodrum resonators.

2

NONLINEAR MECHANICS OF MEMBRANES

In order to accomplish the research goal of understanding nonlinearities in graphene, it is necessary to derive a mathematical model that can explain the dynamics of graphene nanoresonators. To meet this end, this chapter begins by discussing the nonlinear strain-displacement relations arising from geometric nonlinearities. These equations are further extended to develop an axisymmetric model, which is used to explain the dynamics of circular drum graphene nanoresonators through out the bulk of this dissertation.

2.1. NONLINEAR STRESS AND STRAIN RELATIONS

A membrane behaves nonlinearly when the tension induced by external forces are comparable to, or larger than the pretension in the membrane. The stress and strain relations shown in this section closely follow references [38, 39].

2.1.1. KINEMATIC EQUATIONS
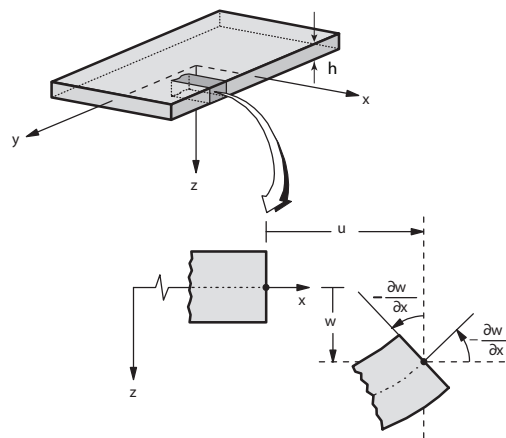
Figure 2.1: Undeformed and deformed geometries of an membrane under kirchhoff assumptions [38].

Consider a membrane of uniform thickness h as shown in Figure 2.1. We shall use the rectangular Cartesian coordinates (x, y, z) with the xy-plane, coinciding with the geometric

middle plane of the membrane. Let (u_x, u_y, u_z) denote the total displacements of a point along the (x, y, z) coordinates. Then, the kinematic equations are obtained based on the Kirchhoff's hypotheses for plates. Among these hypotheses, an important kinematic assumption is that, the straight lines initially normal to the middle plane before bending, remain straight and normal to the middle surface during the deformation and the length of such elements is not altered. This means that the vertical shear strains ϵ_{xz} and ϵ_{yz} are negligible and the normal strain ϵ_z may also be omitted. These assumptions lead to the following displacement relations,

$$
\begin{aligned}
u_x(x, y, z, t) &= u(x, y, t) - z\frac{\partial w}{\partial x} \\
u_y(x, y, z, t) &= v(x, y, t) - z\frac{\partial w}{\partial y} \\
u_z(x, y, z, t) &= w(x, y, t)
\end{aligned}
$$
(2.1)

The strain components are defined by the Lagrange-strain tensor,

$$
\epsilon_{ij} = \frac{1}{2}\left[\frac{\partial U_i}{\partial X_j} + \frac{\partial U_j}{\partial X_i} + \frac{\partial U_k}{\partial X_i}\frac{\partial U_k}{\partial X_j}\right]
$$
(2.2)

Where U and X are vectors with components,

$$
\begin{aligned}
U &= (u_x, u_y, u_z) \\
X &= (x, y, z)
\end{aligned}
$$

Substituting equation 2.1 into equation 2.2, we obtain the nonlinear strain-displacement relations. If the components of the displacement gradients are of the order ζ i.e,

$$
\frac{\partial u_x}{\partial x}, \frac{\partial u_x}{\partial y}, \frac{\partial u_y}{\partial x}, \frac{\partial u_y}{\partial y}, \frac{\partial u_z}{\partial z} = \mathcal{O}(\zeta)
$$

Then, the small strain assumption implies that terms of the order $\mathcal{O}(\zeta^2)$ are omitted in the strain equations. Unless the rotation of the transverse normals are moderate (10°-15°). In such a case the following terms are not negligible when compared with terms of order $\mathcal{O}(\zeta)$.

$$
\left(\frac{\partial w}{\partial x}\right)^2, \left(\frac{\partial w}{\partial y}\right)^2, \left(\frac{\partial w}{\partial x}\frac{\partial w}{\partial y}\right)
$$

Then, the strain-displacement relations become,

$$
\begin{aligned}
\epsilon_{xx} &= \frac{\partial u}{\partial x} + \frac{1}{2}\left(\frac{\partial w}{\partial x}\right)^2 - z\left(\frac{\partial^2 w}{\partial x^2}\right) \\
\epsilon_{yy} &= \frac{\partial v}{\partial x} + \frac{1}{2}\left(\frac{\partial w}{\partial y}\right)^2 - z\left(\frac{\partial^2 w}{\partial y^2}\right) \\
\epsilon_{xy} &= \frac{1}{2}\left(\frac{\partial u}{\partial y} + \frac{\partial v}{\partial x} + \frac{\partial w}{\partial x}\frac{\partial w}{\partial y} - 2z\frac{\partial^2 w}{\partial x\partial y}\right) \\
\epsilon_{xz} &= 0 \\
\epsilon_{yz} &= 0 \\
\epsilon_{zz} &= 0
\end{aligned}
$$
(2.3)

The equations 2.3 are called *'Von Kármán Strains'*. The strains in equation 2.3 can be represented as a sum of membrane and bending strains given by,

$$\epsilon_{xx} = \epsilon_{xx}^m + \epsilon_{xx}^b$$
$$\gamma_{xy} = 2\epsilon_{xy} = \gamma_{xx}^m + \gamma_{xx}^b \quad (2.4)$$
$$\epsilon_{yy} = \epsilon_{yy}^m + \epsilon_{yy}^b$$

where the strains of the middle surface, $(\epsilon_{xx}^m, \epsilon_{yy}^m, \gamma_{xy}^m)$, are called the membrane strains, and $(\epsilon_{xx}^b, \epsilon_{yy}^b, \gamma_{xy}^b)$ are the flexural (bending) strains, known as the curvatures. It is important to note that, for a membrane element, the bending strains are absent mainly due to zero or negligible bending rigidity (D).

2.1.2. CONSTITUTIVE EQUATIONS

Assuming a linear stress-strain relationship, the constitutive equations are defined by generalized Hooke's law. Consider a membrane element with pretension n_0 per unit length and temperature distribution in the membrane governed by equation 2.5.

$$k\nabla^2\Delta T + Q = \rho c_p \frac{\partial \Delta T}{\partial t} + \frac{E\alpha\Delta T}{1-2\nu}\frac{\partial e}{\partial t} \quad (2.5)$$

Where, ΔT = T - T$_\infty$ is the change is temperature with respect to the ambient temperature (T$_\infty$), e is the dilatation strain caused by thermal effect, E is the Young's modulus, α is the thermal expansion coefficient, ν is Poisson's ratio, ρc_p is the thermal capacitance and Q is the external heat flux.

Then the stress-strain relations are given by,

$$\begin{bmatrix} \sigma_{xx} \\ \sigma_{yy} \\ \sigma_{xy} \end{bmatrix} = \frac{E}{(1-\nu^2)} \begin{bmatrix} 1 & \nu & 0 \\ \nu & 1 & 0 \\ 0 & 0 & 1-\nu \end{bmatrix} \begin{bmatrix} \epsilon_{xx} \\ \epsilon_{yy} \\ \epsilon_{xy} \end{bmatrix} - E\alpha \begin{bmatrix} \Delta T \\ \Delta T \\ 0 \end{bmatrix} + \begin{bmatrix} \sigma_0 \\ \sigma_0 \\ 0 \end{bmatrix} \quad (2.6)$$

where, σ_0 is the stress due to intial tension n_0. The above equations for stress and strains are used in the Lagrange formulation to obtain the equations of motion in the subsequent chapters.

2.1.3. AXISYMMETRIC MODEL OF CIRCULAR MEMBRANE

Consider a circular membrane of radius *'a'*, let the r-coordinate be taken radially outward from the center of the membrane, z-coordinate along the thickness (or height) of the plate, and the θ-coordinate be taken along a circumference of the membrane, as shown in Figure 2.2.

The displacement field from the classical plate theory [39] is given by,

$$u_r(r,\theta,z,t) = u(r,\theta,t) - z\frac{\partial w}{\partial r}$$
$$u_\theta(r,\theta,z,t) = v(r,\theta,t) - \frac{z}{r}\frac{\partial w}{\partial \theta} \quad (2.7)$$
$$u_z(r,\theta,z,t) = w(r,\theta,t)$$
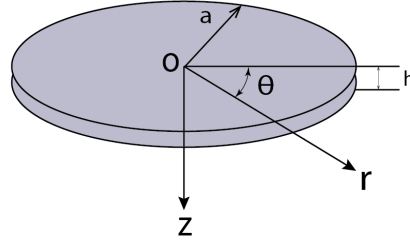
Figure 2.2: Membrane element

The admissible functions for the displacement fields (u_r, u_θ, u_z) are given by the linear mode shapes of the membrane. These derivation of these modeshapes are shown in appendix A. The nonlinear strains are given by equation 2.3. Ignoring the bending strains and accounting only for the *Von Kármán* nonlinearity (i.e., neglecting all nonlinear terms except for those involving only u_z), and also incorporating the strain $\alpha \Delta T$ due to thermal load, we obtain the below strain equations for a perfectly flat membrane,

$$\epsilon_r = \frac{\partial u}{\partial r} + \frac{1}{2}\left(\frac{\partial w}{\partial r}\right)^2 + \alpha \Delta T$$

$$\epsilon_\theta = \frac{1}{r}\frac{\partial v}{\partial \theta} + \frac{u}{r} + \frac{1}{2}\left(\frac{\partial w}{r\partial \theta}\right)^2 + \alpha \Delta T \tag{2.8}$$

$$\gamma_{r\theta} = \frac{\partial v}{\partial r} - \frac{v}{r} + \frac{1}{r}\frac{\partial u}{\partial \theta} + \left(\frac{\partial w}{\partial r}\right)\left(\frac{\partial w}{r\partial \theta}\right)$$

For an axisymmetric model, the loads are assumed to be rotationally symmetric making the system independent of the θ-coordinate. Thus, the above system of equations reduces to,

$$\epsilon_r = \frac{\partial u}{\partial r} + \frac{1}{2}\left(\frac{\partial w}{\partial r}\right)^2 + \alpha \Delta T$$

$$\epsilon_\theta = \frac{u}{r} + \alpha \Delta T \tag{2.9}$$

$$\gamma_{r\theta} = 2\epsilon_{r\theta} = 0$$

where,
α = Thermal expansion coefficient in K^{-1}.
ΔT = T- T_0 , T_0 being the ambient temperature in K.
Solving for the stresses we have [40],

$$\sigma_r = \frac{E}{1-v^2}\left((\epsilon_r + v\epsilon_\theta) - \alpha(1+v)\Delta T\right) + \sigma_0$$

$$\sigma_\theta = \frac{E}{1-v^2}\left((\epsilon_\theta + v\epsilon_r) - \alpha(1+v)\Delta T\right) + \sigma_0 \tag{2.10}$$

$$\sigma_{r\theta} = \frac{E}{2(1+v)}\gamma_{r\theta} = 0$$

The stresses σ_{ij} and the forces acting on the system n_{ij} are related by the equation,

$$n_{ij} = \int_{-\frac{h}{2}}^{\frac{h}{2}} \sigma_{ij} dz \tag{2.11}$$

Where h is the thickness of the membrane. Using equation 2.11 and 2.10 we have,

$$n_r = \frac{Eh}{1-v^2}\Big((\epsilon_r + v\epsilon_\theta) - \alpha(1+v)\Delta T\Big) + n_0$$

$$n_\theta = \frac{Eh}{1-v^2}\Big((\epsilon_\theta + v\epsilon_r) - \alpha(1+v)\Delta T\Big) + n_0 \tag{2.12}$$

$$n_{r\theta} = \frac{Eh}{2(1+v)}\gamma_{r\theta} = 0$$

Where, n_0 denotes initial tension.

Assuming only an external load 'P$_z$' acting perpendicular to the plane of the membrane, we can derive the equilibrium equations from Figure 2.3 and are given by,
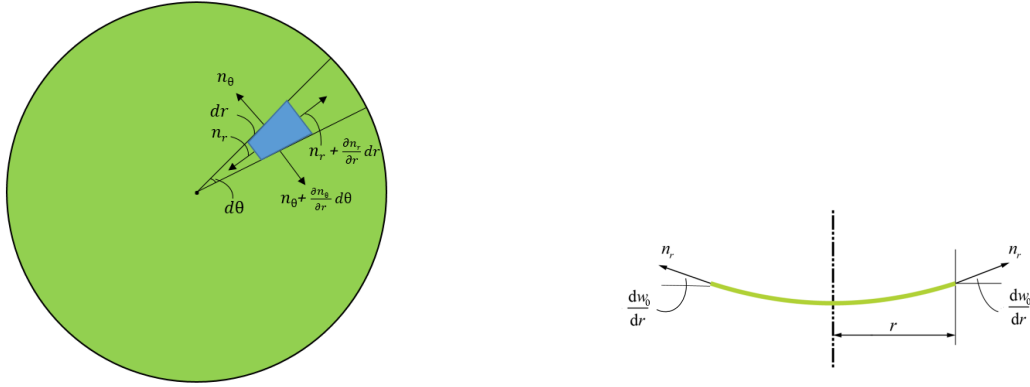
Figure 2.3: Forces acting on a circular membrane [20].

By projecting the forces in radial (r) direction one can obtain:

$$r\frac{dn_r}{dr} - n_\theta + n_r = 0 \tag{2.13}$$

By projecting the forces in transverse (z) direction one can obtain:

$$\nabla n_r \frac{\partial w}{\partial r} + P_z = \rho h \frac{\partial^2 w}{\partial t^2} \tag{2.14}$$

2.1.4. Membrane with Initial Geometric Imperfection

In the previous section, we considered the mechanics of a perfectly flat membrane and derived the stress-strain relations. In this section, the membrane is assumed to possess an initial geometric imperfection for which the kinematic relations are derived [41],

The transverse displacement (u_z) is modified to incorporate the additional imperfection term given by $w_0(r,\theta,t)$ as follows,

$$u_z(r,\theta,z,t) = w(r,\theta,t) + w_0(r,\theta,t) \tag{2.15}$$

$$\epsilon_r = \frac{\partial u}{\partial r} + \frac{1}{2}\left(\frac{\partial w}{\partial r}\right)^2 + \left(\frac{\partial w}{\partial r}\right)\left(\frac{\partial w_0}{\partial r}\right) + \alpha \Delta T$$

$$\epsilon_\theta = \frac{1}{r}\frac{\partial v}{\partial \theta} + \frac{u}{r} + \frac{1}{2}\left(\frac{\partial w}{r\partial \theta}\right)^2 + \left(\frac{\partial w}{r\partial \theta}\right)\left(\frac{\partial w_0}{r\partial \theta}\right) + \alpha \Delta T \qquad (2.16)$$

$$\gamma_{r\theta} = \frac{\partial v}{\partial r} - \frac{v}{r} + \frac{\partial u}{r\partial \theta} + \left(\frac{\partial w}{\partial r}\right)\left(\frac{\partial w}{r\partial \theta}\right) + \left(\frac{\partial w}{\partial r}\right)\left(\frac{\partial w_0}{r\partial \theta}\right) + \left(\frac{\partial w_0}{\partial r}\right)\left(\frac{\partial w}{r\partial \theta}\right)$$

The stresses and the corresponding forces are calculated in the same way as shown in the previous section.

2.2. Conclusion

In this chapter, the detailed derivations of governing equations of motion for clamped circular membranes are discussed. The geometric nonlinearities are introduced in the form of *'Von Kármán Strains'*. Finally, an axisymmetric model is developed in cylindrical coordinates and the concept of geometric imperfection is introduced. The equations developed in this chapter are used in the subsequent part of the thesis to further model a single layer graphene nanoresonator in the form of a mass spring damper system.

<div align="right">

3

</div>

PARAMETRICALLY DRIVEN GRAPHENE NANODRUM RESONATORS

This chapter utilizes the nonlinear equations and admissible functions derived in the previous chapter, to develop an parametrically excited axisymmetric model for graphene nanodrum resonator. The model is developed through a Lagrangian approach and is used to simulate the experimental parametric response seen in Figure 1.3. The chapter begins by explaining the source of parametric excitation, followed by understanding the dynamics of parametrically excited systems and finally numerical simulations to prove the theoretical predictions.

3.1. SOURCE OF PARAMETRIC EXCITATION

The physics behind the parametric excitation seen in Figure1.3 can be explained by looking at the temperature distribution within the membrane. The modulated blue diode laser used for exciting the membrane also acts as a heat source causing a temperature variation within the membrane. This periodic heat source, when modulated at twice the natural frequency of the resonator, causes the tension of the membrane to be modulated giving rise to parametric excitation [42].

The governing differential equation of heat transfer is obtained by assuming that, the resonator heats up due to absorbed laser radiation and cools down according to Newton's law of cooling. A lumped parameter heat model is used to arrive at the differential equation governing the temperature distribution.

From energy balance we have: Rate of accumulation of internal energy + Rate of heat loss to the surroundings = Rate of heating. This is expressed mathematically as,

$$mc_p \frac{dT}{dt} + hA(T - T_\infty) = P_{abs} \cos(\omega t)$$

Where, m is mass of the membrane(kg), c is specific heat capacity($J\,kg^{-1}\,K^{-1}$), h is heat transfer coefficient($W\,m^{-1}\,K^{-2}$), P_{abs} is optical power absorbed by the membrane from the laser

Taking, $dT = (T - T_\infty)$, since T_∞ being the ambient temperature is a constant and also representing $\Delta T = (T - T_\infty)$ the above equation reduces to,

$$\frac{d\Delta T}{dt} + \frac{1}{\tau_{th}}\Delta T = \frac{P_{abs}}{C}\cos(\omega t) \tag{3.1}$$

Where,

$$\tau_{th} = \left(\frac{1}{hA}\right)\left(mc_p\right) = RC$$

τ_{th} is the thermal time constant, R is the thermal resistance and C is the thermal capacitance of the resonator.

In the above governing differential equation, it should be noted that the spatial dependency of the temperature field governed by the term $k\nabla^2 T$ is ignored here. This is due to the fact that, in graphene nano drum resonators, the thermal resistance term R is assumed to be dominated by the interfacial resistance such that, the thermal time constant τ_{th} becomes independent of thermal conductivity k of the graphene [37]. This boundary resistance will cause the formation of a temperature discontinuity at the interface between suspended and supported graphene. Another interesting point to be noted is that, the thermoelastic coupling term $\beta\dot{e}$, with e being the dilatation is ignored in the above equation. This is mainly due to the small strength of such coupling in MEMS and NEMS systems [43].

The solution to differential equation 3.1 is given by,

$$\Delta T = \frac{P_{abs}\tau\,e^{-\frac{t}{\tau_{th}}}\left(\tau_{th}\omega\,e^{t/\tau_{th}}\cos(\omega t) - e^{t/\tau_{th}}\sin(\omega t) - \tau_{th}\omega\right)}{C\left(\tau_{th}^2\omega^2 + 1\right)}$$

The steady state solution is obtained by ignoring the transient terms in the above equation which leads to,

$$\Delta T = \frac{P_{abs}\,\tau_{th}^2\,\omega\cos(\omega t)}{C\,(\tau_{th}^2\omega^2 + 1)} - \frac{P_{abs}\,\tau_{th}\sin(\omega t)}{C\,(\tau_{th}^2\omega^2 + 1)} \tag{3.2}$$

Figure 3.1 shows the plot of coefficients of sine and cosine term of equation 3.2 versus the thermal time constant. From the figure, it is noted that the steady state temperature distribution is dominated by mainly the cosine term. From the experiments, it is also noted that for a 5 micron diameter graphene drum the average thermal time constant is around 100 ns [37]. This allows for further simplification in the temperature field by ignoring the sine term in the temperature distribution expression giving,

$$\Delta T = \frac{P_{abs}\,\tau_{th}^2\,\omega\cos(\omega t)}{C\,(\tau_{th}^2\omega^2 + 1)} \tag{3.3}$$
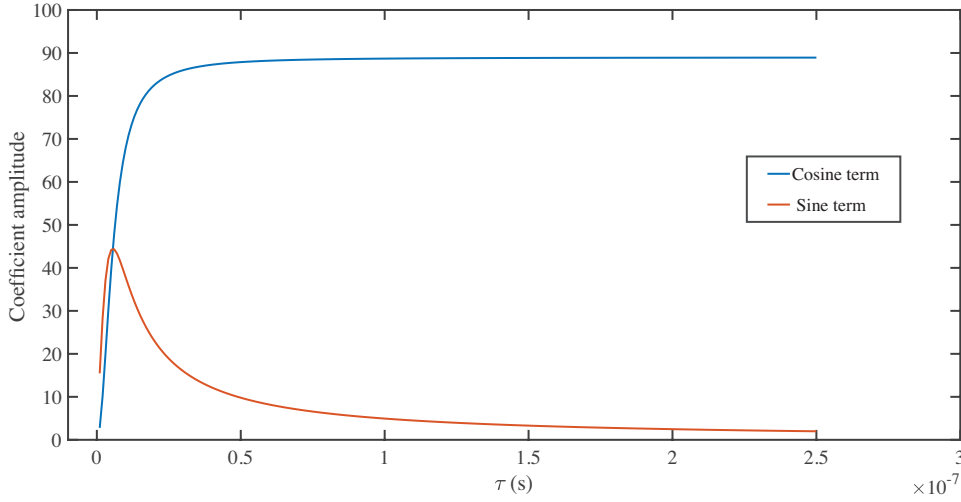
Figure 3.1: Plot showing the strength of coefficients of Cosine and Sine terms versus thermal time constant

3.2. MATHEMATICAL MODELING USING LAGRANGIAN APPROACH

In the subsequent part of this thesis, a Lagrangian approach is used to model the equations of motion. In Lagrangian formulation, the trajectory of a system of particles is derived by solving the Lagrange equations of first or second kind. In each case, a mathematical function called the 'Lagrangian' is formed which is a function of the generalized coordinates, their time derivatives, and the time parameter. The Lagrangian contains the information about the dynamics of the system.

By definition, the Lagrangian is given by,

$$L(q, \dot{q}, t) = T(q, \dot{q}, t) - V(q, t) \tag{3.4}$$

Where, T is the kinetic energy and the V is the potential energy of the system.

Consider a membrane of radius 'a', thickness 'h', thermal expansion coefficient 'α' and temperature change 'ΔT' as shown in Figure 2.2. The equation of motion governing a parametrically excited system is obtained by formulating a Lagrangian of the system as follows,

POTENTIAL ENERGY:

The potential energy of a thermally actuated circular membrane is given by,

$$V = \int_0^{2\pi} \int_0^a \frac{h}{2} \Big(\sigma_r (\epsilon_r - \alpha \Delta T) + \sigma_\theta (\epsilon_\theta - \alpha \Delta T) + \sigma_{r\theta} \gamma_{r\theta} \Big) r \, dr \, d\theta \tag{3.5}$$

The strains $\epsilon_r, \epsilon_\theta, \gamma_{r\theta}$ and stresses $\sigma_r, \sigma_\theta, \sigma_{r\theta}$ are given by equations 2.8 and 2.10 respectively. For an axisymmetric model indeed the shear strain $\gamma_{r\theta} = 0$. The temperature difference ΔT is given by equation 3.3. Furthermore, in order to calculate the potential energy, a set of displacement functions are required which satisfy the clamped membrane boundary conditions.

Admissible Displacement Functions:

For a membrane with fixed edges, the boundary conditions suggest that the displacements u and w should vanish at the boundary. Moreover, the radial displacement field u should disappear at the center of the membrane for continuity and symmetry requirement. Furthermore, assuming only axisymmetric vibration, the tangential displacement is eliminated i.e $v = 0$. Expressing the above requirements mathematically,

$$
\begin{aligned}
u(a, t) &= 0 \\
w(a, t) &= 0 \\
u(0, t) &= 0
\end{aligned}
\tag{3.6}
$$

The displacement fields that satisfy the above requirements are given by,

$$
w = x(t) J_0\left(\alpha_0 \frac{r}{a}\right)
\tag{3.7}
$$

$$
u = u_0 r + r(a - r) \sum_{k=1}^{\bar{N}} q_k(t) r^{k-1}
\tag{3.8}
$$

where, u_0 is the intial displacement obtained from initial tension n_0 given by

$$
u_0 = \frac{\sigma_0(1 - v)}{E}
\tag{3.9}
$$

Here, it should be noted that for axisymmetric vibrations the shear strain $\gamma_{r\theta}$ would be zero. In equation 3.7, x(t) is the generalized coordinate associated with the fundamental transverse mode and q_k(t) are the generalized coordinates associated with the radial displacement. Moreover, J_0 is the Bessel function of order zero, and α_0= 2.40483 for the first vibrational mode shape. In addition, $\bar{N}$ is the number of necessary terms in the expansion of radial displacement.

Kinetic Energy:

The kinetic energy of the membrane is given by:

$$
T = \frac{1}{2} \rho h \int_0^{2\pi} \int_0^a \left(\left(\frac{\partial u}{\partial t}\right)^2 + \left(\frac{\partial w}{\partial t}\right)^2\right) r \, dr \, d\theta
\tag{3.10}
$$

The Lagrange equations of motion are

$$
\frac{d}{dt}\left(\frac{\partial T}{\partial \dot{\mathbf{q}}}\right) - \frac{\partial T}{\partial \mathbf{q}} + \frac{\partial U}{\partial \mathbf{q}} = 0
\tag{3.11}
$$

and $\mathbf{q} = [x(t), q_k(t)], k = 1, ..., \bar{N}$, is the vector including all the generalized coordinates. Equation 3.11 yields a Multi Degree of freedom system of non-linear ordinary differential equations with modulated stiffness and cubic non-linear terms as follows:

$$
\mathbf{M}\ddot{\mathbf{q}} + \mathbf{C}\dot{\mathbf{q}} + \left[\mathbf{K_1} + \mathbf{K_2}\cos(\omega t) + \mathbf{N_3}(\mathbf{q}, \mathbf{q})\right]\mathbf{q} = 0
\tag{3.12}
$$

Where, **M** is the mass matrix and **C** is the viscous damping matrix added to the equations of motion to introduce dissipation. Moreover, **K₁** is the linear stiffness matrix dominated by the tension n_0, **K₂** is the coefficient of the time varying stiffness causing parametric excitation due to temperature variation ΔT. Furthermore, **N₃** denotes the cubic non-linear stiffness terms. It should be noted here the absence of any direct excitation term which indicates that the above equation can be used only to explain the parametric excitation seen in Figure1.3.

A single degree of freedom is more convenient to explain the behavior of single layer graphene resonators. In order to obtain the single degree of freedom model, the above procedure is slightly modified in a way as to include only one degree of freedom in the transverse direction and no inplane modes. To meet this end, the radial displacement field is modified to have only spatial dependency as follows,

$$u = u_0 r + r(a-r)\sum_{k=1}^{\bar{N}} q_k r^{k-1} \tag{3.13}$$

The difference between the MDOF and SDOF model is in the radial displacement field. In the MDOF model a total of $\bar{N}$ in-plane modes were taken with each mode having a temporal dependency given by $q_k(t)$. However, in SDOF model, only spatial distribution is considered and the q_k's are constants which are determined from the condition that the total energy of the membrane for a position of equilibrium is minimum.i.e,

$$\frac{\partial V}{\partial q_k} = 0 \tag{3.14}$$

Once the value of the constants q_k are obtained for $\bar{N}$ terms they are subsituted back into equation 3.13. The kinetic energy of the membrane is now governed by only the transverse displacement:

$$T = \frac{1}{2}\rho h \int_0^{2\pi}\int_0^a \left(\left(\frac{\partial w}{\partial t}\right)^2\right) r\,dr\,d\theta \tag{3.15}$$

The equation of motion is obtained by using the Lagrange equations as follows,

$$\frac{d}{dt}\left(\frac{\partial T}{\partial \dot{\mathbf{x}}}\right) - \frac{\partial T}{\partial \mathbf{x}} + \frac{\partial U}{\partial \mathbf{x}} = 0 \tag{3.16}$$

The above equation yields a single degree of freedom non-linear ordinary differential equation with modulated stiffness and cubic non-linear terms as follows:

EQUATION OF MOTION (SDOF)

$$m\ddot{x} + c\dot{x} + (k + k_p\alpha\Delta T)x + k_3 x^3 = 0$$

Where,

$$\Delta T = \frac{P_{abs}\tau_{th}^2\omega\cos(\omega t)}{C(\tau_{th}^2\omega^2 + 1)}$$

Taking $F_p = k_p \alpha \Delta T$ as the strength of parametric drive we have,

$$F_p = \frac{k_p \alpha P_{abs} \tau_{th}^2 \omega}{C(\tau_{th}^2 \omega^2 + 1)} \tag{3.17}$$

The final equation of motion is reduced to the standard form of a Duffing-Mathieu-Hill differential equation

$$m\ddot{x} + c\dot{x} + (k + F_p \cos(\omega t))x + k_3 x^3 = 0 \tag{3.18}$$

where, $(\ddot{\bullet})$ denotes differentiation with respect to time, m is the mass of resonator and c is the viscous damping added to the equations of motion to introduce dissipation. Moreover, k is the linear stiffness term dominated by the tension n_0, k_p is a constant introduced by the thermal strain term, F_p is the coefficient of the time varying stiffness causing parametric excitation as a matter of temperature variation ΔT. Furthermore, k_3 denotes the cubic non-linear stiffness term introduced by the geometric nonlinearity.

3.3. DYNAMICS OF PARAMETRICALLY EXCITED DUFFING OSCIL-LATOR

The purpose of this section is to analyze the differential equation related to the kinematics formulated in the previous section. The following derivation and the method closely follows references [44, 45]. The solution to the governing differential equation is obtained by using averaging method to cast the governing equation into a system of equations of 'slow' variables.

3.3.1. DYNAMIC ANALYSIS OF EQUATION OF MOTION

The governing differential equation of a resonator with cubic nonlinearity that is parametrically excited is given by Duffing-Mathieu equation as shown by equation 3.19.

$$m\ddot{x} + c\dot{x} + (k + F_p \cos(\omega t))x + k_3 x^3 = 0 \tag{3.19}$$

The above equation is analyzed using standard averaging method to examine the steady state solutions. There are other perturbation techniques like method of multiple scales, method of renormalization etc, that could also be used to solve the nonlinear system [46]. However, the result is the same as shown in this section.

Normalizing equation 3.19 with respect to mass and scaling the time with respect to natural frequency $\tau = \omega_0 t$. Where ω_0 is given by,

$$\omega_0 = \sqrt{\frac{k}{m}}$$

Normalized equation of motion can be obtained as,

$$\ddot{x} + \mu\dot{x} + x + \delta\cos(\Omega\tau)x + \gamma x^3 = 0 \tag{3.20}$$

Definition	Non-dimensional parameter
$(\dot{\bullet}) = \frac{d(\bullet)}{d\tau}$	Scaled time derivative
$\Omega = \frac{\omega}{\omega_0}$	Non-dimensional excitation frequency
$\mu = \frac{c}{2m\omega_0}$	Scaled linear damping coefficient
$\gamma = \frac{k_3}{m\omega_0^2}$	Scaled Nonlinear cubic stiffness coefficient
$\delta = \frac{F_p}{m\omega^2}$	Scaled Parametric excitation amplitude

Table 3.1: Non-dimensional parameter definitions

Assuming the solution of equation 3.20 to be of the form,

$$x = q_1 \cos\left(\frac{\Omega\tau}{2}\right) - q_2 \sin\left(\frac{\Omega\tau}{2}\right) \tag{3.21}$$

Where, q_1 and q_2 are functions of time. The velocity is assumed to be of the form,

$$\frac{dx}{dt} = -\frac{\Omega}{2}\left(q_1 \sin\left(\frac{\Omega\tau}{2}\right) + q_2 \cos\left(\frac{\omega t}{2}\right)\right) \tag{3.22}$$

Substituting equations 3.21 and 3.22 into equation 3.20 and considering each term individually we have,

$$\ddot{x} = L_1(\tau) = -\frac{\Omega}{2}\left(\dot{q}_1 \sin\left(\frac{t\Omega}{2}\right) + \frac{\Omega}{2}q_1 \cos\left(\frac{t\Omega}{2}\right) + \dot{q}_2 \cos\left(\frac{t\Omega}{2}\right) - \frac{\Omega}{2}q_2 \sin\left(\frac{t\Omega}{2}\right)\right)$$

$$\mu\dot{x} = L_2(\tau) = -\mu\frac{\Omega}{2}\left(q_1 \sin\left(\frac{\Omega\tau}{2}\right) + q_2 \cos\left(\frac{\omega t}{2}\right)\right)$$

$$x = L_3(\tau) = q_1 \cos\left(\frac{\Omega\tau}{2}\right) - q_2 \sin\left(\frac{\Omega\tau}{2}\right) \tag{3.23}$$

$$\gamma x^3 = L_4(\tau) = \gamma\left(q_1 \cos\left(\frac{\Omega\tau}{2}\right) - q_2 \sin\left(\frac{\Omega\tau}{2}\right)\right)^3$$

$$\delta\cos(\Omega\tau)x = L_5(\tau) = \delta\cos(\Omega\tau)\left(q_1 \cos\left(\frac{\Omega\tau}{2}\right) - q_2 \sin\left(\frac{\Omega\tau}{2}\right)\right)$$

$$\approx \frac{\delta}{2}\left(q_1 \cos\left(\frac{\Omega\tau}{2}\right) + q_2 \sin\left(\frac{\Omega\tau}{2}\right)\right)$$

Where, $L_5(\tau)$ is obtained by neglecting the nonsecular terms. From equation 3.20 and equations 3.23, it is directly seen that $\sum_n^5 L_n(\tau) = 0$. The slow flow equations are obtained by averaging the effect of each term over one period (T) of oscillation on the quadrature

constituents of the equation.

$$\frac{1}{T}\int_0^T \left(\sum_n L_n(\tau)\sin\left(\frac{\Omega\tau}{2}\right)\right)d\tau = 0$$

$$\frac{1}{T}\int_0^T \left(\sum_n L_n(\tau)\cos\left(\frac{\Omega\tau}{2}\right)\right)d\tau = 0$$

For the system considered, the time period is given by 4π / Ω. The sine quadrature coefficients are calculated as shown below,

$$\frac{1}{T}\int_0^T \left(L_1(\tau)\sin\left(\frac{\Omega\tau}{2}\right)\right)d\tau = -\frac{1}{2}\left(\frac{\Omega}{2}\dot{q}_1 - \left(\frac{\Omega}{2}\right)^2 q_2\right)$$

$$\frac{1}{T}\int_0^T \left(L_2(\tau)\sin\left(\frac{\Omega\tau}{2}\right)\right)d\tau = -\mu\frac{\Omega\tau}{4}q_1$$

$$\frac{1}{T}\int_0^T \left(L_3(\tau)\sin\left(\frac{\Omega\tau}{2}\right)\right)d\tau = -\frac{q_2}{2}$$

$$\frac{1}{T}\int_0^T \left(L_4(\tau)\sin\left(\frac{\Omega\tau}{2}\right)\right)d\tau = -\gamma\frac{3}{8}q_2(q_1^2 + q_2^2)$$

$$\frac{1}{T}\int_0^T \left(L_5(\tau)\sin\left(\frac{\Omega\tau}{2}\right)\right)d\tau = \frac{\delta}{4}q_2$$

The cosine quadrature coefficients are calculated as shown below,

$$\frac{1}{T}\int_0^T \left(L_1(\tau)\cos\left(\frac{\Omega\tau}{2}\right)\right)d\tau = -\frac{1}{2}\left(\frac{\Omega}{2}\dot{q}_2 + \left(\frac{\Omega}{2}\right)^2 q_1\right)$$

$$\frac{1}{T}\int_0^T \left(L_2(\tau)\cos\left(\frac{\Omega\tau}{2}\right)\right)d\tau = -\mu\frac{\Omega\tau}{4}q_2$$

$$\frac{1}{T}\int_0^T \left(L_3(\tau)\cos\left(\frac{\Omega\tau}{2}\right)\right)d\tau = -\frac{q_1}{2}$$

$$\frac{1}{T}\int_0^T \left(L_4(\tau)\cos\left(\frac{\Omega\tau}{2}\right)\right)d\tau = \gamma\frac{3}{8}q_1(q_1^2 + q_2^2)$$

$$\frac{1}{T}\int_0^T \left(L_5(\tau)\cos\left(\frac{\Omega\tau}{2}\right)\right)d\tau = \frac{\delta}{4}q_1$$

Summing all the terms and setting them to zero, we get the governing equations for slow variables.

$$\dot{q}_1 = -\mu q_1 + 2\sigma q_2 + \frac{\delta}{\Omega}q_2 - \frac{3\gamma}{2\Omega}q_2(q_1^2 + q_2^2)$$

$$\dot{q}_2 = -\mu q_1 - 2\sigma q_2 + \frac{\delta}{\Omega}q_2 + \frac{3\gamma}{2\Omega}q_2(q_1^2 + q_2^2)$$

Where, $\sigma = \Omega$ - 2 is the detuning of the system. Now that we have the governing equations for the slow variables, we will look into the steady state solutions in the next section. The steady state solutions, are those where the time dependence vanishes (No transient in the solution), $\dot{q}_1 = \dot{q}_2 = 0$. The amplitude square of oscillation is given by the pythagorean sum of squares of the quadrature signals $a^2 = q_1^2 + q_2^2$.

$$-\mu q_1 + \left(\frac{\delta}{\Omega} + 2\sigma - \frac{3\gamma}{2\Omega}a^2\right)q_2 = 0$$

$$-\mu q_2 + \left(\frac{\delta}{\Omega} - 2\sigma + \frac{3\gamma}{2\Omega}a^2\right)q_1 = 0$$

Simultaneously solving above equations and using the expression $a^2 = q_1^2 + q_2^2$ we obtain,

$$\left(\left(\frac{\delta}{\Omega}\right) - \left(2\sigma - \frac{3\gamma}{2\Omega}\right) - \mu^2\right)a^2 = 0$$

The above equation provides a relation between the amplitude as a function of the detuning valid very near the resonance, i.e $\omega = 2\omega_0$

Rewriting the above amplitude equation we have the frequency response function for a parametrically excited system,

$$a^2 = \frac{4\omega_0}{3\gamma}\left[2\sigma \pm \left(\left(\frac{\delta}{\Omega} - \mu^2\right)\right)^{1/2}\right] \tag{3.24}$$

It is clear that the equation 3.20 has two types of solutions: a trivial solution corresponding to (x=0) and the non trivial solution corresponding to (x≠ 0). The steady state solutions obtained for the non-trivial fixed points (x≠ 0) is given by equation 3.24. This equation helps us to examine the spectral features of the parametrically resonant system. The amplitude a, has two branches, a stable branch and an unstable branch. Figure 3.2 explains the number of solutions present and stability of each solution in various regions of a parametrically excited system.
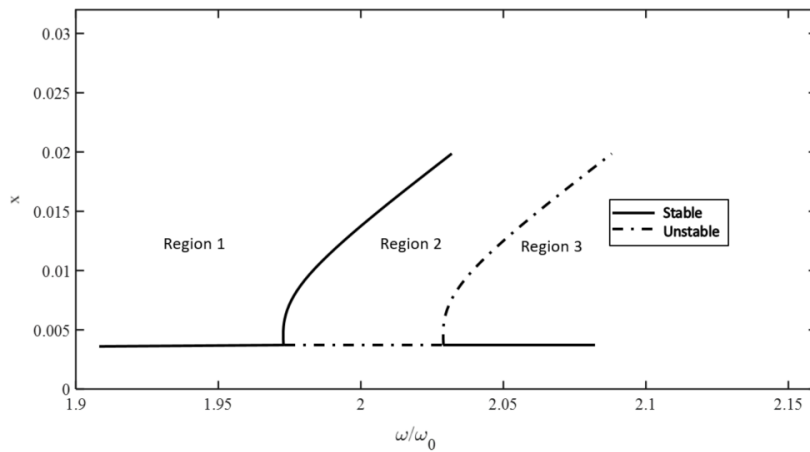
Figure 3.2: Stability of steady state solutions in a parametrically excited system. The response curves are obtained for coefficients $\omega_0 = 1$, $\mu = 0.03$, $\gamma = 0.5$, $\delta = 0.25$ and $\sigma = 0.3$

Region I: In this region, the system has only a stable zero amplitude or no motion solution. All initial conditions will decay to this value. In phase space, it corresponds to a center at (0,0).
Region II: In this region, the system has a zero-amplitude solution and a set of stable high

amplitude solution which are symmetric but differ by a phase of 180°. In phase space, this is represented by a saddle point at (0,0) and two centers corresponding to trivial unstable and nontrivial stable solutions. This is a bi-stable region.

Region III: In this region, the unstable branch separates a zero-amplitude stable solution from a high amplitude stable solution. The hysteresis in this region is seen in many of the literature and well documented concerning mechanical oscillators in experiment at the micro and nano scale. This is an important phenomena, which will be revisited in further chapters in detail. In phase space, the trivial stable solution is represented by a center at (0,0), the nontrivial stable and unstable solutions are represented by two centers and two saddle points respectively. This represents a tri-stable region.

The 'regions' under discussion are separated by curves in the parameter space called 'Transition curves' or 'Instability curves' as shown in Figure 3.5. Essentially, these curves (points on these curves) create, destroy, or modify the type of stability of fixed points. By definition, these are bifurcations.

3.3.2. STABILITY ANALYSIS

The system described by equations 3.24 is known to be unstable for certain range of parameters (δ, Ω) [46, 47]. The stability of such a system can be studied by linearizing the nonlinear system given by equations 3.24 around an equilibrium point and then analyzing its eigenvalues [Hartman-Grobman theorem [47]].

let,

$$\bar{x} = \begin{bmatrix} q_1 \\ q_2 \end{bmatrix}$$

Then, the linearized system of equations is given by,

$$\dot{\bar{x}} = A\bar{x}, \qquad A = \begin{bmatrix} -\mu & \frac{\delta}{\Omega} + 2\sigma \\ \frac{\delta}{\Omega} - 2\sigma & -\mu \end{bmatrix}$$

The characteristic equation for A is then det[A-sI]=0, where s represents the eigenvalue. Solving the characteristic equation we find,

$$s_{1,2} = -\mu \pm \sqrt{\left(\frac{\delta}{\Omega}\right)^2 - (2\sigma)^2}$$

Where, $s_{1,2}$ denotes the eigenvalues of the system. To evaluate the stability of the system, we consider the real part of the eigenvalues. If the real part of all the eigenvalues are negative, it indicates the system is stable otherwise the system is unstable. The system considered will have negative real parts for both the eigenvalues, except for the cases where the parameters space (δ, Ω) satisfies the following relationship:

$$-\mu \pm \sqrt{\left(\frac{\delta}{\Omega}\right)^2 - (2\sigma)^2} > 0 \tag{3.25}$$

It can be noted that, the detuning, σ will always impede the presence of the instability. From the above expression, it is seen that achieving parametric resonance is a matter of

driving the system with adequate strength. Equation 3.25 delineates the region in the driving parameters for which the system is stable or unstable. A plot obtained using this equation with the parametric drive term (δ) versus the detuning (σ) results in the so called 'Transition curve' of the system. This transition curve dictates the points of period doubling bifurcations and is shown in Figure 3.5.

To find the minimum strength required to push the system into parametric resonance, we look at the case where detuning is zero ($\sigma = 0$ and $\Omega = 2$). Then, the required driving field strength to achieve parametric resonance becomes,

$$\delta_{th} > \Omega\mu = 2\mu = \frac{2}{Q} \tag{3.26}$$

Where, the damping factor μ is written as $\frac{1}{Q}$, Q being the quality factor of the resonator. The expression coincides with the work of reference [45, 47], where a polar form of the solution is used to arrive at the same equations. From the above expression, it is clear that, to excite the system into parametric resonance, there exists a critical drive threshold (δ_{th}), which should overcome the linear damping present in the system. Furthermore, an increase in quality factor of the system increase the parameter space in which instabilities exist. This is a very important result required to perform numerical simulations. There is an interesting temporal feature of parametrically excited systems to note here. The drive term given by $\delta\cos(\Omega\tau)$, is proportional to the oscillation amplitude. This means that, as the amplitude of oscillation grows, so does the energy that is being pumped into the system. This makes a characteristic exponential amplitude growth in the slow variables in time.

3.4. NUMERICAL SIMULATION

The equation of motion of a graphene nanoresonator, that is parametrically excited is formulated as shown in section 3.2. The table 3.2 shows the graphene mechanical and thermal properties used for the Lagrangian formulation.

parameter	value	Definition
a	$2.5\,\mu\text{m}$	Radius
h	$0.335\,\text{nm}$	Thickness
ρ	$2330\,\text{kg}\,\text{m}^{-3}$	Density
E	$1\,\text{TPa}$	Young's modulus
ν	0.16	Poisson's ratio
n_0	$0.006\,159\,\text{N}\,\text{m}^{-1}$	Intial Tension
C	$9.195\,64 \times 10^{-15}\,\text{J}\,\text{K}^{-1}$	Thermal capacitance
τ	$100\,\text{ns}$	Thermal time constant
P_{total}	$2\,\text{mW}$	Total laser power
Ω_0	$13.6\,\text{MHz}$	1st natural frequency

Table 3.2: Graphene material parameters

The equation of motion is obtained using *MATHEMATICA* and is of the form shown in equation 3.20. In order to simulate the equation numerically, the equation of motion is cast into state space form. The numerical simulations are perfomed using a bifurcation analysis

and continuation software package called *AUTO* [48]. The package uses psuedo arclength continuation and collocation technique to detect bifurcations and obtain periodic solutions.

In particular, the bifurcation analysis is carried out in four steps:

1. The equation of motion 3.20 is made dimensionless with respect to the amplitude of oscillations by dividing the displacements by the radius a of the membrane .

2. The bifurcation analysis is carried out with the absorbed power P_{abs} as the first continuation parameter and is incremented to a chosen power level.

3. After reaching the desired P_{abs}, the solution is continued by considering the frequency ratio $\Omega = \omega/\omega_0$ (ω_0 being the fundamental frequency) as the second bifurcation parameter which is spanned in the spectral neighborhood of $\Omega = 2$ in order to obtain parametric resonance.

4. The onset of parametric resonance is confirmed by the presence of period doubling (PD) bifurcation or a Floquet multiplier of '-1' in the output of step 3. Once the points of bifurcation are known, the branches of solution is obtained by continuing the analysis with the frequency ratio $\Omega = \omega/\omega_0$ as the parameter to obtain the stable and unstable solution branches till the desired frequency range.

Numerical simulations have been performed with a Single-Degree-Of-Freedom (SDOF) model made up of fundamental mode of the circular membrane and Multiple-Degree-Of-Freedom (MDOF) model made up of 1 out-of-plane mode and 4 in-plane modes. Figure 3.3 and 3.4 shows parametric resonance of the membrane subjected to different levels of absorption power for a SDOF and MDOF model respectively. The continuous line indicates stable branch of solution and the dashed line indicates unstable branch. It is clearly seen that, below a critical threshold of absorbed power $P_{abs}< 0.15\,\mu W$ for SDOF model and $P_{abs}< 0.14\,\mu W$ for MDOF model, the system is not pushed into linear instability and therefore no parametric resonance is observed. It can be seen that, close to $\Omega = 2$, a dynamic Mathieu-type instability takes place, and the vibration amplitude can be quite large. Indeed, a Period Doubling (PD) bifurcation appears giving rise to a new stable solution branch.

Furthermore, a very important point to notice here is that the linear damping doesn't have a strong effect on the amplitude of parametric resonance. In other words, the amplitude of resonator rises exponentially unless the system has a very large linear damping. This is the first indication of the presence of higher order nonlinear damping in the system which saturates the parametric response. This is discussed in detail in chapter 5.
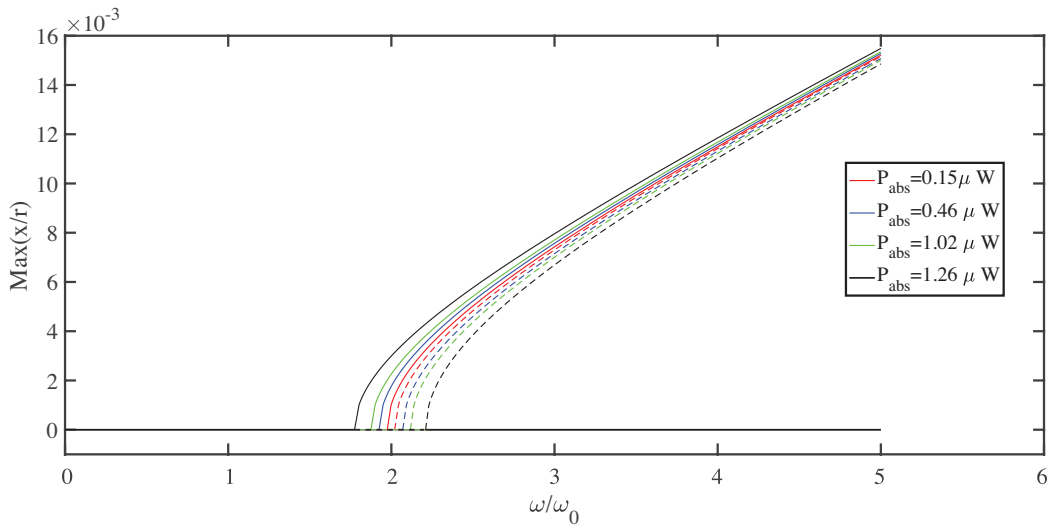
Figure 3.3: Parametric resonance at different absorption powers for SDOF model
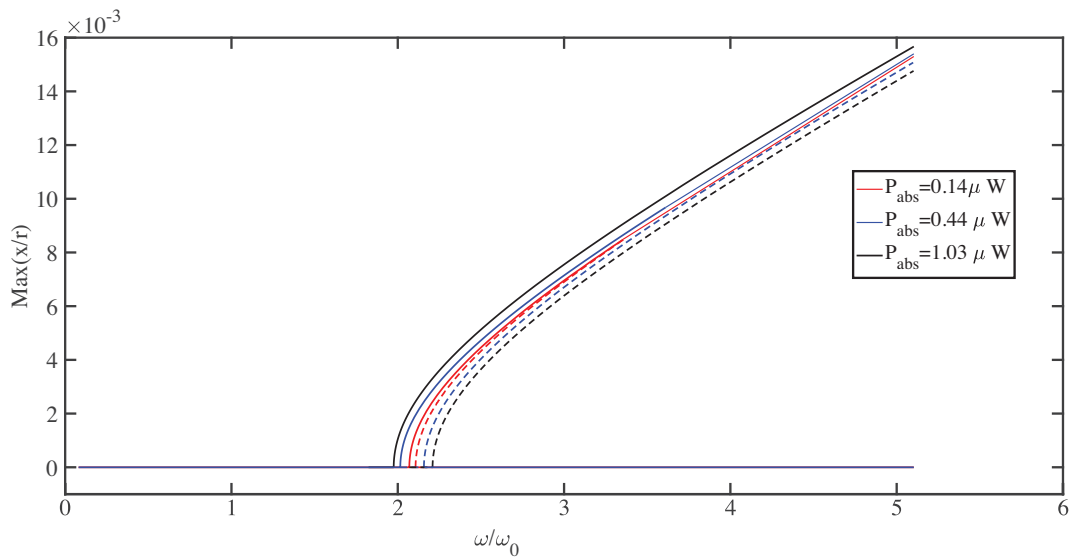

Figure 3.4: Parametric resonance at different absorption powers for MDOF model

Figure 3.5 shows the transition curve for a SDOF model obtained from numerical simulation. The corresponding analytical expression is given by 3.25. The curve indicates the minimum threshold parametric drive required to over come the linear damping in the system and excite the resonator into parametric resonance. The inset shows the tip of the curve to be curved which indicates a slightly damped system. Indeed, in the absence of any damping in the system, the tip of the curve would have a sharp edge like transition instead of a smooth curve.
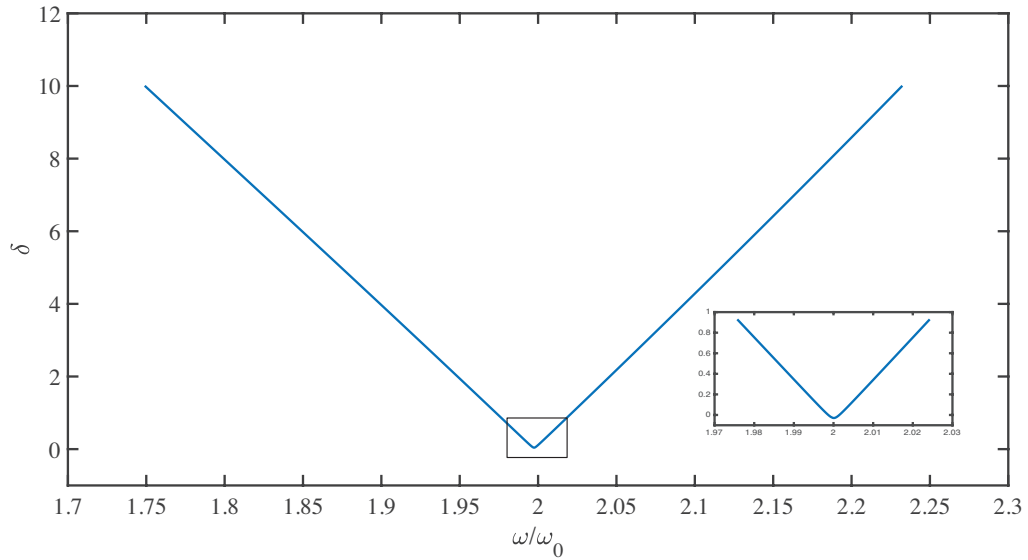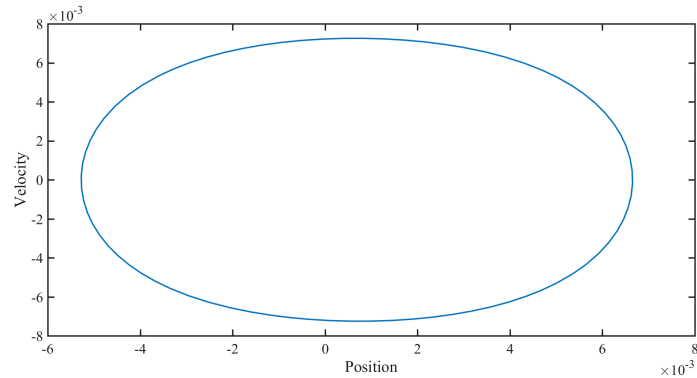
Figure 3.5: Transition curve for SDOF model

3.4.1. PHASE SPACE PLOT AND PARAMETER VARIATION OVER A TIME PERIOD

The phase space plot for a parametric response is shown in Figure 3.6. The closed curve indicates the presence of a periodic solution.

Figure 3.6: Phase space graph at $\omega = 2.2\omega_0$ indicating a periodic solution

In order to reassure the occurrence of parametric resonance, the temporal variation of displacement and force is investigated. The variation of displacement and parametric drive as a function of time period (T) for a SDOF model is shown in figures 3.7 and 3.8 respectively. The plots correspond to the numerical simulation data, taken at frequency $\omega = 2.2\omega_0$. As seen in the figures, when the forcing function has a period of $\frac{T}{2}$, the corresponding displacement has a period of T. This is termed as period doubling, one of the clear indicators of parametric resonance.
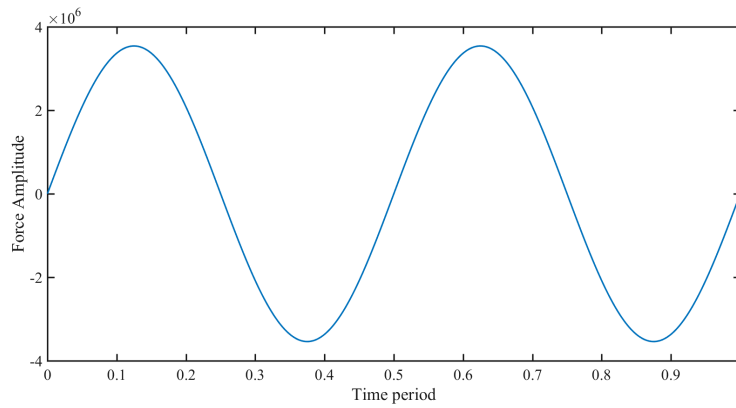
Figure 3.7: Parametric drive varying as a function of time period at $\omega = 2.2\omega_0$
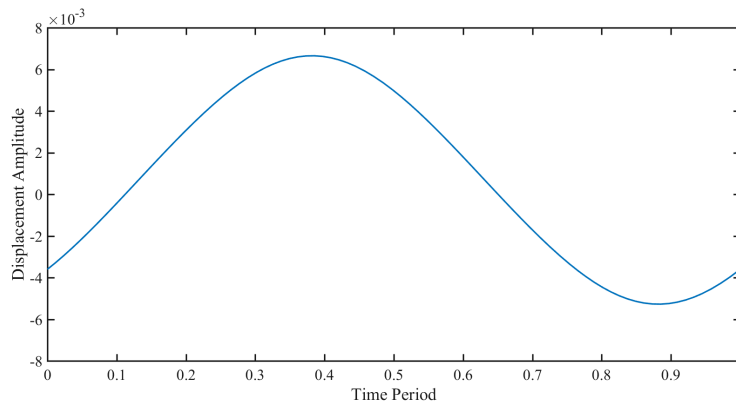

Figure 3.8: Membrane motion as a function of time period at $\omega = 2.2\omega_0$

By utilizing the plots of force vs time period and displacement vs time period, the actuation mechanism of parametric resonance is explained schematically in figure 3.9. As discussed in the previous sections, the parametric resonance in optically actuated graphene nanodrum resonators is due to the stiffness modulation caused by the periodic heating of the membrane. In Figure 3.9, the blue membrane is indicative of lower temperature and red membrane represents higher temperature. Each time the laser modulation indicated by blue curve is maximum, it causes the tension to be modulated to its maximum and as a result, the membrane motion indicated by the green curve passes through the equilibrium. Moreover, the laser modulation occurs twice per period and hence the tension is also modulated twice per period of membrane motion. This leads to period doubling bifurcation and hence, parametric resonance.
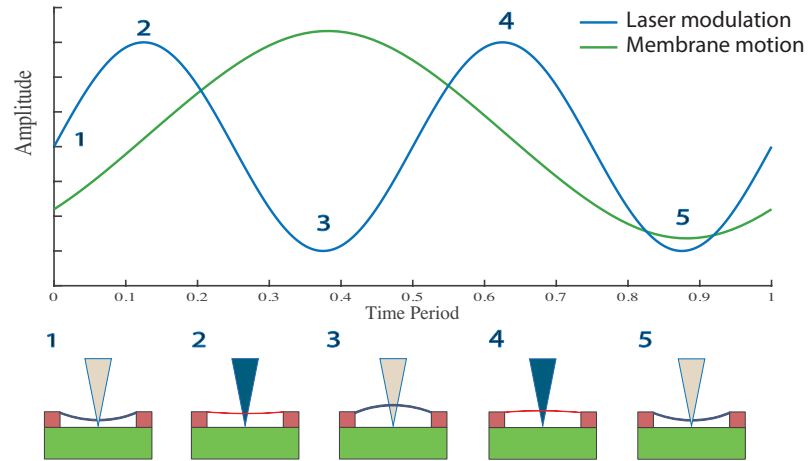
Figure 3.9: Schematic showing parametric resonance actuation mechanism

3.5. Conclusion

In this chapter, the source of parametric excitation is explained on the basis of change in tension due to heating of the membrane. The governing temperature field responsible for periodic heating is derived based on energy exchange formulas. The dynamics of parametrically excited Duffing oscillator is explained with detailed derivations of governing equations and stability analysis is performed. The concepts of instability region and critical parametric drive amplitude is introduced and its dependency on the quality factor of the system is explained. A series of numerical simulations are performed for different absorbed powers and it was shown that temperature modulated tension is indeed the reason for parametric excitation. By studying the underlying dynamics, it was concluded that linear damping has a limited effect on the oscillation amplitude of a resonator under parametric resonance. This indicates that, there might be higher order nonlinear damping terms which are responsible for saturation of parametric response.

4

DIRECTLY DRIVEN GRAPHENE NANODRUM RESONATORS

In the previous chapter, the physics behind the parametric excitation was explained with detailed equations. But as seen in Figure 1.3, there is a direct excitation response around the natural frequency of the resonator, which is not discussed in the previous chapter. This chapter deals with the physics and mathematics behind the direct excitation in a single layer graphene nanoresonator that is excited using a laser. To meet this end, the source of direct excitation in monolayer graphene nanoresonator is explained and the corresponding dynamics of a directly excited resonator model is briefly discussed. The existence of primary and secondary resonances are illustrated and finally numerical simulations are carried out to prove the theoretical predictions.

4.1. SOURCE OF DIRECT EXCITATION: OPTICAL FORCE OR RADIATION PRESSURE

The first source of direct excitation considered is the optical force or radiation pressure exerted by the laser onto the membrane. The photons in the laser transfer their momemtum when they collide with the membrane. In this section, this rate of change of momentum is modeled as a physical force and simulated.

The total optical force exerted by a laser with power (P) assuming no transmission and other losses is given by the equation,

$$F_{optical} = \frac{\beta_{abs}P}{c} + \frac{2\beta_{ref}P}{c} \tag{4.1}$$

Where, β_{abs} and β_{ref} are the coefficients of absorption and reflection of graphene respectively and c is the speed of light. Above equation assumes that total power of the laser is either reflected or absorbed with no other optical losses. Furthermore, to obtain the maximum optical force, an assumption is made that all of the incident total power is reflected i.e., $\beta_{abs} = 0$. This reduces the above equation to,

$$F_{optical} = \frac{2\beta_{ref}P}{c} \tag{4.2}$$

Considering a total power of 2 mW and an reflection coefficient (β_{ref}) of 1, the maximum optical force exerted by the laser is given by,

$$F_{optical} = 13.3\,\text{pN} \tag{4.3}$$

4.1.1. NUMERICAL SIMULATION

The equation of motion of a forced Duffing oscillator given by equation 4.4 is simulated in continuation software package *AUTO*. The optical force calculated above is used as the amplitude of external drive.

The dimensionless equation of motion is given by,

$$\ddot{x} + \mu\dot{x} + x + \gamma x^3 = \bar{F}\cos(\Omega t) \tag{4.4}$$

Where $\bar{F} = \frac{F_{optical}}{k}$. Simulating the above equation around the frequency range Ω=1, we find the frequency response of the system as shown in Figure 4.1. It is clear from the frequency response curve that, even at maximum reflection coefficient, the optical force exerted by the laser cannot induce a large amplitude response in the system. From this, it can be concluded that, the optical force exerted by laser is not the source of direct excitation seen in the experimental responses.
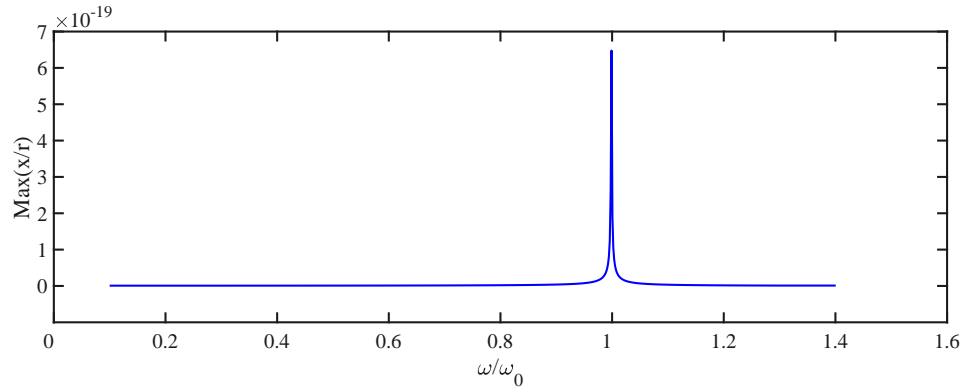

Figure 4.1: Dynamic response with optical force as source of excitation

4.2. SOURCE OF DIRECT EXCITATION: INITIAL GEOMETRIC IM-PERFECTION

From the previous section, it was proved that the optical force lacks the strength to drive the system to large amplitude responses. Another source of direct excitation is the initial geometric imperfection present in the system. So far, the membrane is assumed to be perfectly flat but in reality this is rarely the case. A small geometric imperfection is present in majority of the resonators as shown in Figure 4.2 and is experimentally verified. The height of such an imperfection from the flat configuration is measured using an Atomic force microscope and is found to be approximately 10 nm. This value could vary between different samples to a certain extent but, in order to explain the dynamics, it is assumed to

be exactly 10 nm. This initial deviation from the flat configuration could be due to out-of-plane crumpling or rippling of the graphene membrane. In this section, such an geometric imperfection is assumed to resemble the fundamental mode shape of the circular membrane and is incorporated as an additional term in the transverse displacements. Furthermore, Lagrange equations are formulated to obtain the governing equations of motion.
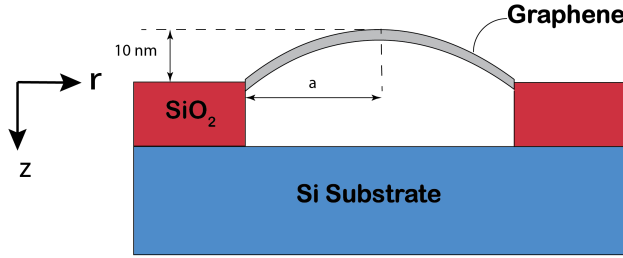

Figure 4.2: Negative initial imperfection modeled as first vibrational mode shape.

4.2.1. Mathematical Modeling using Lagrangian Approach

The procedure to derive the mathematical model is similar to that shown in section 3.2, with the difference that the transverse displacement function now includes w_0, the deviation of the membrane in the negative z-direction from flat configuration. Similarly, the dynamics and response of the system to positive geometric imperfection is shown in appendix B.

For an axisymmetric model, the radial displacement field is given by equation 3.8 and the transverse displacement equation from 2.7 can be rewritten as,

$$u_z(r, \theta, z, t) = w(r, t) - w_0(r)$$

Where, w_0 represents the initial geometric imperfection. The negative sign is taken as per the conventions indicated in Figure 4.2 and from here on, is referred to as negative initial geometric impefection. For simplifying the model, the spatial distribution of the geometric imperfection is assumed to resemble the first vibration mode shape of the circular membrane.

$$u_z = x(t) J_0\left(\alpha_0 \frac{r}{a}\right) - \delta J_0\left(\alpha_0 \frac{r}{a}\right) \tag{4.5}$$

Where, $\delta = 10$ nm and $\alpha_0 = 2.40483$. The strains and stresses for the axisymmetric model can be obtained from equation 2.16 and equation 2.10 respectively. The rest of the derivation closely follows the procedure shown in section 3.2

The governing nonlinear equations of motion for a MDOF graphene resonator can be obtained from equation 3.11. By incorporating the geometric imperfection in the modeling, the main difference seen in the equation of motion is the appearance of nonlinear quadratic term (x^2) along with the direct excitation terms. The equation of motion is given by,

$$\mathbf{M\ddot{q}} + \mathbf{C\dot{q}} + \left[\mathbf{K_1} + \mathbf{K_2}\cos(\omega t) + \mathbf{N_2(q)} + \mathbf{N_3(q, q)}\right]\mathbf{q} = \mathbf{F}\cos(\omega t) + \mathbf{F_0} \tag{4.6}$$

where $\mathbf{M}$ is the mass matrix and $\mathbf{C}$ is the viscous damping matrix added to the equations of motion to introduce dissipation. Moreover, $\mathbf{K_1}$ is the linear stiffness matrix dominated by the

tension n_0. $\mathbf{K_2}$ is the coefficient of the time varying stiffness causing parametric excitation as a result of temperature variation ΔT. Furthermore, $\mathbf{N_2}$ gives the quadratic non-linear stiffness terms due to imperfection w_0. $\mathbf{N_3}$ denotes the cubic non-linear stiffness terms and $\mathbf{F}$ is the vector of direct dynamic external excitation and $\mathbf{F_0}$ is the static direct external excitation due to the presence of imperfection. Indeed for a completely flat membrane, $\mathbf{N2} = \mathbf{F} = \mathbf{F_0} = \mathbf{0}$.

For graphene resonators, it is convenient to study the SDOF model which provides insight into the dynamics of the system. The governing nonlinear equation of motion for a SDOF Duffing oscillator is given by the Lagrange equation defined by 3.11. It takes the form as shown below,

$$m\ddot{x} + c\dot{x} + (k + k_p \alpha \Delta T)x + k_2 x^2 + k_3 x^3 = F\cos\omega t + F_0$$

Where,

$$F = k_d \alpha \Delta T, \qquad \Delta T = \frac{P_{abs}\tau^2 \omega \cos(\omega t)}{C(\tau^2\omega^2 + 1)}$$

Taking $F_p = k_p \alpha \Delta T$ as the strength of parametric drive we have,

$$F_p = \frac{k_p \alpha P_{abs}\tau^2 \omega}{C(\tau^2\omega^2 + 1)} \tag{4.7}$$

The final equation of motion is reduced to the standard form of a Duffing-Mathieu-Hill differential equation given by,

$$m\ddot{x} + c\dot{x} + (k + F_p \cos(\omega t))x + k_2 x^2 + k_3 x^3 = F\cos\omega t + F_0 \tag{4.8}$$

where, $(\ddot{\bullet})$ denotes differentiation with respect to time, m is the mass of resonator and c is the viscous damping added to the equation of motion to introduce dissipation. Moreover, k is the linear stiffness term dominated by the tension n_0, k_p is a constant introduced by the thermal strain term, δ is the coefficient of the time varying stiffness causing parametric excitation as a result of temperature variation ΔT. Furthermore, k_2 and k_3 denotes the quadratic and cubic non-linear stiffness term introduced by the imperfection and the geometric nonlinearity respectively. The direct excitation introduced by the imperfection is two fold, a dynamic excitation term given by $F\cos\omega t$ and a static excitation term given by F_0.

4.3. DYNAMICS OF DIRECTLY EXCITED DUFFING OSCILLATOR

In this section, the dynamics of a damped Duffing oscillator with additional quadratic nonlinearity is studied in detail. To simplify the study, parametric drive is turned off i.e $F_p = 0$ in equation 4.8. This assumption is valid since, it is seen that in the experiments, the higher harmonics of principal parametric resonance are not observed even at maximum driving power. Which indicates that the dynamics of the system at excitation frequency $\omega = \omega_0$ is purely dominated by the dynamics of Duffing equation. Furthermore, it is not interesting to see the effect of static forcing term F_0 on the system. Because, this will result in a small static deflection proportional to the compliance of the resonator and hence it is ignored in the current analysis. However, these terms will be incorporated in the numerical simulations

done with continuation software package *AUTO.* Based on these assumptions, the governing differential equation is of the form,

$$m\ddot{x} + c\dot{x} + kx + k_2 x^2 + k_3 x^3 = F\cos\omega t \tag{4.9}$$

Normalizing equation 4.9 with respect to the mass of the resonator and time with respect to time period of resonant mode as shown in equation 3.3.1 we have,

$$\ddot{x} + 2\zeta\dot{x} + x + \eta x^2 + \gamma x^3 = f\cos\Omega\tau \tag{4.10}$$

The definitions of coefficients used in the above equation are as shown in table 4.1.

$Definition$	Non-dimensional parameter
$(\dot{\bullet}) = \frac{d(\bullet)}{d\tau}$	Scaled time derivative
$\Omega = \frac{\omega}{\omega_0}$	Non-dimensional excitation frequency
$\zeta = \frac{c}{2\sqrt{mk}}$	linear damping ratio
$\gamma = \frac{k_3}{m\omega_0^2}$	Scaled nonlinear cubic stiffness coefficient
$\eta = \frac{k_2}{m\omega^2}$	Scaled nonlinear quadratic stiffness coefficient
$f = \frac{F}{m\omega_0^2}$	Scaled Direct drive amplitude

Table 4.1: Non-dimensional parameter definitions

The solutions for several standard forms of Duffing oscillators has been studied extensively in the past decades, the detailed derivation can be found in [44, 46, 49]. In this section, the main features are briefly discussed and focus is provided to understand the qualitative relations between different parameters governing the system dynamics. The detailed derivation using perturbation techniques can be found in appendix B.

4.3.1. Primary Duffing Resonance

Primary resonance occurs when the external excitation coincides with the resonant frequency ($\omega = \omega_0$). The normalized excitation frequency is such that,

$$\Omega = 1 + \epsilon^2\sigma$$

Where, σ is the external detuning

By using the method of multiple scales, the solution of equation 4.10 to second order approximation is given by,

$$x = a\cos(\omega t - \phi) + \frac{1}{2}\epsilon\alpha_2\omega_0^{-2}a^2\left[-1 + \frac{1}{3}\cos(2\omega t - 2\phi)\right] + \mathcal{O}(\epsilon^2) \tag{4.11}$$

The nonlinear term in the solution $\frac{1}{2}\epsilon\alpha_2\omega_0^{-2}a^2$ is due to the asymmetric nonlinearity (x^2), which causes the system to drift or steady stream from the equilibrium position.

The frequency response equation given by,

$$\left[\zeta^2 + \left(\sigma - \frac{9\gamma - 10\eta^2}{24}a^2\right)\right]a^2 = \frac{f^2}{4} \tag{4.12}$$

The phase equation is given by,

$$\tan\phi = \frac{\zeta}{\sigma - \frac{9\gamma - 10\eta^2}{24}a^2} \tag{4.13}$$

But from Figure 1.3, it is seen that, the hardening behavior dominates in the Duffing response indicating that, $\gamma > \frac{10}{9}\eta^2$ for optically actuated graphene nanodrum resonators. This is an important result as it indicates that, in order to fit a Duffing response to an experimentally obtained curve, we can ignore the effect of quadratic nonlinear stiffness and build a model with a dominant cubic stiffness nonlinearity.

It is seen that, the effect of nonlinearity is to bend the amplitude curve and distort the phase curve. The profound difference between the nonlinear and linear oscillator is that, in the nonlinear case the response is multivalued, meaning there can be as much as three different response amplitudes for a driving frequency. This is consequence of the fact that the equation 4.12 is cubic in a^2. This multivaluedness leads to the well known *jump phenomenon.* which is discussed in detail in appendix B.

4.3.2. SECONDARY OR SUPERHARMONIC RESONANCES

As seen in Figure 1.3, in addition to the standard Duffing response, we see additional superharmonic resonances at $\omega = \frac{\omega_0}{2}$ and $\omega = \frac{\omega_0}{3}$ corresponding to the quadratic and cubic nonlinearities.

For quadratic nonlinearity

The normalized external excitation frequency is given by,

$$\Omega = \frac{1}{2} + \epsilon\sigma$$

The solution to the first approximation is obtained by using method of mutliple scales,

$$x = \frac{\frac{F}{m}}{\omega_0^2 - \Omega^2}\cos(\omega t) - a\sin(2\omega t - \phi) + \mathcal{O}(\epsilon) \tag{4.14}$$

Where a is given by,

$$a = \frac{\eta F^2}{4m^2\omega_0(\omega_0^2 - \Omega^2)^2(\zeta^2 + \sigma^2)^{1/2}}$$

For cubic nonlinearity

The normalized external excitation frequency is given by,

$$\Omega = \frac{1}{3} + \epsilon\sigma$$

The solution to the first approximation is obtained by using method of mutliple scales,

$$x = \frac{\frac{F}{m}}{\omega_0^2 - \Omega^2} \cos(\omega t) + a\cos(3\omega t - \phi) + \mathcal{O}(\epsilon) \qquad (4.15)$$

Where a is given by,

$$\left[\zeta^2 + \left(\sigma - 3\frac{\gamma\Lambda^2}{\omega_0} - \frac{3\gamma}{8\omega_0}a^2\right)^2\right]a^2 = \frac{\gamma^2\Lambda^6}{\omega_0^2}$$

$$\Lambda = \frac{\frac{F}{m}}{\omega_0^2 - \Omega^2}$$

From the above equations we see that, when $\omega = \frac{\omega_0}{2}$ and $\omega = \frac{\omega_0}{3}$, the free oscillation term does not decay to zero in spite of presence of damping and is in contrast with the linear case. Moreover, the nonlinearities adjusts the frequency of free oscillation term to exactly twice and thrice the frequency of excitation so that the response is periodic. Since the frequency of the generated free oscillation term is an higher multiple of excitation frequency, they are termed as superharmonic or secondary resonances. This explains the reason behind the appearance of such secondary resonances seen in Figure 1.3.

4.4. NUMERICAL SIMULATIONS

The equation of motion for a SDOF and MDOF is given by equations 4.8 and 4.6 respectively. In this section, the numerical simulations are performed using the continuation software package *AUTO*. The equation of motion is obtained from *MATHEMATICA* model using the graphene parameters given by equation 3.2. In particular, the bifurcation analysis is carried out as described in the following steps:

1. The equation of motion 4.8 is normalized with respect to the mass of the resonator, the time is scaled with respect to the period of the resonant mode and finally, the displacements are made dimensionless by dividing with respect to the radius a of the membrane. Then, the equation is cast into state space form converting a second order differential equation into two first order differential equations.

2. The bifurcation analysis begins by assuming the initial imperfection to be of the form $w_0 = -\delta J_0\left(\alpha_0 \frac{r}{R}\right)$ with δ as the first continuation parameter.

3. Once the desired imperfection amplitude is reached, the bifurcation analysis is carried out with the absorbed power P_{abs} as the second continuation parameter and is incremented to a chosen power level.

4. After reaching the desired P_{abs}, the solution is continued by considering the frequency ratio $\Omega = \omega/\omega_0$ (ω_0 being the fundamental frequency) as the second bifurcation parameter, which is spanned in the spectral neighborhood of $\Omega = 1$ and $\Omega = 2$ in order to obtain direct and parametric resonance. The superharmonic resonances are obtained by sweeping the frequency from $\Omega = 0.2$ till 0.6.

5. The Duffing response begins by tracing the stable branch of the solution and becomes unstable after reaching the limit point (LP) and further continues to trace the unstable branch of the solution.

6. The onset of Parametric resonance is confirmed by the presence of period doubling (PD) or Floquet multiplier equal to '-1' in the output of step 3. Once the points of bifurcation are known, the branches of solution is obtained by continuing the analysis with the frequency ratio $\Omega = \omega/\omega_0$ as the parameter. This gives the parametric stable and unstable solution branches till the desired frequency range.

Figure 4.3 shows the frequency response of a SDOF model with initial geometric imperfection simulated using *AUTO* at a specific absorption power. It can be seen that, the geometric imperfection clearly acts as a source of direct excitation in single layer graphene nanodrum resonators which are optically actuated. The figure also shows the parametric response caused by tension modulation through heating of the membrane. Furthermore, the superharmonic resonances due to the quadratic and cubic nonlinearity are present in the vicinity of $\omega = 0.3\omega_0$ and $\omega = 0.5\omega_0$ respectively. The stable branches are indicated by continuous lines and the unstable branches are indicated by dashed lines.

An interesting behavior is that the direct primary resonance ($\omega = \omega_0$) and secondary resonances ($\omega = 0.3\omega_0$, $\omega = 0.5\omega_0$) are shifted to the left slightly because of the increase in linear stiffness (k+ Δk) caused by inserting an imperfection to the model. Furthermore, it can be seen from the figure that, the amplitudes of direct and parametric responses are affected differently by linear damping term. This is in agreement with the theory that linear damping doesn't have a strong curbing effect on the amplitude of parametric response. The figure also indicates the presence of limit points and period doubling bifurcations which are one of the main indicators of Duffing and parametric responses respectively.

Figure 4.4 shows the frequency response of 5 DOF model with one out of plane and 4 in-plane modes. The qualitative dynamics remains the same, but the amplitudes of oscillation are different.
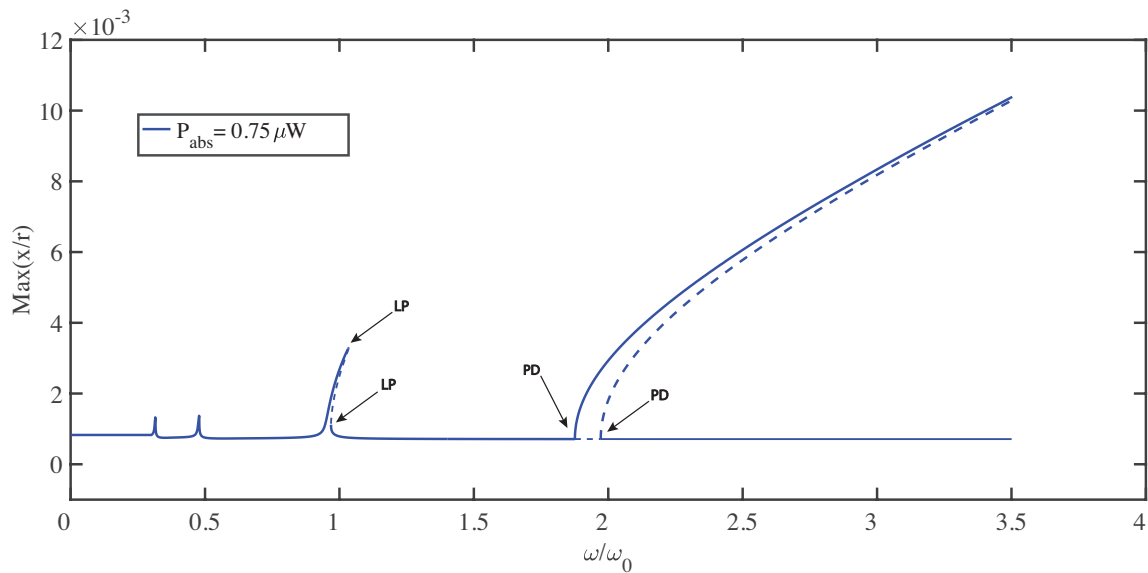
Figure 4.3: Frequency response of SDOF model showing direct, parametric and superharmonic responses
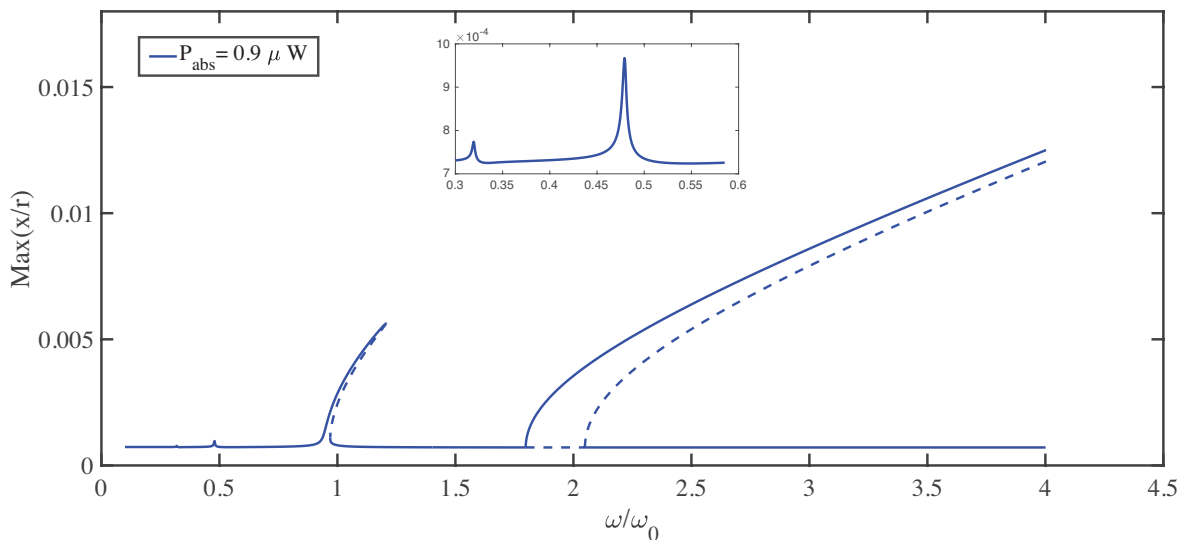

Figure 4.4: Frequency response of MDOF model with negative initial imperfection showing direct, parametric and superharmonic responses

4.4.1. PHASE SPACE PLOT AND PARAMETER VARIATION OVER A TIME PERIOD

The phase space plot of direct Duffing response is shown in Figure 4.5. The closed curve indicates the presence of periodic solution. Furthermore, the variation of Force, displacement and velocity of membrane as a function of time period (T) for a SDOF model is shown in Figures 4.7 and 4.6. The plot corresponds to the numerical simulation data at frequency $\omega = 1.2\omega_0$. As seen in these figures, when the forcing function has a period of T, the corresponding displacement has a period of T. This is in accordance with standard forced harmonic resonance where, the displacement oscillates at the same frequency as the forcing function.
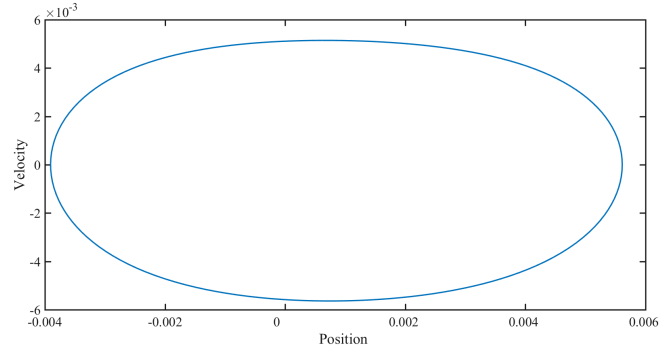
Figure 4.5: Phase space graph at $\omega = 1.2\omega_0$ indicating a periodic solution
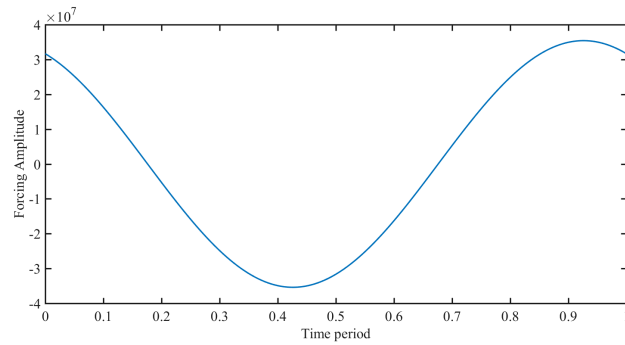

Figure 4.6: Force amplitude as a function of time period at $\omega = 1.2\omega_0$
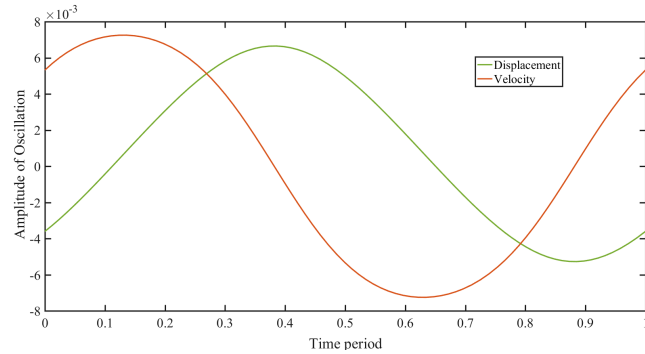

Figure 4.7: Membrane displacement and velocity as a function of time period at $\omega = 1.2\omega_0$

By utilizing the plots of force vs time period and displacement vs time period, the actuation mechanism of parametric resonance is explained schematically in Figure 4.8. As discussed in the previous sections, the direct resonance in optically actuated graphene nanodrum resonators is due to the presence of initial geometric imperfection. Each time the laser modulation indicated by blue curve is maximum, the membrane motion indicated by the green curve passes through the equilibrium indicating that laser modulation is synchronized with membrane motion. This leads to forced harmonic resonance.
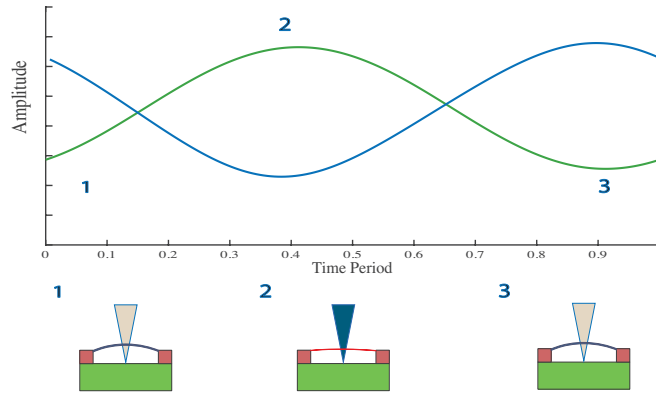
Figure 4.8: Schematic showing direct resonance actuation mechanism

4.5. CONCLUSION

In this chapter, the source of direct excitation in graphene nanodrum resonators is explained on the basis of presence of an initial geometric imperfection. The alternate possibility of optical force being the source of excitation is disproved based on lack of driving strength to produce Duffing response as shown in Figure 4.9. The dynamics of directly excited duffing oscillator is studied in detail based on the models obtained through Lagrangian approach. A series of numerical simulations is performed and it was shown that primary direct resonance at $\omega = \omega_0$ and secondary resonances at $\omega = 0.3\omega_0$, $\omega = 0.5\omega_0$ due to the quadratic and cubic nonlinearities are possible. By studying the dynamics of direct excitation, it was further verified that the linear damping has varied effects on the direct and parametric responses.
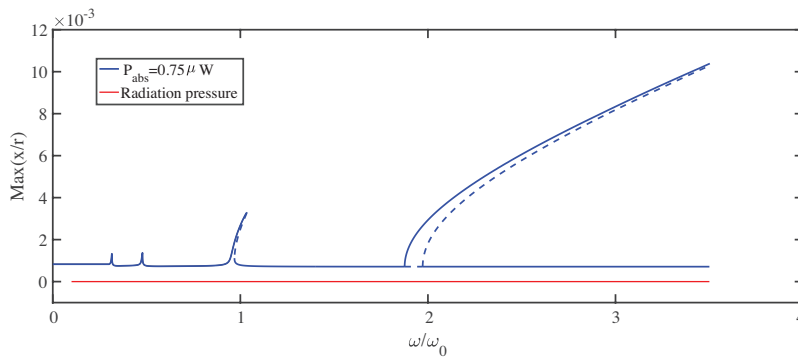

Figure 4.9: Comparison of frequency response produced by optical force (red curve) and initial geometric imperfection (blue curve) as sources of direct excitation

<p style="text-align: right; font-size: 3em; font-weight: bold;">5</p>

EXPERIMENTAL RESULTS AND COMPARISON WITH THEORETICAL MODELS

In this chapter, a brief introduction is given to Duffing-Mathieu model with nonlinear damping, then the theoretical models obtained are used to fit the experimental curves. One single theoretical model is used to fit both Duffing and parametric response obtained from the experiments and the results are analyzed at the end of the chapter. Furthermore, a way to characterize t he material properties of graphene is introduced based on the mathematical model and experimental response curves.

5.1. DYNAMICS OF DIRECTLY DRIVEN DUFFING OSCILLATOR WITH NONLINEAR DAMPING

In this section, an overview on the dynamics of directly driven SDOF Duffing oscillator with nonlinear damping is provided. The oscillator is driven by an external periodic force. A nonlinear damping term ($x^2\dot{x}$) is introduced externally into the equation of motion to represent the dissipation caused by material damping. The detailed derivation and response curves are shown in appendix D.

The normalized equation of motion is given by,

$$\ddot{x} + Q^{-1}\dot{x} + x + x^2 + \eta x^2 \dot{x} + x^3 = f \cos\Omega\tau \tag{5.1}$$

Where the overhead dots denotes the differentiation with respect to the dimensionless time τ, Ω is the nondimensional excitation frequency, Q is the quality factor of the system, η is the scaled nonlinear damping coefficient and f is the scaled direct excitation amplitude.

The frequency response equation to system 5.1 is obtained by using perturbation technique and by casting the system into slow variables. It is given by,

$$f = \left[\left(\frac{3}{4}|a|^2 - 2\sigma \right) + i\left(1 + \frac{\eta}{4}|a|^2 \right) \right] a \tag{5.2}$$

The amplitude and phase of the response are then obtained from equation 5.2 and is given

by,

$$|a|^2 = \frac{g^2}{\left(2\sigma - \frac{3}{4}|a|^2\right)^2 + \left(1 + \frac{\eta}{4}|a|^2\right)^2} \tag{5.3}$$

$$\tan\phi = \frac{1 + \frac{\eta}{4}|a|^2}{2\sigma - \frac{3}{4}|a|^2} \tag{5.4}$$

From equation 5.3 it can be seen that the responsivity (a/g) decreases with increase in nonlinear damping. This is discussed in detail in appendix D.

When the drive amplitude is f is sufficiently strong, we can use equation 5.2 to find the bifurcation points. These are the points of vertical tangencies which are obtained using the condition that $\frac{d\sigma}{da^2}$=0. This yields a quadratic equation in σ, which is solved to obtain the frequencies at which bifurcations occur.

$$\sigma^{\pm} = \frac{3}{4}|a|^2 \pm \frac{1}{2}\sqrt{\frac{3}{16}(3-\eta^2)|a|^4 - \eta|a|^2 - 1} \tag{5.5}$$

where, $\sigma^{\pm}$ indicates the saddle node bifurcation points where the stable and unstable nontrivial solutions meet.

5.2. DYNAMICS OF PARAMETRICALLY DRIVEN DUFFING OSCIL-
LATOR WITH NONLINEAR DAMPING

In this section, an overview is given on the dynamics of a parametrically driven Duffing oscillator with nonlinear damping. The oscillator is actuated parametrically. The detailed derivation and response curves are shown in the appendix D.

The normalized equation of motion of such a system is given by,

$$\ddot{x} + Q^{-1}\dot{x} + x[1 + f_p\cos(\Omega_p\tau)] + x^2 + \eta x^2\dot{x} + x^3 = f\cos(\Omega_d\tau) \tag{5.6}$$

Where, $f_p = \frac{F_p}{k}$ is the scaled parametric drive amplitude. $\Omega_p = \frac{\omega_p}{\omega_0}$ is the nondimensional parametric pump frequency and $\Omega_d = \frac{\omega_d}{\omega_0}$ is the nondimensional direct drive frequency.

The frequency response equation to system 5.6 is obtained by using perturbation techniques and by casting the system into slow variables. It is given by,

$$\frac{-\delta a*}{2} = \left[\left(\frac{3}{4}|a|^2 - \sigma_p\right) + i\left(1 + \frac{\eta}{4}|a|^2\right)\right]a \tag{5.7}$$

From the above equation, we see that zero motion state i.e., a = 0 is always a possible solution to the equation irrespective of the excitation frequency σ_p. The nontrivial response and

phase equations are obtained from equation 5.7 and are given by,

$$\frac{\delta^2}{4} = \left(\sigma_p - \frac{3}{4}|a|^2\right)^2 + \left(1 + \frac{\eta}{4}|a|^2\right)^2 \tag{5.8}$$

$$tan(2\phi) = \frac{1 + \frac{\eta}{4}|a|^2}{\frac{3}{4}|a|^2 - \sigma_p} \tag{5.9}$$

From equation 5.2, it can be seen that nonlinear damping acts to saturate the parametric response. The response of the system rises until a limit point is reached and a saddle node bifurcation occurs. This is in contrast to the parametrically excited system with linear damping, where the response grows indefinitely. The equation for saddle node bifurcations is given by,

$$\sigma_p^\pm = \frac{\delta}{2}\sqrt{1 + \left(\frac{3}{\eta}\right)} - \frac{3}{\eta} \tag{5.10}$$

where, $\sigma_p^\pm$ indicates the points where the stable and unstable nontrivial solutions meet. From frequencies above $\sigma_p^\pm$ the only solution available is the zero amplitude solution, a = 0.

The onset of parametric response is indicated by the presence of period doubling bifurcations as discussed in chapter 3. The equation for period doubling bifurcations is given by,

$$\sigma_{PD} = \pm\sqrt{(\delta/2)^2 - 1} \tag{5.11}$$

where, σ_{PD} indicates the point at which trivial and nontrivial solutions meet.

As discussed so far, the effects of nonlinear damping on direct and parametric responses differ significantly. Hence, by studying the dynamics and understanding the physics behind such nonlinear effects, one can develop a single governing equation of motion. This single equation can then be used to explain both the direct and parametric responses. In the subsequent sections, this equation is employed to numerically fit the experimental curves obtained for a graphene nanodrum resonator.

5.3. EXPERIMENTAL RESULTS

The Duffing and parametric experimental curves for both forward and reverse sweep are as shown in Figures 5.1, 5.2 and 5.3, 5.4 respectively. These figures correspond to first experimental data set obtained on a optothermally excited 5 micron diameter single layer graphene nanoresonator. Similarly, a second data set results are discussed in appendix E.
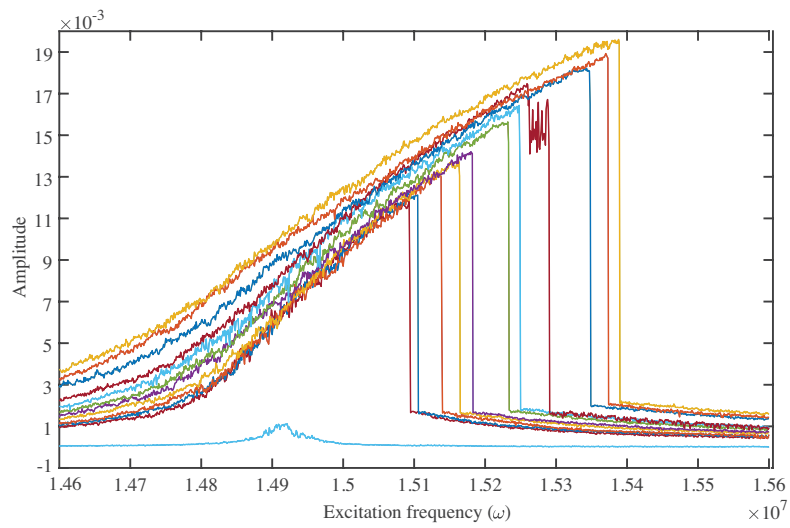
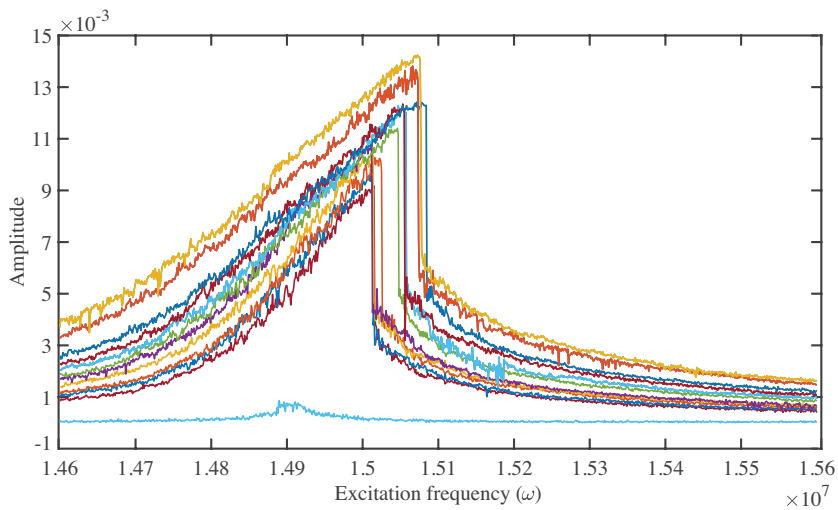Figure 5.1: Duffing experimental response curves: Forward sweep

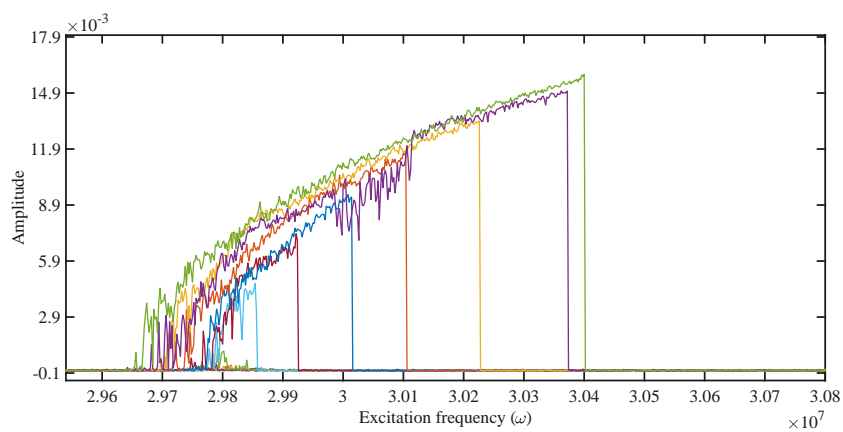Figure 5.2: Duffing experimental response curves: Backward sweep.

Figure 5.3: Parametric experimental response curves: Forward sweep
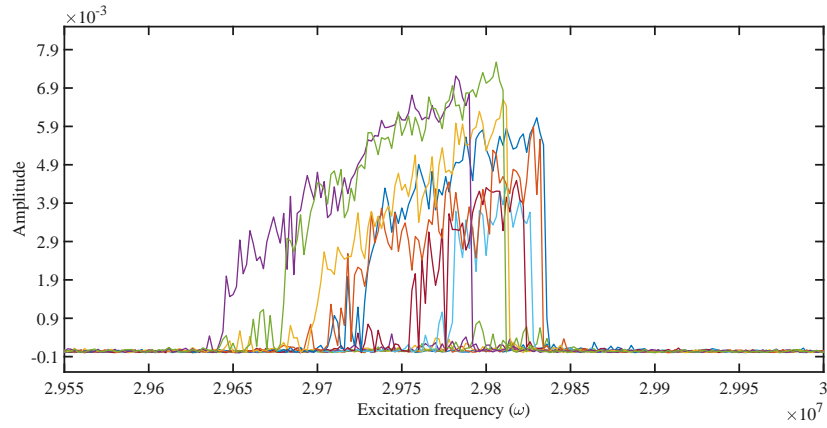
Figure 5.4: Parametric experimental response curves: Backward sweep.

5.4. MODELING AND SIMULATION

The experimental setup and the interferometer setup are explained in section 1.5.2. A 5 μm diameter monolayer graphene nanodrum resonators are synthesized as explained in section 1.6. The parametric and direct drive are achieved by a modulated blue diode laser impinging on the membrane. The actuation is due to the periodic laser heating and cooling of the membrane, which in turn induces a vibratory motion at the driving frequency. A red Helium-Neon laser is used to read the motion of the membrane in a Fabry-Perot type optical interference. The transmission gain from the blue diode laser modulation to the signal detected by the photodetector is measured using a network analyzer. The direct and parametric resonances shown in Figures 5.1 & 5.2 and 5.3 & 5.4 are obtained by modulating the blue diode laser at driving frequencies $\omega = \omega_0$ and $\omega = 2\omega_0$ respectively. The experiment is repeated at different driving powers and on different graphene drums all of same diameter. A set of experimental curves obtained for each graphene drum is treated as one data set in the subsequent sections.

The modeling approach adopted is 'brute force method' where, each coefficient in the governing equation of motion is varied until a proper fit to the experimental curve is obtained. The reason for this approach is that due to the unknown mass of the single layer graphene membrane. Without the mass value, the normalized coefficients cannot be calculated using analytical relations. Furthermore, due to the unknown optical transduction factor present between the signal (Volts) measured by the VNA during the experiments and the actual motion of the membrane in physical units (nano meters), it becomes difficult to characterize the mass of the membrane using Brownian motion.

5.4.1. FITTING CRITERION

The normalized equations of motion obtained in the previous chapters for the Duffing-Mathieu model with and without nonlinear damping is simulated using continuation software package *AUTO* to match the following criterion.

Simple Harmonic Response Fit

1. For low power responses, a normalized simple harmonic oscillator model is fitted to obtain an initial approximation of linear damping coefficient (μ) or the quality factor (Q) and the amplitude of excitation (f).

Duffing Response Fit

2. At Ω away from 1, the offset of low amplitude Duffing solution along the y-axis is initially matched by varying the amplitude of excitation (f).

3. Once the desired offset is obtained, the coefficient of cubic stiffness (γ) is varied to match the slope of the Duffing response obtained during the forward sweep in the experiment.

4. After obtaining the coefficient of cubic stiffness (γ), the peak amplitude of Duffing response is matched by changing the amount of linear (μ) and/or nonlinear damping (ν) coefficients of the system.

Parametric Response Fit

5. The points of bifurcation, causing the solution to branch out from zero amplitude solution to stable and unstable high amplitude solutions are matched by varying the parametric drive (δ) and the amount of linear damping in the system (μ).

6. The peak amplitude of the parametric response is matched by varying the nonlinear damping coefficient (η).

The above procedure is repeated and the coefficient values are optimized till all the values obtained in the final model are within acceptable error margins and are able to fit both Duffing and parametric responses.

5.5. CURVE FITTING USING DUFFING-MATHIEU MODEL WITH LINEAR DAMPING

In this section, we look into the theoretical fit obtained by using Duffing-Mathieu model with linear damping whose dynamics were discussed in sections 4.3 and 3.3. The dimensionless equation is given by,

$$\ddot{x} + \mu\dot{x} + x + \delta\cos(\Omega\tau)x + \gamma x^3 = f\cos(\Omega\tau) \tag{5.12}$$

In order to arrive at the above equation from equation 4.8, the symmetry breaking non-linearities such as (x^2) and the static excitation term (F_0) introduced by the geometric imperfection is ignored. This assumption is valid since, the direct response as seen in the experimental curves 5.1 is mostly dominated by the stiffening nonlinearity indicating that the contribution from the x^2 is negligible. The above model is used to fit the first set of experimental response curves obtained from a 5 micron diameter graphene nanodrum resonator with a fundamental frequency of $\omega_0 = 14.913\,\text{MHz}$. Such a theoretical fit obtained for both Duffing and parametric responses is as shown in Figure 5.5.
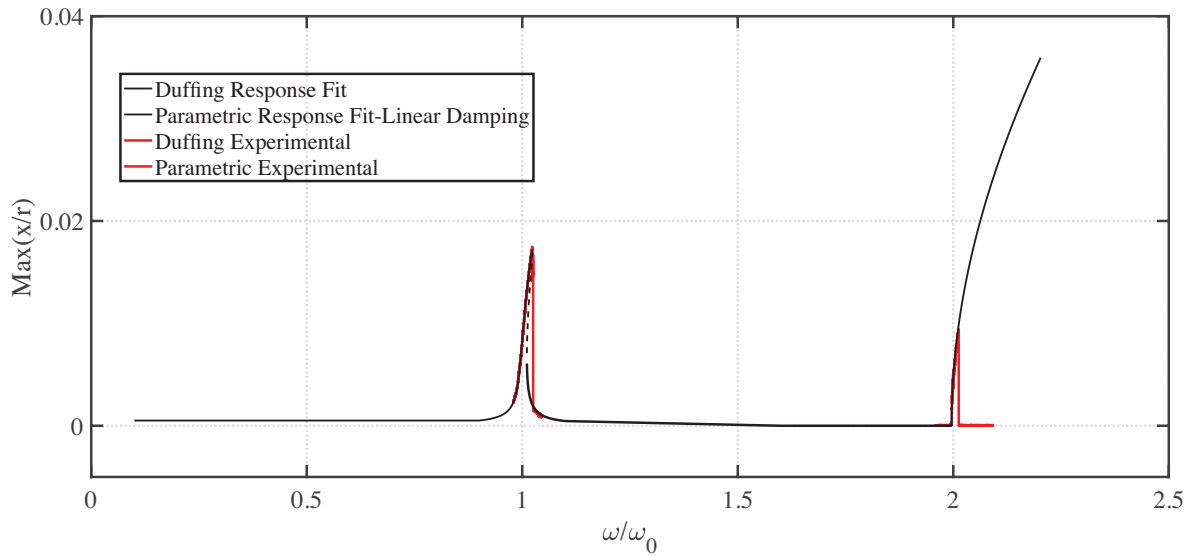
Figure 5.5: Theoretical fitting of experimental response using Duffing-Mathieu model with linear damping
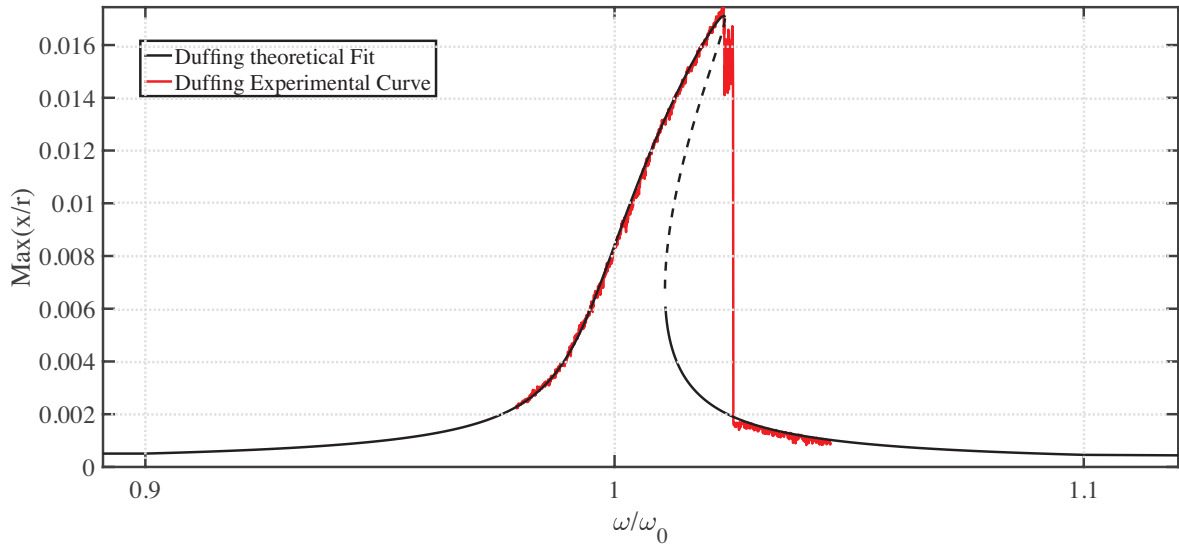

Figure 5.6: Theoretical fitting of forward sweep Duffing response obtained from experiments using Duffing-Mathieu model with linear damping.

As seen from the curve fitting shown in Figure 5.6 & 5.7, although the model can fit the experimental duffing response to a high degree of accuracy, it fails to account for the drop in amplitude of the parametric response. This is due to the different effects of linear damping on direct and parametric response as discussed in section 3.4. The parametric response grows without bound as seen in Figure 5.7 contrary to the experimental response. Therefore, one can conclude that the Duffing-Mathieu Model with low linear damping given by equation 5.12 fails to capture the global dynamics of both direct and parametric responses.
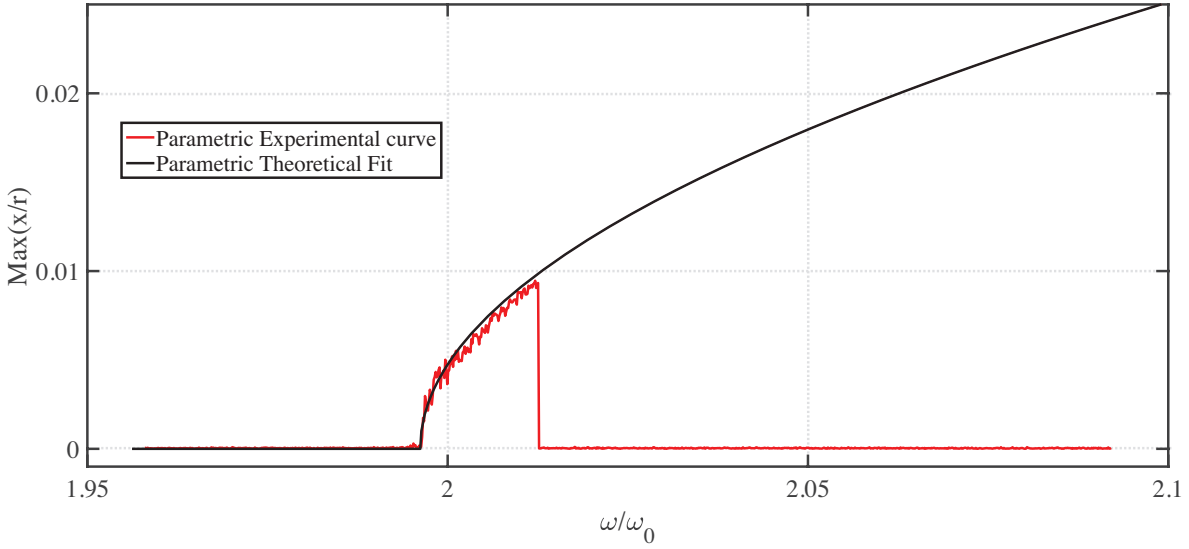
Figure 5.7: Theoretical fitting of forward sweep parametric response obtained from experiments using Duffing-Mathieu model with linear damping.

5.6. DUFFING-MATHIEU MODEL WITH NONLINEAR DAMPING

In this section, we look into the theoretical fit obtained by using Duffing-Mathieu model with nonlinear damping whose dynamics are discussed in sections D.1 and D.2 of the appendix.

The dimensionless equation is given by,

$$\ddot{x} + \mu\dot{x} + \eta x^2\dot{x} + x + \delta\cos(\Omega\tau)x + \gamma x^3 = f\cos(\Omega\tau) \tag{5.13}$$

The above model is used to fit the first set of experimental response curves obtained from a 5 micron diameter graphene nanodrum resonator with a fundamental frequency of $\omega_0 = 14.913$MHz.

The simple harmonic resonance obtained at low driving powers is fitted with an oscillator model to extract the quality factor for the system and this value is used as initial approximation of linear damping (μ) present in the system.

Once the initial approximation for the linear damping present in the system is obtained. The experimental response curves at higher driving powers which give rise to large amplitude curves are simulated. The theoretical model given by equation 5.13 is used to fit these curves based on the criterion discussed in the section 5.4.1. As seen from theoretical fit given by Figures 5.9 and 5.10, the model can fit the forward and backward sweeps of Duffing and parametric response with a high degree of accuracy at low power levels.
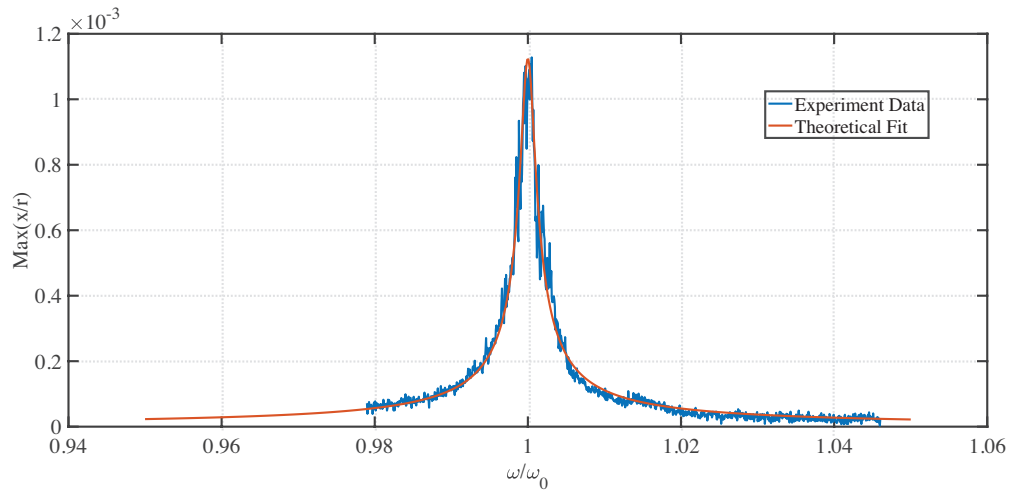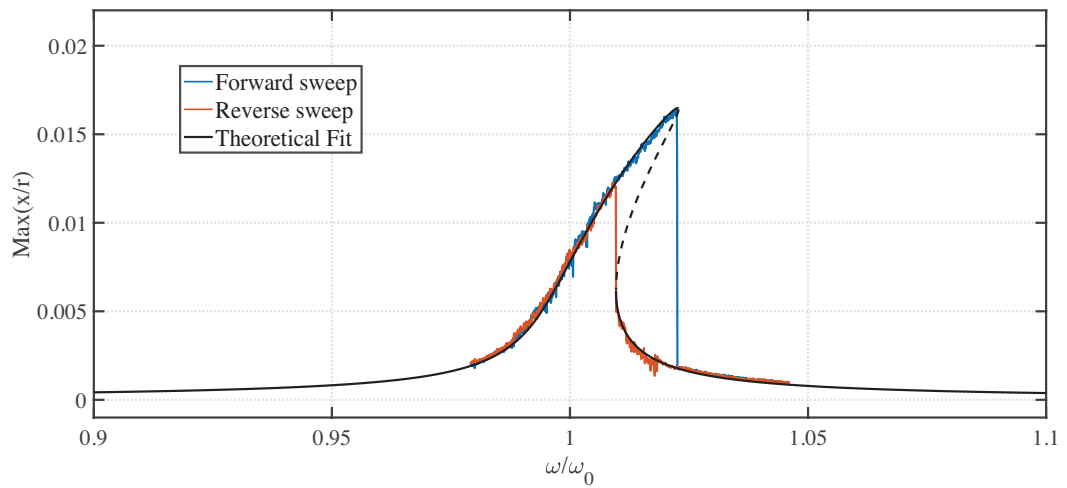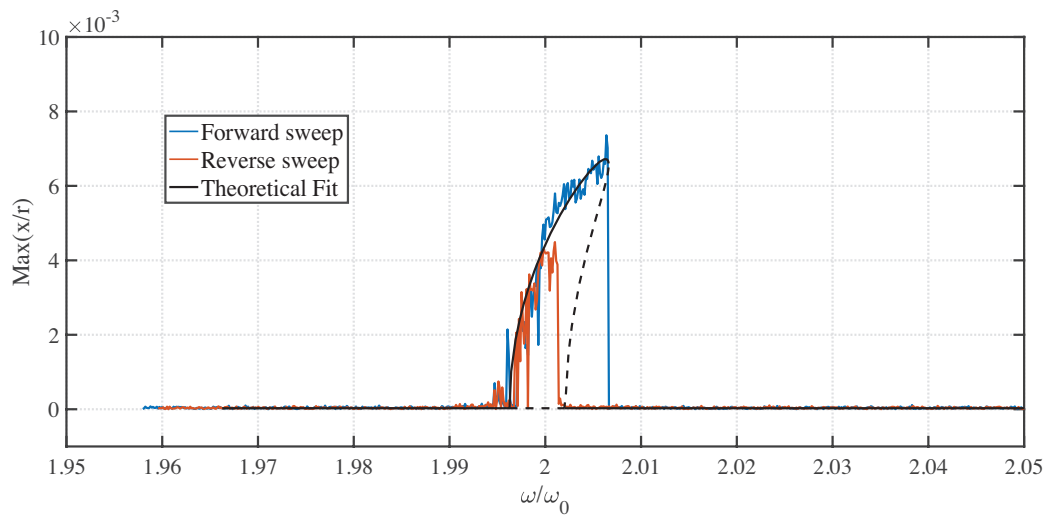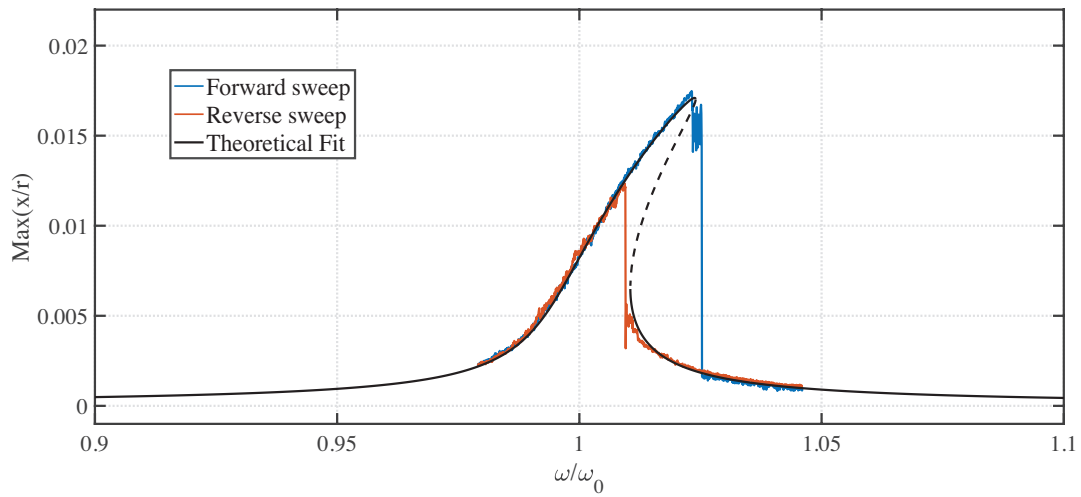
Figure 5.8: Simple harmonic resonance at V_{rms}=0.0071 V

(a) Duffing response.

(b) Parametric response.

Figure 5.9: Theoretical fit of experimental response at V_{rms}= 0.2508 V using Duffing-Mathieu model with nonlinear damping.

(a) Duffing response
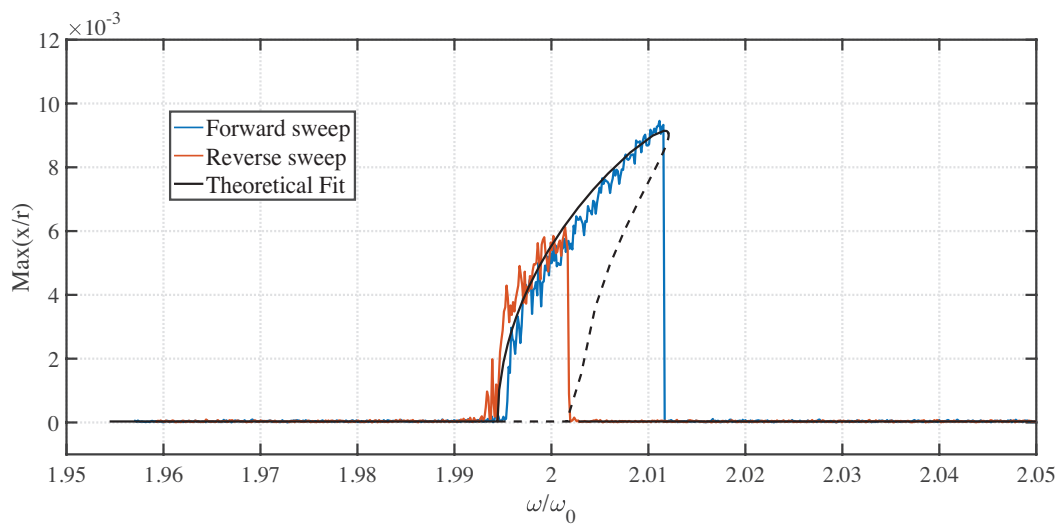

(b) Parametric response

Figure 5.10: Theoretical fit of experimental response at V_{rms}= 0.2815 V using Duffing-Mathieu model with nonlinear damping.

But at higher powers, the fit has high accuracy in the forward sweep for both Duffing and parametric responses, but there is a discrepancy in the fit for the reverse sweeps. This is more predominant in the parametric response, as shown with a red dashed rectangle in Figures 5.11, 5.12 and 5.13.

(a) Duffing response

(b) Parametric response

Figure 5.11: Theoretical fit of experimental response at $V_{rms} = 0.3544\,V$ using Duffing-Mathieu model with nonlinear damping.

(a) Duffing response

(b) Parametric response

Figure 5.12: Theoretical fit of experimental response at $V_{rms}= 0.3976\,V$ using Duffing-Mathieu model with nonlinear damping.

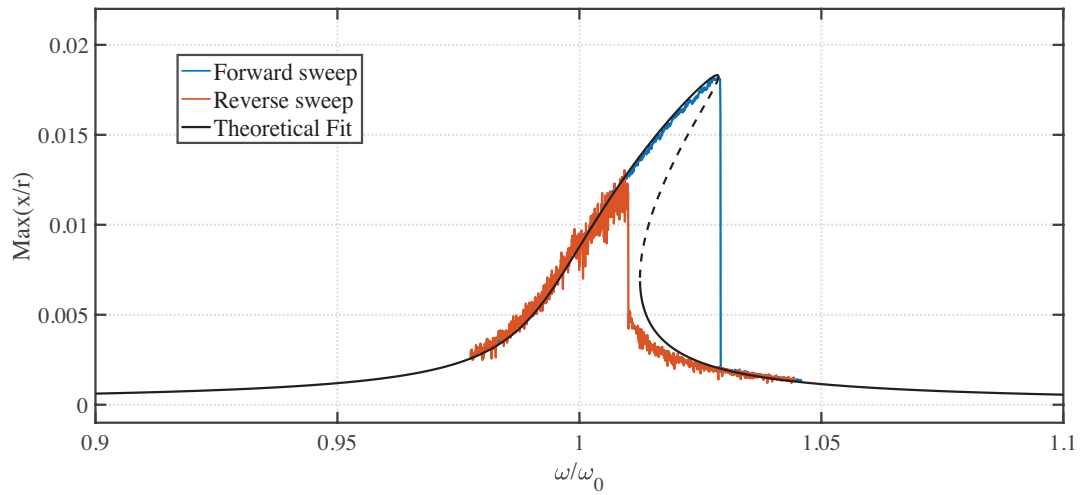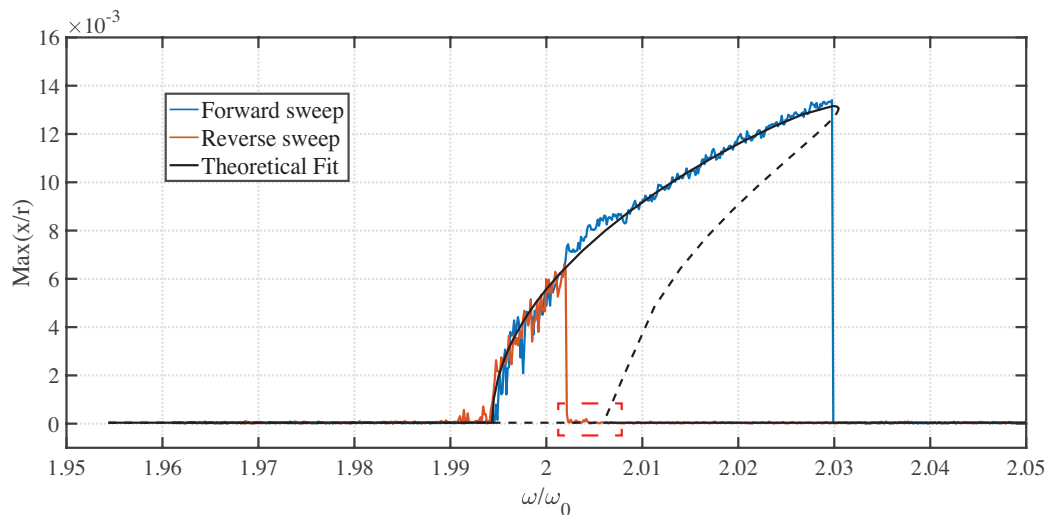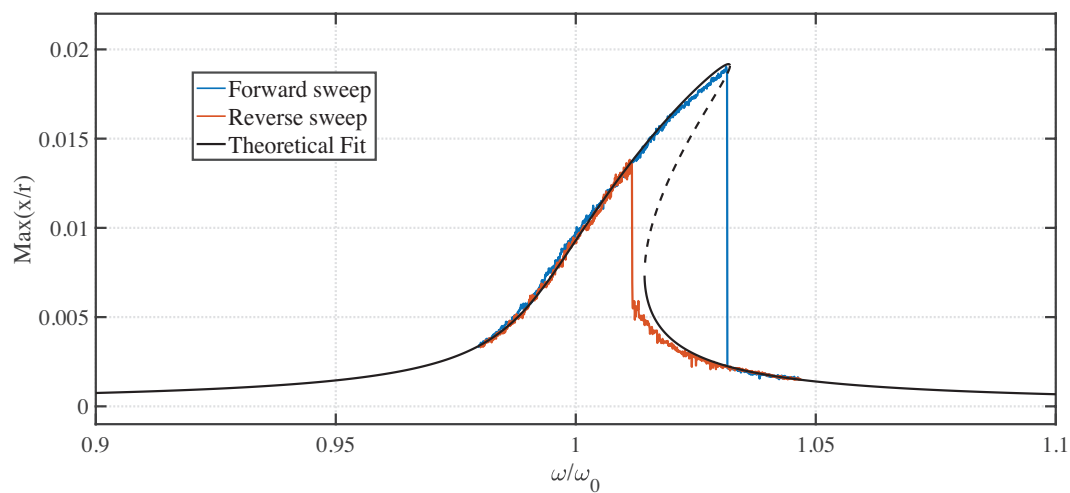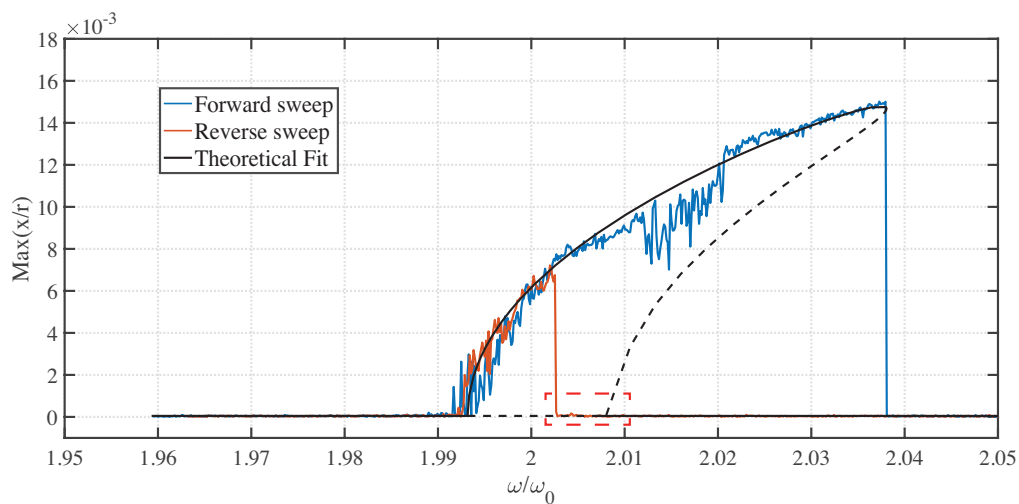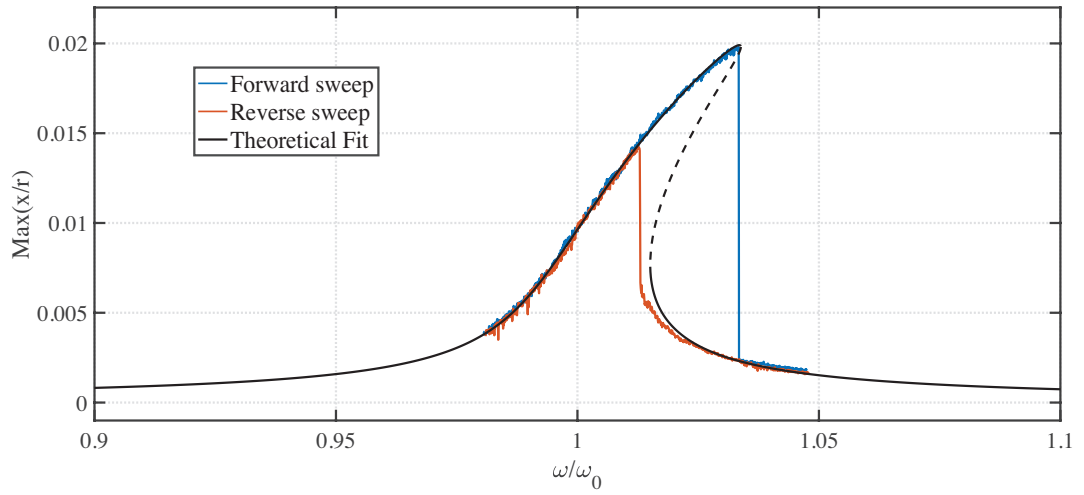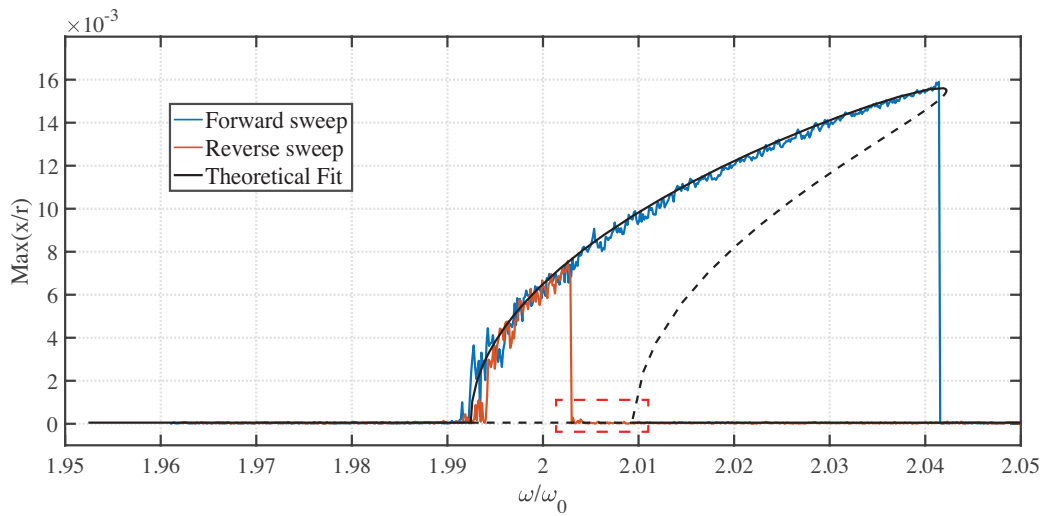(a) Forward sweep

(b) Backward sweep.

Figure 5.13: Theoretical fit of experimental response at V_{rms}= 0.4462 V using Duffing-Mathieu model with nonlinear damping.

This discrepancy from the current model can be attributed to missing damping terms from the current model. This is due to the fact that, the points of period doubling bifurcations mainly depend on the amplitude of parametric drive term (δ) and the amount of linear damping present (μ) in the system. This is discussed in depth in appendix D.2. From Figure 5.15, there is almost a linear relationship between the applied voltage signal in the experiments and the parametric drive amplitude term obtained from curve fitting. This is also true for the direct excitation term f as shown in Figure 5.14. This indicates that the transduction factors between them are also linear in nature. However, there is no direct way to obtain such a relationship for the damping. From the modeling point of view, this suggests that, there could be other unknown damping mechanisms involved, which are not taken into account in the current model.
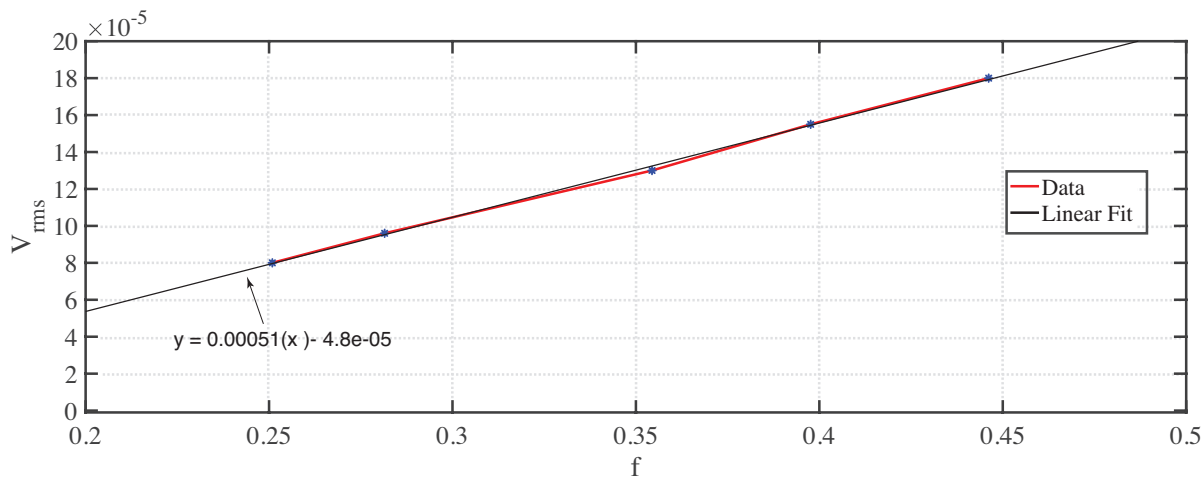
Figure 5.14: Plot of applied voltage signal V_{rms} against amplitude of direct drive (f) from theoretical fit
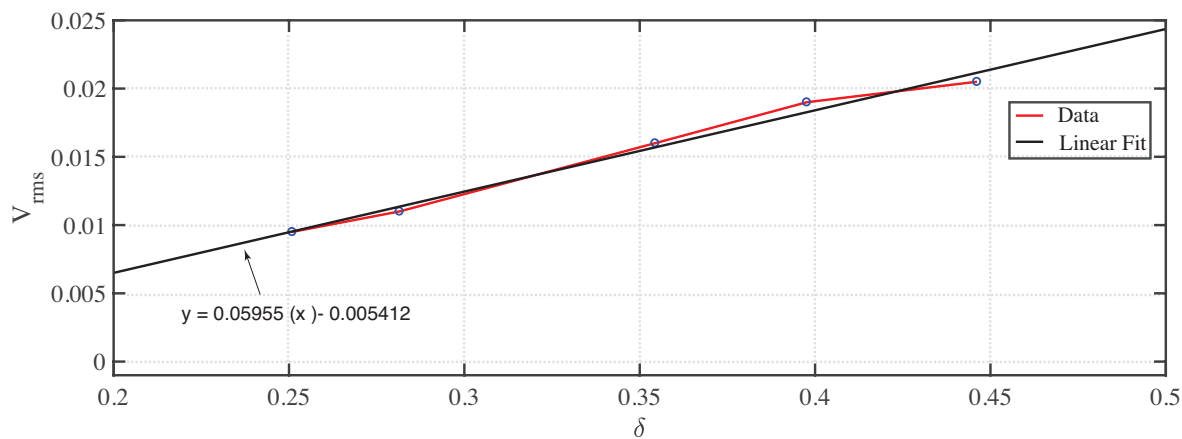
Figure 5.15: Plot of applied voltage signal V_{rms} against amplitude of parametric drive (δ) from theoretical fit

However, there is no concrete evidence to support that, damping alone could be the reason for the discrepancy. From the physics perspective, there are other nonlinear phenomena which can cause such a discrepancy like, the effect of wrinkles, non-uniform tension in the membrane, uneven heating of the membrane and the frequency noise. Since these effects are not taken into account in the model, further experimentation and modeling which includes such effects could provide more information regarding their influence on the system dynamics.

In appendix C, a preliminary analysis is carried out into some of the higher order damping nonlinearities induced by various mechanisms and their effect on the dynamics of the system. It is concluded that, adding these higher order damping terms does not alter the response curves in a fundamental way. They merely conspire to renormalize the effective values of coefficients used in the original equation of motion. Thus, without any particular model and physical reason at hand, it is difficult to discern the existence of such terms in the equation.

Table 5.1 shows the list of coefficients used in the model for fitting the experimental response curves. Here, the subscript d and p represent the values used to fit the Duffing and parametric responses. It should be noted that the average values of $\nu = 75$ and $\gamma = 225$ can be used to fit all the experimental responses with reasonable accuracy. The maximum variation for the nonlinear damping coefficient (ν) is 12.5% and minimum variation is 5%. Similarly, for cubic stiffness coefficient, the maximum variation is 2.1 %. These variations are attributed to measurement inaccuracies.

Experimental Curve	Duffing response fit				Parametric response fit		
V_{rms} (V)	μ	ν_d	γ_{d}	$f \times 10^{-5}$	ν_p	γ_{p}	$\delta \times 10^{-2}$
0.2508	0.0045	70	225	8	76	215	1.06
0.2815	0.0045	72	220	9.2	76	220	1.22
0.3544	0.0045	74	230	11.7	79	225	1.6
0.3976	0.0045	76	230	14.2	80	225	1.8
0.4462	0.0045	76	230	15.5	80	225	1.93

Table 5.1: Table of coefficients used for numerical simulation of first data set.

5.6.1. Transition Curves

The Figures 5.16 are the transition curves for different sets of experimental data obtained from a 5 micron diameter graphene resonator. Figure 5.16 (a) and 5.16 (b) correspond to the first and second experimental data respectively. In Figure 5.16 comparison is made between the transition curve obtained from experimental data and theoretical Duffing-Mathieu model with nonlinear damping. As seen from the plots, the theoretical model predicts a symmetrical behavior whereas, the experimental transition curve is asymmetrical. The forward sweeps of both theory and experiments match. Where as, there is a mismatch between the reverse sweeps as seen before. This is seen in both the data sets and confirms the qualitative dynamics is the same for both cases. This is a very important indicator of damping terms missing from equation of motion or other underlying physics which is not taken into account in the modeling. The frequency response curves for the second experimental data set are shown in appendix E.
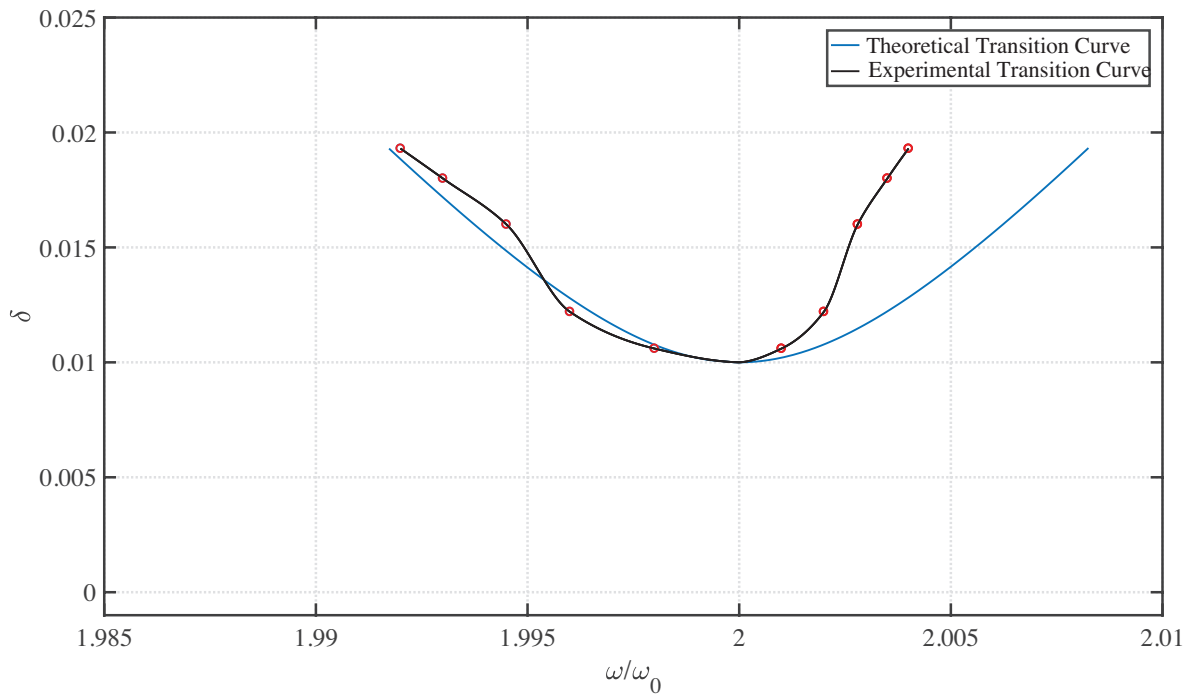
(a) Experimental data set 1
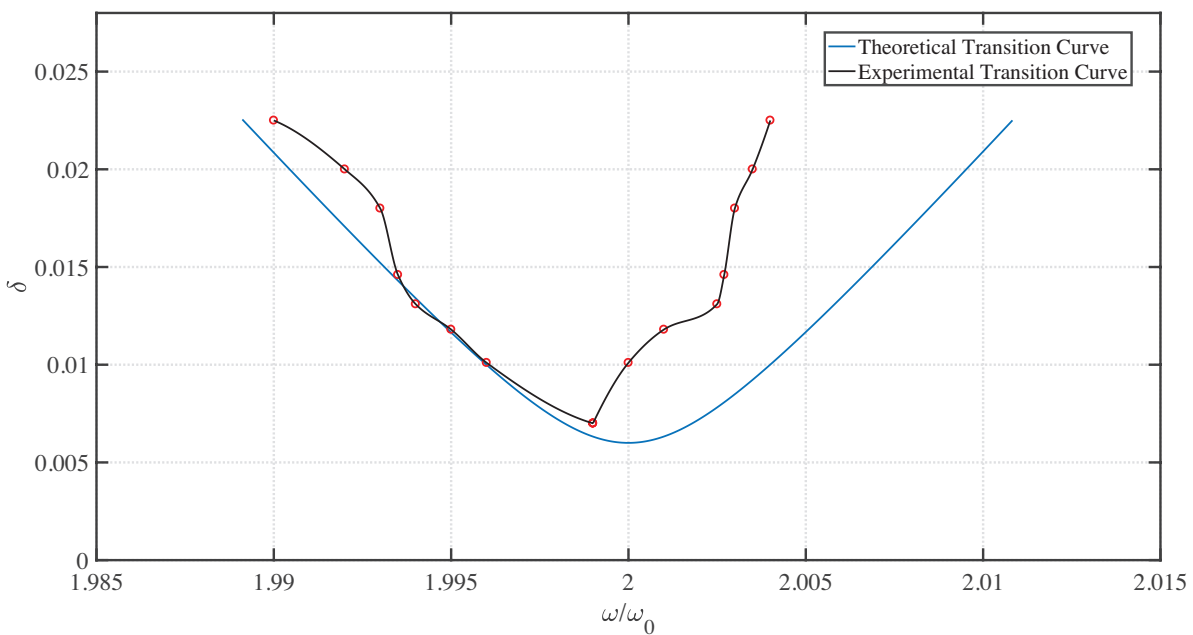
(b) Experimental data set 2

Figure 5.16: Comparison of experimental and theoretical transition curves for two data sets.

5.7. CHARACTERIZATION OF GRAPHENE MATERIAL PROPERTIES

Graphene material properties can be characterized by studying the dynamics of parametric excitation in optothermally actuated graphene nanoresonators. By using the models developed earlier and from the experimental data, one can extract properties such as thermal expansion coefficient (α), thermal time constant (τ) and optical Power absorbed (P_{abs}) by the graphene membrane. Some of these parameters such as thermal time constant and

optical power absorbed are dependent on the number of layers of graphene.

The procedure for extracting parameters is as follows,

1. A theoretical model given by equation 5.6 is used to fit the experimental response curve.

$$m\ddot{\tilde{x}} + c_1\dot{\tilde{x}} + k\tilde{x} + F_p\cos(\omega_p t)\tilde{x} + k_2\tilde{x}^2 + c_2\tilde{x}^2\dot{\tilde{x}} + k_3\tilde{x}^3 = F\cos\omega_d t$$

2. From section 3.1, we know that the parametric drive amplitude (F_p) is due to periodic heating of the membrane and is given by the equation 3.17.

$$F_p = \frac{k_p\,\alpha\,P_{abs}\,\tau^2\,\omega}{C(\tau^2\omega^2 + 1)}$$

Where, k_p is a constant. As seen from the above equation, the parametric drive (F_p) is a function of 3 material properties, power absorbed (P_{abs}), thermal expansion coefficient (α) and thermal time constant (τ). i.e $F_p = \chi(P_{abs}, \alpha, \tau)$.

3. Since there is one equation and 3 variables, we can extract only one material property from the above equation, at any given point of time. This is done by treating any of the other 2 properties as constant and using the third as a fitting parameter. From this method, one can obtain a range of values for which parametric resonance is observed with small detuning. Out of these range of values, one can find the exact value that matches the experimental response by curve fitting process. This provides a way to characterize material properties based on the dynamics of parametric excitation seen in optically actuated graphene nanoresonators.

An illustration of the method using theoretical model is shown below.

Consider a laser with a power of 2 mW and absorption coefficient (β_{abs}) of 7.34% [50], then the absorbed power is given by equation 4.1 and is calculated to be 1.46×10^{-4} W. From literature, the standard values of thermal expansion coefficient is given by $\alpha = -7.5 \times 10^{-6}\,\mathrm{K}^{-1}$ [51] and the thermal time constant is given by τ=100 ns [37].

By using the graphene resonator parameters given in table 3.2. Numerical simulation of equation 5.6 is performed by brute force method. Through the simulation, we find the critical value of parametric drive required for exciting system into resonance to be F_p=$3.54 \times 10^{16}\,\mathrm{N\,m}^{-1}$.

Now assuming the parameters α and τ to be constants and equal to $-7.5 \times 10^{-6}\,\mathrm{K}^{-1}$ and 100 ns respectively. The power absorbed (P_{abs}) by the membrane is treated as an unknown parameter. The strength of parametric drive required to excite the system into resonance is given by equation 3.17. In this equation, the only unknown is the parameter currently is P_{abs} as shown below.

$$F_p = P_{abs} \times 2.39 \times 10^{21}$$

Substituting the value of F_p obtained from brute force simulation i.e, $F_p = 3.54 \times 10^{16}$ We obtain,

$$P_{abs} = \frac{3.54 \times 10^{16}}{2.39 \times 10^{21}}$$
$$P_{abs} = 14.7 \mu W$$

In order to verify the above value obtained for power absorbed, the equation of motion 5.6 is simulated again using the continuation software package *AUTO*. This is done by treating P_{abs} as a continuation parameter and it is seen that at $P_{abs} = 14.7 \mu W$ indeed parmetric resonance is achieved.

Similarly, the above process can be repeated for the other two parameters as well. By treating P_{abs} and τ as constants, we can extract thermal expansion coefficient. Whose value is found to be $\alpha = -7.62 \times 10^{-7} \, K^{-1}$ Or by treating P_{abs} and α as constants, we can extract thermal time constant. Whose value is found to be $\tau = 2 \, ns$.

The above illustration is based on the theoretical models and doesn't reflect the actual parameters. But as seen from the above values, we see that the thermal expansion coefficient is an order different and the power absorbed and thermal time constant is almost 2 orders different from the standard literature values. Once the model is improved to match the experimental results, the accuracy of parameter estimation can be significantly improved. This could provide a new direction to characterize material properties of graphene in future.

5.8. CONCLUSION

In this chapter, the responses from theoretical models are compared against the experimental data. It is concluded that models with low linear damping fail to capture the global dynamics of parametric excitation. Then, models with nonlinear damping are used to fit the experimental data and are shown to be excellent at simulating the experimental behavior during forward sweeps. But at higher driving powers a discrepancy is noticed in the prediction of points of bifurcations by the theoretical model, when compared with experiments. This difference is attributed to missing damping terms and/or other underlying physics missing from the model. This is shown clearly with the help of transition curves for two different data sets. Furthermore, some higher order nonlinearities are incorporated explicitly into equation of motion (see appendix C) and it is shown that these nonlinearities merely change the effective values of coefficients used in the original equation of motion. In this chapter, only a speculation is provided towards the potential reason behind such discrepancy. It requires more in depth research to uncover the actual physics behind the phenomenon. Finally, the application of studying the dynamics of parametric excitation in graphene nanodrums is illustrated in the form of material property characterization.

6

CONCLUSION AND DISCUSSION

6.1. ORIGIN OF DIRECT AND PARAMETRIC EXCITATION

As discussed in chapters 3 and 4, the physics behind parametric excitation could be explained due to periodic heating of the membrane by the laser which in turn modulates the stiffness of the membrane. Furthermore, this phenomena is modeled by considering the energy exchange in the form of Newton's law of cooling. Finally, an expression for the temperature modulated stiffness is obtained and its dependency on various material properties such as optical power absorbed by the membrane (P_{abs}), thermal expansion coefficient (α) and the thermal time constant (τ) is studied in depth.

The source of direct excitation is found to be the presence of initial geometric imperfection in the membrane. This deviation causes primary Duffing response at higher driving powers along with secondary superharmonic responses. The direct excitation is then modeled by assuming the deviation of the membrane from the flat configuration to be in the form of first fundamental vibration mode shape. This introduces a symmetry breaking nonlinearity (x^2) along with static (F_0) and dynamics excitation ($F\cos(\omega t)$) terms which were studied in depth mathematically by using perturbation techniques.

6.2. THEORETICAL MODELS

From the discussion in the previous chapters, it is clear that the Duffing-Mathieu model with linear damping can explain the direct response with a high degree of accuracy and also, predicts the onset of principal parametric resonance but fails to explain the global dynamics. It is seen that, in the linear damping model, the parametric response grows without bound, however, this is something that doesn't match with experimental observations. This disadvantage is overcome by including nonlinear damping arising from the material in the equation of motion. By performing numerical simulations, it is shown that the parametric response can be limited by the presence of nonlinear damping. The mathematical modeling provides insight into the influence of damping for achieving linear instability. It is shown that the critical drive threshold is dependent only on the amount of linear damping present in the system. Furthermore, the role played by the linear damping on the points of period doubling bifurcations is discussed.

The lack of accuracy in the fitting of Duffing-Mathieu model with nonlinear damping emerges during the reverse sweep cycle. The theoretical model predicts the period doubling at a higher frequency than that seen in the experiments. Exact reasons for this discrepancy is yet unknown. As seen in the chapter 5 and appendix E, the Duffing-Mathieu model with nonlinear damping is used to curve fit two different sets of data, in both the cases the qualitative dynamics remains the same. This indicates that the theoretical model needs some correction terms to accurately simulate the experimental behavior. However, potential reasons for this discrepancy could be due to additional damping terms missing from equation of motion or, it could be due to influence of alternative physics. This reasoning is further bolstered by the deviation seen in the transition curve plots. Furthermore, the effect of different nonlinear damping terms on the response of the system is studied in depth (refer appendix C) and it is concluded that these nonlinearities merely act to change the effective coefficient values in the original equation of motion. Thus, eliminating them as the cause of mismatch seen in the simulations.

6.2.1. Characterization of Graphene Properties

The parametric excitation caused by the modulated stiffness as a result of periodic heating could be used to extract thermal properties of graphene. It is shown that the onset of parametric resonance is inherently dependent on the strength of parametric drive and the amount of damping present in the system. Furthermore, the strength of parametric drive is dependent on material properties such as optical power absorbed by the membrane (P_{abs}), thermal expansion coefficient (α) and the thermal time constant (τ). These parameters could be extracted from the nonlinear response curves through curve fitting the experimental data. The parametric response also provides information on the amount of nonlinear damping present in the system. By knowing the transduction factors involved, the coefficient of nonlinear damping can be easily extracted. Finally, by further improving the theoretical model presented in the previous chapters, to account for the discrepancy seen in the reverse sweep, the accuracy of characterization process could be greatly enhanced. This methodology lays the foundation for future experiments.

6.3. Recommendations for Future Research

In this dissertation, the origins of parametric and direct excitation in optically actuated monolayer graphene resonators are explained. The influence of system parameters on achieving linear instability and the accuracy of linear and nonlinear damping models to simulate the experimental response is discussed. Furthermore, an illustration of material property characterization from parametric response is introduced. Finally, the advantages and disadvantages of simulating the dynamics of both direct and parametric responses using one differential equation is illustrated.

In this section, future recommendations for further research are proposed.

1. In the modeling of temperature filed responsible for parametric excitation, the model is simplified to have only temporal dependency. It would be interesting to include the spatial dependency of the temperature field to simulate for example uneven heating of the membrane.

2. The dilatation term is ignored in the heat conduction equation due to its low co-efficient of coupling in MEMS and NEMS devices. But, this dilatation term is also responsible for thermoelastic damping in the system and could be investigated to find the influence of such a term on the quality factor of single layer graphene resonators. It could also give an insight into the energy exchange during the nonlinear interaction between the mechanical and thermal modes.

3. The optical power source term, when modeled to be a function of spatial distribution, could introduce a plethora of nonlinearities in the governing differential equation, which could provide immense amount of information.

4. The appearance of parametric resonance in homodyne scheme could be explained based on the nonlinear optical transduction. He-Ne laser signal is used for detecting the motion of the membrane and the reflected intensity of this signal is a function of membrane vibration. By assuming the intensity to be a nonlinear function of the membrane vibration, the appearance of parametric resonance in homodyne scheme could be justified. This could provide a new direction for calibrating the amplitude of vibration in optically actuated graphene resonators [52].

5. From mathematical point of view, the Duffing-Mathieu model with nonlinear damping could be further improved by considering either macroscopic and or microscopic damping mechanisms to better explain the discrepancy seen in the curve fitting during reverse sweep.

6. From physics perspective, the origin of the discrepancy seen during the fitting of curves in reverse sweep could be due to the presence of wrinkles and uneven tension in the membrane. To predict the influence of such unknown mechanism, one needs further detailed experiments and novel mathematical equations.

7. The transduction factors involved in the conversion of optical signal to physical units of oscillation could help improve the curve fitting process by providing an initial estimate to the mass of the membrane. This can help automate the curve fitting process instead of brute force approach. This would also further give a better approximation of the material properties extracted from the experimental curves.

8. The material characterization process and accuracy of values obtained could be improved by utilizing the higher parametric modes [53].

9. An asymmetric reduced order model could be developed to study the nonlinear modal interactions in graphene nanodrum resonators. This could provide insight into the nature of energy exchange between in-plane and out of plane modes.

BIBLIOGRAPHY

[1] K. S. Novoselov, A. K. Geim, S. V. Morozov, D. Jiang, Y. Zhang, S. V. Dubonos, I. V. Grigorieva, and A. A. Firsov, *Electric field effect in atomically thin carbon films,* Science **306**, 666 (2004).

[2] C. Soldano, A. Mahmood, and E. Dujardin, *Production, properties and potential of graphene,* Carbon **48**, 2127 (2010).

[3] C. Chung, Y.-K. Kim, D. Shin, S.-R. Ryoo, B. H. Hong, and D.-H. Min, *Biomedical applications of graphene and graphene oxide,* Accounts of Chemical Research **46**, 2211 (2013).

[4] K. C. Kemp, H. Seema, M. Saleh, N. H. Le, K. Mahesh, V. Chandra, and K. S. Kim, *Environmental applications using graphene composites: water remediation and gas adsorption,* Nanoscale **5**, 3149 (2013).

[5] N. Bich Ha, Nguyen Van Hieu, *Two-dimensional hexagonal semiconductors beyond graphene,* Advances in Natural Sciences: Nanoscience and Nanotechnology **7**, 043001 (2016).

[6] J. Lee, Z. Wang, K. He, J. Shan, and P. X. L. Feng, *High frequency mos2 nanomechanical resonators,* ACS Nano **7**, 6086 (2013).

[7] A. K. Geim and K. S. Novoselov, *The rise of graphene,* Nature materials 6, 183 (2007).

[8] M. K. K. N. T. B. J. C. Meyer, A. K. Geim and S. Roth, *The structure of suspended graphene sheets,,* Nature 446, 60 (2007).

[9] N. P. K. S. N. A. C. Neto, F. Guinea and A. K. Geim, *The electronic properties of graphene,* Reviews of modern physics 81, 109 (2009).

[10] X. Zang, Q. Zhou, J. Chang, Y. Liu, and L. Lin, *Graphene and carbon nanotube (cnt) in mems/nems applications,* Microelectronic Engineering **132**, 192 (2015).

[11] T. Palacios, A. Hsu, and H. Wang, *Applications of graphene devices in rf communications,* IEEE Communications Magazine **48**, 122 (2010).

[12] A. K. Geim and K. S. Novoselov, *The rise of graphene,* Nat Mater **6**, 183 (2007).

[13] S. Bae, H. Kim, Y. Lee, X. Xu, J.-S. Park, Y. Zheng, J. Balakrishnan, T. Lei, H. Ri Kim, Y. I. Song, Y.-J. Kim, K. S. Kim, B. Ozyilmaz, J.-H. Ahn, B. H. Hong, and S. Iijima, *Roll-to-roll production of 30-inch graphene films for transparent electrodes,* Nat Nano **5**, 574 (2010).

[14] M. Poot and H. S. J. van der Zant, *Nanomechanical properties of few-layer graphene membranes,* Applied Physics Letters **92**, 063111 (2008).

[15] *https://www.extremetech.com/extreme/211437-extremetech-explains-what-is-graphene, .*

[16] J. S. Bunch, A. M. van der Zande, S. S. Verbridge, I. W. Frank, D. M. Tanenbaum, J. M. Parpia, H. G. Craighead, and P. L. McEuen, *Electromechanical resonators from graphene sheets,* Science **315**, 490 (2007).

[17] C. Chen, S. Rosenblatt, K. I. Bolotin, W. Kalb, P. Kim, I. Kymissis, H. L. Stormer, T. F. Heinz, and J. Hone, *Performance of monolayer graphene nanomechanical resonators with electrical readout,* Nat Nano **4**, 861 (2009).

[18] EichlerA, MoserJ, ChasteJ, ZdrojekM, I. Wilson Rae, and BachtoldA, *Nonlinear damping in mechanical resonators made from carbon nanotubes and graphene,* Nat Nano **6**, 339 (2011).

[19] T. Natsuki, J.-X. Shi, and Q.-Q. Ni, *Vibration analysis of nanomechanical mass sensor using double-layered graphene sheets resonators,* Journal of Applied Physics **114**, 094307 (2013).

[20] R. J. Dolleman, *Graphene Based Pressure Sensors: Resonant Pressure Transduction Using Atomically Thin Materials,* Master's thesis, Delft University of Technology (2014).

[21] H. Tian, Y. Shu, X.-F. Wang, M. A. Mohammad, Z. Bie, Q.-Y. Xie, C. Li, W.-T. Mi, Y. Yang, and T.-L. Ren, *A graphene-based resistive pressure sensor with record-high sensitivity in a wide pressure range,* **5**, 8603 (2015).

[22] S. S. Varghese, S. Lonkar, K. K. Singh, S. Swaminathan, and A. Abdala, *Recent advances in graphene based gas sensors,* Sensors and Actuators B: Chemical **218**, 160 (2015).

[23] S. Schmid, L. G. Villanueva, and M. L. Roukes, *Fundamentals of Nanomechanical Resonators* (Springer, 2016).

[24] J. M. Gere and B. J. Goodno, *Mechanics of Materials* (Cengage Learning, 2009).

[25] D. Davidovikj, F. Alijani, S. J. Cartamil-Bueno, H. S. J. van der Zant, M. Amabili, and P. G. Steeneken., *Young's modulus of 2d materials extracted from their nonlinear dynamic response,* arXiv:1704.05433 (2017).

[26] I. Kozinsky, H. W. C. Postma, I. Bargatin, and M. L. Roukes, *Tuning nonlinearity, dynamic range, and frequency of nanomechanical resonators,* Applied Physics Letters **88**, 253101 (2006).

[27] W. Zhang, R. Baskaran, and K. Turner, *Tuning the dynamic behavior of parametric resonance in a micromechanical oscillator,* Applied Physics Letters **82**, 130 (2003).

[28] L. G. Villanueva, R. B. Karabalin, M. H. Matheny, D. Chi, J. E. Sader, and M. L. Roukes, *Nonlinearity in nanomechanical cantilevers,* Physical Review B **87**, 024304 (2013).

[29] J. F. Rhoads, S. W. Shaw, and K. L. Turner, *Nonlinear dynamics and its applications in micro- and nanoresonators,* Journal of Dynamic Systems, Measurement, and Control **132**, 034001 (2010).

[30] M. H. Matheny, L. G. Villanueva, R. B. Karabalin, J. E. Sader, and M. L. Roukes, *Nonlinear mode-coupling in nanomechanical systems,* Nano Letters **13**, 1622 (2013).

[31] R. Lifshitz and M. C. Cross, *Nonlinear dynamics of nanomechanical and microme-chanical resonators,* Nonlinear Dynamics and Complexity: (2009).

[32] S. Zaitsev, O. Shtempluck, E. Buks, and O. Gottlieb, *Nonlinear damping in a microme-chanical oscillator,* Nonlinear Dynamics **67**, 859 (2012).

[33] Z. Wei, Z. Qiang, Z. Meng-Qiang, and K. Luise Theil, *Direct writing on graphene paper by manipulating electrons as invisible ink,* Nanotechnology **24**, 275301 (2013).

[34] R. Raccichini, A. Varzi, S. Passerini, and B. Scrosati, *The role of graphene for electro-chemical energy storage,* Nat Mater **14**, 271 (2015).

[35] R. V. LEEUWEN, *NANOSCALE MECHANICAL RESONATORS AND OSCILLATORS,* Ph.D. thesis, Technische Universiteit Delft (2015).

[36] C. Chen, S. Rosenblatt, K. I. Bolotin, W. Kalb, P. Kim, I. Kymissis, H. L. Stormer, T. F. Heinz, and J. Hone, *Performance of monolayer graphene nanomechanical resonators with electrical readout,* Nat Nano **4**, 861 (2009).

[37] D. Robin J, H. Samer, D. Davidovikj, S. J. Cartamil-Bueno, H. S. J. van der Zant, and P. G. Steeneken., *Optomechanics for thermal characterization of suspended graphene,* Arxiv (2017).

[38] J.N.Reddy, *Theory and Analysis of Elastic plates and Shells* (C, 2006).

[39] D. Szilard, *Theories and Applications of Plate Analysis : Classical, Numerical and Engineering Methods* (Wiley, 2004).

[40] R. B. H. Mohammad Reza Eslami, *Thermal Stresses – Advanced Theory and Applications* (Springer, 2008).

[41] M. Amabili, *Nonlinear Vibrations and Stability of Shells and Plates* (Cambridge University Press, 2008).

[42] K. L. Turner, S. A. Miller, P. G. Hartwell, N. C. MacDonald, S. H. Strogatz, and S. G. Adams, *Five parametric resonances in a microelectromechanical system,* Nature **396**, 149 (1998).

[43] W. F. Faris, *Nonlinear Dynamics of Annular and Circular Plates under Thermal and Electrical Loadings,* Ph.D. thesis, Virginia Polytechnic Institute and State University (2003).

[44] A. H. Nayfeh, *Introduction to perturbation techniques* (Wiley, 1993).

[45] M. V. Requa, *Parametric Resonance in Microcantilevers with Application in Mass Sensing,* Ph.D. thesis, UNIVERSITY OF CALIFORNIA (2006).

[46] A. hasan Nayfeh and D. T. Mook, *Non-linear oscillations* (Wiley, 1995).

[47] A. H. Nayfeh, *Applied nonlinear dynamics* (Wiley, 1995).

[48] E. J. Doedel, A. R. Champneys, T. F. Fairgrieve, Y. A. Kuznetsov, B. Sandstede, and X. Wang, *Auto 97: Continuation and bifurcation software for ordinary differential equations,* (1998).

[49] I. Kovacic, *The Duffing Equation: Nonlinear Oscillators and Their Behaviour* (Wiley, 2011).

[50] R. R. Nair, P. Blake, A. N. Grigorenko, K. S. Novoselov, T. J. Booth, T. Stauber, N. M. R. Peres, and A. K. Geim, *Fine structure constant defines visual transparency of graphene,* Science **320**, 1308 (2008).

[51] S. Vibhor, S. Shamashis, S. S. Hari, D. Rohan, A. Adrien, D. Sajal, P. Prita, and M. D. Mandar, *Probing thermal expansion of graphene and modal dispersion at low-temperature using graphene nanoelectromechanical systems resonators,* Nanotechnology **21**, 165204 (2010).

[52] D. Robin J, D. Davidovikj, H. S. J. van der Zant, and P. G. Steeneken., *Calibrating the amplitude and equilibrium position of graphene resonators by nonlinear optical transduction,* (in progress) (2017).

[53] D. Robin J, H. Samer, C. Abhilash, A. Farbod, H. S. J. van der Zant, and P. G. Steeneken., *Multi-mode parametric resonances and amplification of graphene resonators,* (in progress) (2017).

[54] A. Olkhovets, D. W. Carr, J. M. Parpia, and H. G. Craighead, *Non-degenerate nanomechanical parametric amplifier,* Technical Digest. MEMS 2001. , 298 ((2001).).

[55] S. Azizi, G. Rezazadeh, M.-R. Ghazavi, and S. E. Khadem, *Parametric excitation of a piezoelectrically actuated system near hopf bifurcation,* Applied Mathematical Modelling **36**, 1529 (2012).

[56] A. Champneys, *Dynamics of parametric excitation,* in *Mathematics of Complexity and Dynamical Systems,* edited by R. A. Meyers (Springer New York, New York, NY, 2011) pp. 183–204.

[57] B. E. DeMartini, J. F. Rhoads, K. L. Turner, S. W. Shaw, and J. Moehlis, *Linear and nonlinear tuning of parametrically excited mems oscillators,* Journal of Microelectromechanical Systems **16**, 310 (2007).

[58] A. Eichler, J. Chaste, J. Moser, and A. Bachtold, *Parametric amplification and self-oscillation in a nanotube mechanical resonator,* Nano Letters **11**, 2699 (2011).

[59] V. K. Lal, *Parametric excitation of circular micromachined polycrystalline silicon disks,* Applied Physics Letters **85**, 3923 (2004).

[60] R. Lifshitz and M. C. Cross, *Response of parametrically driven nonlinear coupled oscillators with application to micromechanical and nanomechanical resonator arrays,* Physical Review B **67**, 134302 (2003).

[61] M. Zalalutdinov, A. Zehnder, A. Olkhovets, S. Turner, L. Sekaric, B. Ilic, D. Czaplewski, J. M. Parpia, and H. G. Craighead, *Auto-parametric optical drive for micromechanical oscillators,* Appl. Phys. (2001).

[62] I. Mahboob and H. Yamaguchi, *Parametrically pumped ultrahigh q electromechanical resonator,* Applied Physics Letters **92**, 253109 (2008).

[63] J. P. Mathew, R. N. Patel, A. Borah, VijayR, and M. M. Deshmukh, *Dynamical strong coupling and parametric amplification of mechanical modes of graphene drums,* Nat Nano **11**, 747 (2016).

[64] K. Moran, C. Burgner, S. Shaw, and K. Turner, *A review of parametric resonance in microelectromechanical systems,* Nonlinear Theory and Its Applications, IEICE **4**, 198 (2013).

[65] G. Prakash, A. Raman, J. Rhoads, and R. G. Reifenberger, *Parametric noise squeezing and parametric resonance of microcantilevers in air and liquid environments,* Review of Scientific Instruments **83**, 065109 (2012).

[66] B. Rajashree and L. T. Kimberly, *Mechanical domain coupled mode parametric resonance and amplification in a torsional mode micro electro mechanical oscillator,* Journal of Micromechanics and Microengineering **13**, 701 (2003).

[67] J. P. Raskin, A. R. Brown, B. Khuri-Yakub, and G. M. Rebeiz, *A novel parametric-effect mems amplifier,* Journal of Microelectromechanical Systems **9**, 528 (2000).

[68] J. F. Rhoads, V. Kumar, S. W. Shaw, and K. L. Turner, *The non-linear dynamics of electromagnetically actuated microbeam resonators with purely parametric excitations,* International Journal of Non-Linear Mechanics **55**, 79 (2013).

[69] J. F. Rhoads and S. W. Shaw, *The impact of nonlinearity on degenerate parametric amplifiers,* Applied Physics Letters **96**, 234101 (2010).

[70] J. F. Rhoads, S. W. Shaw, K. L. Turner, and R. Baskaran, *Tunable microelectromechanical filters that exploit parametric resonance,* Journal of Vibration and Acoustics **127**, 423 (2005).

[71] J. F. Rhoads, S. W. Shaw, K. L. Turner, J. Moehlis, B. E. DeMartini, and W. Zhang, *Nonlinear response of parametrically-excited mems,* Proceedings of IDETC/CIE 2005 , 453 (2005).

[72] J. F. Rhoads, S. W. Shaw, K. L. Turner, J. Moehlis, B. E. DeMartini, and W. Zhang, *Generalized parametric resonance in electrostatically actuated microelectromechanical oscillators,* Journal of Sound and Vibration **296**, 797 (2006).

[73] D. Rugar and P. Gruetter, *Mechanical parametric amplification and thermomechanical noise squeezing,* Physical Review Letters **67**, 699 (1991).

[74] S. W. Shaw, K. L. Turner, J. F. Rhoads, and R. Baskaran, *Parametrically excited mems-based filters,* in *IUTAM Symposium on Chaotic Dynamics and Control of Systems and Processes in Mechanics: Proceedings of the IUTAM Symposium held in Rome, Italy, 8?13 June 2003,* edited by G. Rega and F. Vestroni (Springer Netherlands, Dordrecht, 2005) pp. 137–146.

[75] O. Shoshani and S. W. Shaw, *Generalized parametric resonance,* SIAM Journal on Applied Dynamical Systems **15**, 767 (2016).

[76] C. van der Avoort, R. van der Hout, and J. Hulshof, *Parametric resonance and hopf bifurcation analysis for a mems resonator,* Physica D: Nonlinear Phenomena **240**, 913 (2011).

[77] F. Verhulst, *Parametric and autoparametric resonance,* Acta Applicandae Mathematica **70**, 231 (2002).

[78] W. Zhang and K. L. Turner, *A mass sensor based on parametric resonance,* Proceedings of the Solid State Sensor, Actuator and Microsystem Workshop, Hilton Head Island, SC , 49 (2004).

[79] R. B. Wenhua Zhang and K. L. Turner, *Nonlinear dynamics analysis of a parametrically resonant mems sensor,* SEM Annual Conference & Exposition on Experimental and Applied Mechanics (2002).

[80] M. Zalalutdinov, A. Olkhovets, A. Zehnder, B. Ilic, D. Czaplewski, H. G. Craighead, and J. M. Parpia, *Optically pumped parametric amplification for micromechanical oscillators,* Applied Physics Letters **78**, 3142 (2001).

[81] M. Zalalutdinov, A. Zehnder, A. Olkhovets, S. Turner, L. Sekaric, B. Ilic, D. Czaplewski, J. M. Parpia, and H. G. Craighead, *Autoparametric optical drive for micromechanical oscillators,* Applied Physics Letters **79**, 695 (2001).

[82] L. D. Zavodney, A. H. Nayfeh, and N. E. Sanchez, *The response of a single-degree-of-freedom system with quadratic and cubic non-linearities to a principal parametric resonance,* Journal of Sound and Vibration **129**, 417 (1989).

[83] W. Zhang, R. Baskaran, and K. L. Turner, *Effect of cubic nonlinearity on auto-parametrically amplified resonant mems mass sensor,* Sensors and Actuators A: Physical **102**, 139 (2002).

[84] W. Zhang and K. L. Turner, *Application of parametric resonance amplification in a single-crystal silicon micro-oscillator based mass sensor,* Sensors and Actuators A: Physical **122**, 23 (2005).

[85] W. M. Zhang and G. Meng, *Nonlinear dynamic analysis of electrostatically actuated resonant mems sensors under parametric excitation,* IEEE Sensors Journal **7**, 370 (2007).

[86] J. Zhu, C. Q. Ru, and A. Mioduchowski, *High-order subharmonic parametric resonance of nonlinearly coupled micromechanical oscillators,* The European Physical Journal B **58**, 411 (2007).

[87] D. W. Jordan and P. Smith, *Nonlinear Ordinary Differential Equations, An introduction for Scientists and Engineers FOURTH EDITION* (Oxford university press, 2007).

[88] N. W. M. Lachlan, *Theory and Application of Mathieu Functions* (Dover, 1947).

[89] R. Grimshaw, *Nonlinear Ordinary Differential Equations* (CRC Press, 1991).

[90] V. Kumar, Y. Yang, J. W. Boley, G. T. C. Chiu, and J. F. Rhoads, *Modeling, analysis, and experimental validation of a bifurcation-based microsensor,* Journal of Microelectromechanical Systems **21**, 549 (2012).

[91] R. H. Rand, *Lecture notes on Nonlinear vibrations* (Dept. Theoretical & Applied Mechanics Cornell University, -).

[92] O. Brand, I. Dufour, S. M. Heinrich, and F. Josse, eds., *Resonant MEMS- Fundamentals, Implementation and Application* (Wiley, 2015 ed).

[93] B. Yurke, P. G. Kaminsky, R. E. Miller, E. A. Whittaker, A. D. Smith, A. H. Silver, and R. W. Simon, *Observation of 4.2-k equilibrium-noise squeezing via a josephson-parametric amplifier,* Phys. Rev. Lett. **60**, 764 (1988).

[94] V. Radeka and R. L. Chase, *A parametric radiation detector preamplifier,* IEEE Transactions on Nuclear Science **13**, 477 (1966).

[95] Y. Zhang, H. Wang, X. Li, J. Jing, C. Xie, and K. Peng, *Experimental generation of bright two-mode quadrature squeezed light from a narrow-band nondegenerate optical parametric amplifier,* Phys. Rev. A **62**, 023813 (2000).

[96] M. E. Marhic, N. Kagi, T.-K. Chiang, and L. G. Kazovsky, *Broadband fiber optical parametric amplifiers,* Opt. Lett. **21**, 573 (1996).

[97] MahboobI and YamaguchiH, *Bit storage and bit flip operations in an electromechanical oscillator,* Nat Nano **3**, 275 (2008).

[98] J. Suh, M. D. LaHaye, P. M. Echternach, K. C. Schwab, and M. L. Roukes, *Parametric amplification and back-action noise squeezing by a qubit-coupled nanoresonator,* Nano Letters **10**, 3990 (2010), pMID: 20843059, http://dx.doi.org/10.1021/nl101844r .

[99] R. Napoli, M.and Baskaran, K. Turner, , and B. Bamieh, *Understanding mechanical domain parametric resonance in microcantilevers.* in *Proceedings of the IEEE 16th Annual International Conference on Micro Electro Mechanical Systems, pp. 169?172* (2003).

[100] M.Napoli, C. B.Bamieh, and K.Turner, *A novel sensing scheme for the displacement of electrostatically actuated microcantilevers, Proceedings of the 2005 American Control Conference, pp 2475?2480,* (2005).

[101] M. F. Yu, G. J. Wagner, R. S. Ruoff, , and M. J. Dyer, *Realization of parametric resonances in a nanowire mechanical system with nanomanipulation inside a scanning electron microscope.* Phys. Rev. B, 66 (7), 073406 (2002).

[102] C. Liu and V. Tripathi, *Observational consequences of parametrically driven vibrations of carbon nanotubes,* Phys. Rev. B, 70 (15), 115414. (2004).

[103] M. Requa and K. Turner, *Electromechanically driven and sensed parametric resonance in silicon microcantilevers.* Appl. Phys. Lett., 88 (26), 263508. (2006).

[104] J. F. Rhoads, V. Kumar, S. W. Shaw, and K. L. Turner, *The non-linear dynamics of electromagnetically actuated microbeam resonators with purely parametric excitations,* International Journal of Non-Linear Mechanics **55**, 79 (2013).

[105] V. Kumar, Y. Yang, J. W. Boley, G. T. C. Chiu, and J. F. Rhoads, *Modeling, analysis, and experimental validation of a bifurcation-based microsensor,* Journal of Microelectromechanical Systems **21**, 549 (2012).

[106] L. A. Oropeza-Ramos and K. L. Turner, *Parametric resonance amplification in a memgyroscope,* in *IEEE Sensors,* (2005.) p. 4 pp.

[107] C. B. Burgner, W. S. Snyders, and K. L. Turner, *Control of mems on the edge of instability,* in *2011 16th International Solid-State Sensors, Actuators and Microsystems Conference* (2011) pp. 1990–1993.

[108] C. Guo and G. K. Fedder, *Bi-state control of parametric resonance,* Applied Physics Letters **103**, 183512 (2013).

[109] S.-B. Shim, M. Imboden, and P. Mohanty, *Synchronized oscillation in coupled nanomechanical oscillators,* Science **316**, 95 (2007).

[110] M. Moreno-Moreno, A. Raman, J. Gomez-Herrero, and R. Reifenberger, *Parametric resonance based scanning probe microscopy,* Applied Physics Letters **88**, 193108 (2006).

[111] T. Ouisse, M. Stark, F. Rodrigues-Martins, B. Bercu, S. Huant, and J. Chevrier, *Theory of electric force microscopy in the parametric amplification regime,* Physical Review B **71**, 205404 (2005).

[112] R. Grimshaw, *Nonlinear Ordinary Differential Equations* (CRC Press, 1991).

[113] A. R. R. S. Itamar Katz, Ron Lifshitz, *Classical to quantum transition of a driven nonlinear nanomechanical resonator,* Physics letters (20 Jul 2008)).

[114] M. V. Requa and K. L. Turner, *Precise frequency estimation in a microelectromechanical parametric resonator,* Applied Physics Letters **90**, 173508 (2007).

[115] M. V. Requa and K. L. Turner, *Electromechanically driven and sensed parametric resonance in silicon microcantilevers,* Applied Physics Letters **88**, 263508 (2006).

[116] Y. Linzon, B. Ilic, S. Lulinsky, and S. Krylov, *Efficient parametric excitation of silicon-on-insulator microcantilever beams by fringing electrostatic fields,* Journal of Applied Physics **113**, 163508 (2013).

[117] C. Guo, E. Tatar, and G. K. Fedder, *Large-displacement parametric resonance using a shaped comb drive,* in *2013 IEEE 26th International Conference on Micro Electro Mechanical Systems (MEMS)*, pp. 173–176.

[118] B. Ilic, H. G. Craighead, S. Krylov, W. Senaratne, C. Ober, and P. Neuzil, *Attogram detection using nanoelectromechanical oscillators,* Journal of Applied Physics **95**, 3694 (2004).

[119] T. K. Eduard Ventsel, *Thin plates and shells :Theory, analysis and applications* (CRC Press, 2001).

[120] S. S. Rao, *Vibration of Continuous Systems* (wiley, 2007).

[121] J. Hedberg, *Wavy graphene - a 3d model of graphene showing the undulations of the crystal,,* (2014).

A

LINEAR MECHANICS OF MEMBRANE

In this section, the solution to the linear differential equation governing the dynamics of the membrane are discussed. The eigenfrequency and the corresponding mode shapes are derived. Finally, the initial tension present in the membrane is extracted from the frequency equation and is validated against a COMSOL model.

A.1. EIGENFREQUENCIES OF CLAMPED CIRCULAR MEMBRANE

This section discusses the solution of a linear differential equation governing the motion of clamped circular membrane. It is important to look at the linear solution, the mode shapes and the corresponding eigenfrequencies as they could be used to make a preliminary approximation as to what the admissible displacement functions should be for the same membrane governed by nonlinear equations of motion. The following derivation closely follows references [39, 120].

The equation that governs the vibration of a membrane is a wave equation and in Cartesian coordinates the forced vibration of a membrane is given by,

$$n_0\left(\frac{\partial^2 w}{\partial x^2} + \frac{\partial^2 w}{\partial y^2}\right) + P_z = \rho h \frac{\partial^2 w}{\partial t^2} \tag{A.1}$$

where $w(x,y)$ represents the deflection in the out of plane direction(m), x and y are the coordinates , ρ is the density of the material ($\text{kg}\,\text{m}^{-3}$), h is the thickness of the membrane(m), n_0 is the initial tension per unit length ($\text{N}\,\text{m}^{-1}$) and P_z is the external load per unit area ($\text{N}\,\text{m}^{-2}$).

For free vibrations of a circular membrane the above equation is expressed in cylindrical coordinates by using the transformation $x = r\cos(\theta)$ and $y = r\sin(\theta)$. This gives the governing differential equation of the form,

$$\frac{\partial^2 w(r,\theta,t)}{\partial r^2} + \frac{1}{r}\frac{\partial w(r,\theta,t)}{\partial r} + \frac{1}{r^2}\frac{\partial^2 w(r,\theta,t)}{\partial \theta^2} = \frac{\rho h}{n_0}\frac{\partial^2 w}{\partial t^2} \tag{A.2}$$

The solution for the displacement $w(r,\theta,t)$ is obtained by method of separation of variables

and expressed as,

$$w(r, \theta, t) = R(r)\Theta(\theta)T(t) \tag{A.3}$$

Where, R, Θ and T are functions of r, θ and t only.

Assuming harmonic vibration with frequency ω we have,

$$w(r, \theta, t) = R(r)\Theta(\theta)sin(\omega t) \tag{A.4}$$

Substituting equation A.3 into equation A.2 we have,

$$\frac{R''(r)}{R(r)} + \frac{1}{r^2}\frac{\Theta''(\theta)}{\Theta(\theta)} + \frac{1}{r}\frac{R'(r)}{R(r)} + \omega^2\frac{\rho h}{n_0} = 0 \tag{A.5}$$

By Introducing λ^2 as the separation constant,

$$\lambda^2 = \omega^2\frac{\rho h}{n_0} \tag{A.6}$$

We reduce equation A.5 into two separate differential equations given by,

$$\frac{d^2\Theta(\theta)}{d\theta^2} + \alpha^2\Theta(\theta) = 0 \tag{A.7}$$

and

$$\frac{d^2R(r)}{dr^2} + \frac{1}{r}\frac{dR(r)}{dr} + \left(\lambda^2 - \frac{\alpha^2}{r^2}\right)R(r) = 0 \tag{A.8}$$

Since the constant α^2 must yield the displacement 'w' as a periodic function of θ with a period 2π i.e., [w(r, θ, t) = w(r, $\theta + 2\pi$, t)]. α must be an integer. Hence,

$$\alpha = m, \qquad m = 0, 1, 2...$$

The solutions of equations A.8 and A.7 are given by,

$$\Theta(\theta) = C_{1m}\cos m\theta + C_{2m}\sin m\theta \tag{A.9}$$
$$R(r) = B_1 J_m(\lambda r) + B_2 Y_m(\lambda r) \tag{A.10}$$

In order for the displacement (w) to be finite everywhere the constant B_2 is taken to be zero, hence the radial solution becomes

$$R(r) = B_1 J_m(\lambda r) \tag{A.11}$$

From the above equations one can deduce the complete solution as,

$$w(r, \theta, t) = W_m(r, \theta)\sin(\omega t) \tag{A.12}$$
$$W_m(r, \theta) = J_m(\lambda r)(C_{1m}\cos m\theta + C_{2m}\sin m\theta) \tag{A.13}$$

For a clamped membrane with radius *'a'*, the displacement *'w'* has to disappear at the boundary r = a, this can be translated into a boundary condition as,

$$W_m(r,\theta) = 0, \qquad m = 0,1,2... \tag{A.14}$$

Using equation A.13 we have,

$$W_m(r,\theta) = J_m(\lambda r)(C_{1m}\cos m\theta + C_{2m}\sin m\theta) = 0 \tag{A.15}$$

Which gives the following condition

$$J_m(\lambda a) = 0 \tag{A.16}$$

The equation A.16 is called the frequency equation. The equation has infinte number of discrete solutions, $\gamma_m n = \lambda a$ for each value of m.

For m=0, $J_0(\gamma) = 0$:

$$\gamma_{0n} = \lambda a = 2.405,\ 5.520,\ 8.654,.....$$

For m=1, $J_1(\gamma) = 0$:

$$\gamma_{1n} = \lambda a = 3.832, 7.016, 10.173,.....$$

For m=2, $J_2(\gamma) = 0$:

$$\gamma_{2n} = \lambda a = 5.135, 8.417, 11.620,.....$$

The angular frequency is then given by,

$$\omega_{mn} = \frac{\gamma_{mn}}{a}\sqrt{\frac{n_0}{\rho h}} \quad \mathrm{rad\,s^{-1}} \tag{A.17}$$

The eigenfrequency is given by,

$$f_{mn} = \frac{\gamma_{mn}}{2\pi a}\sqrt{\frac{n_0}{\rho h}} \quad \mathrm{s^{-1}} \tag{A.18}$$

The complete solution for a clamped circular membrane is given by,

$$w(r,\theta, t) = W_m(r,\theta)\sin(\omega t) \tag{A.19}$$

$$W_m(r,\theta) = J_m\left(\gamma_{mn}\left(\frac{r}{a}\right)\right)(C_{1m}\cos m\theta + C_{2m}\sin m\theta) \tag{A.20}$$

From equation A.18 it can be seen that decreasing the mass or radius and increasing the tension of the membrane increases the natural frequency and from equation A.20 it can be seen that except for m=0 all other frequencies have degenerate mode shapes. In the mode shape of the membrane represented by $W_m(r,\theta)$, the value *'m'* denotes the number of nodal diameters and the value *n* denotes the number of nodal circles. First few mode shapes are shown in Figure A.1.

A.1.1. EXTRACTING THE INITIAL TENSION FROM FREQUENCY EQUATION

The initial tension applied on the graphene membrane is difficult to measure and requires further set of experiments to accurately measure the value. For modeling and numerical simulations the value n_0 is extracted from the frequency equation A.16.

For graphene nano drum resonators we have, radius (a)= 2.5 μm
density (ρ)= 2330 kg m^{-3}
Thickness (h) = 0.335 nm
First natural frequency(f_{01}) = 13.6 MHz
First angular frequency (ω_{01})= $2\pi f_{01}$

Using equation A.17 we obtain the value for initial tension (n_0) as 0.006 159 N m^{-1}.

The above value for initial tension is verified by using a COMSOL model, The value of the initial tension is plugged into the parameters and the corresponding natural frequency of the membrane is verified to be equal to 13.6 MHz. The Figure A.1 shows the mode shapes of a circular membrane clamped along the outer edge.

(a) Mode shape ω_{01}

(b) Mode shape ω_{11}

(c) Mode shape ω_{21}

(d) Mode shape ω_{02}
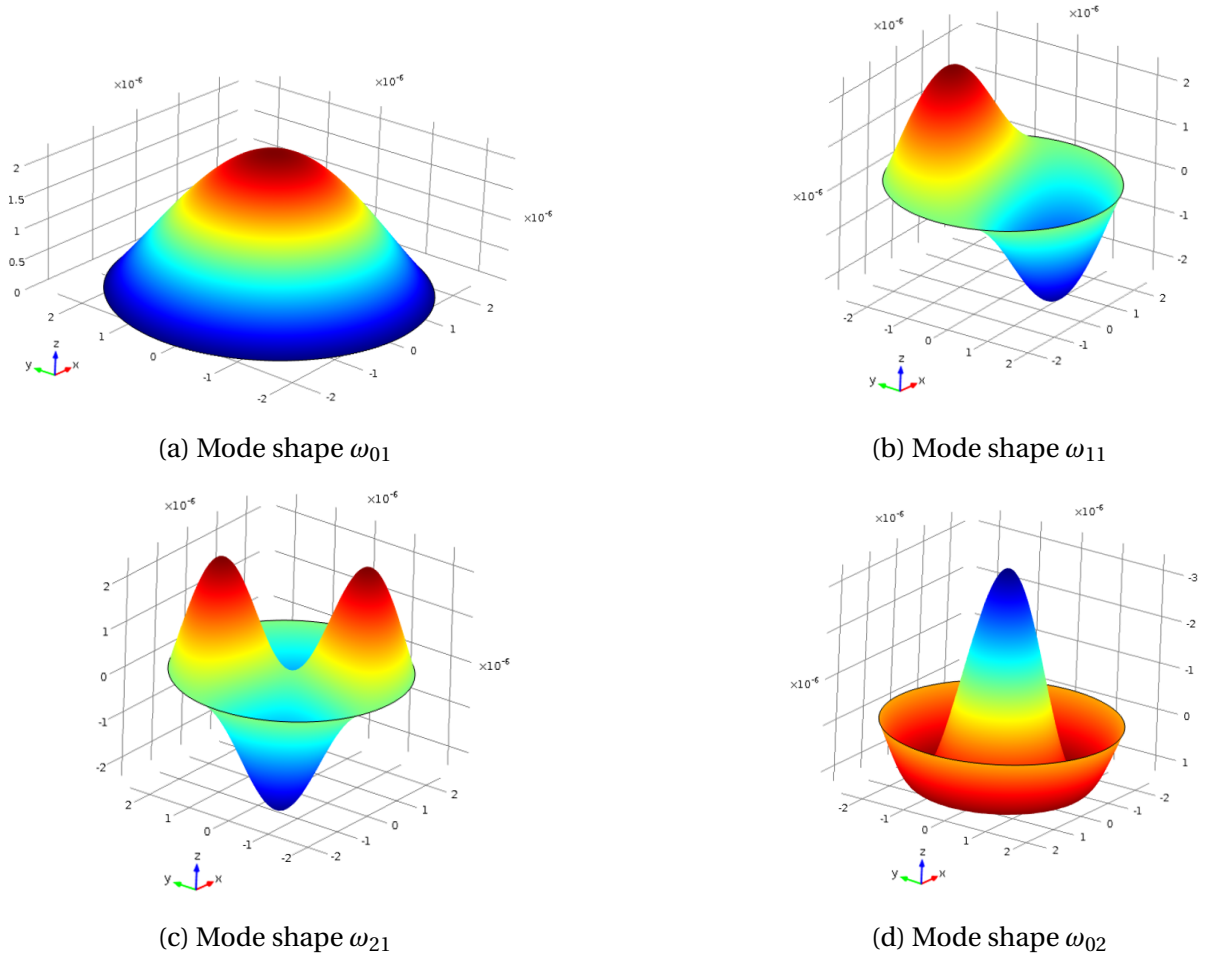
Figure A.1: First 4 eigen modes of a circular membrane obtained from COMSOL simulation.

B

DYNAMICS OF DUFFING OSCILLATOR AND RESPONSE OF SYSTEM DUE TO POSITIVE GEOMETRIC IMPERFECTION

In this section, the dynamics of Duffing oscillator is analyzed using perturbation techniques. The Frequency response equation is derived and the influence of various parameters on the system dynamics is discussed. Then, the multivaluedness of the frequency response curve is used to explain the jump phenomenon. Finally, the response of system due to positive geometric imperfection as a source of direct excitation is studied.

B.1. PRIMARY DUFFING RESONANCE

The primary resonance occurs when the external excitation coincides with the resonant frequency ($\omega = \omega_0$). To analyze this case, the order of damping, the nonlinearities and the external excitation must appear in the same time scale in the perturbation scheme. For this reason the solution is scaled as ϵx, the damping as $\epsilon^2 \zeta$, and excitation amplitude as $\epsilon^3 f$. Where, ϵ is a perturbation parameter.

The equation of motion becomes,

$$\ddot{x} + \epsilon^2 2\zeta \dot{x} + x + \epsilon \eta x^2 + \epsilon^2 \gamma x^3 = \epsilon^2 f \cos \Omega \tau \tag{B.1}$$

The approximate solution is assumed to be of the form,

$$x(t,\epsilon) = x_0(t, \epsilon t, \epsilon^2 t) + \epsilon x_1(t, \epsilon t, \epsilon^2 t) + \epsilon^2 x_2(t, \epsilon t, \epsilon^2 t) + \dots$$

The excitation frequency is such that,

$$\Omega = 1 + \epsilon^2 \sigma$$

Where, σ is the external detuning

By using the method of multiple scales the solution of equation B.1 to second order approximation is given by,

$$x = a\cos(\omega t - \phi) + \frac{1}{2}\epsilon\alpha_2\omega_0^{-2}a^2\left[-1 + \frac{1}{3}\cos(2\omega t - 2\phi)\right] + \mathcal{O}(\epsilon^2) \tag{B.2}$$

The nonlinear term in the solution $\frac{1}{2}\epsilon\alpha_2\omega_0^{-2}a^2$ is due to the asymmetric nonlinearity (x^2) which causes the system to drift or steady stream from the equilibrium position.

The amplitude (a) and phase (ϕ) are governed by,

$$a' = -\zeta a + \frac{f}{2}\sin(\phi) \tag{B.3a}$$

$$a\phi' = \sigma a - \frac{9\gamma - 10\eta^2}{24}a^3 + \frac{f}{2}\cos(\phi) \tag{B.3b}$$

The prime indicates derivative with respect to slow time scale ϵt. The steady state solutions are obtained by setting the equations B.3a and B.3b equal to zero and solving for the amplitude and external detuning relationship. The obtained equation represents the frequency response equation. Which is given by,

$$\left[\zeta^2 + \left(\sigma - \frac{9\gamma - 10\eta^2}{24}a^2\right)\right]a^2 = \frac{f^2}{4} \tag{B.4}$$

The phase equation is given by,

$$\tan\phi = \frac{\zeta}{\sigma - \frac{9\gamma - 10\eta^2}{24}a^2} \tag{B.5}$$

From the above equation we see that for the case $\phi = 0$, the quadratic nonlinearity has a softening effect on the system irrespective of the sign of η. Hence unless $\gamma > \frac{10}{9}\eta^2$ the system will have a softening behavior. It is also interesting to see that both nonlinearities cancel the effect of each other if $\gamma > \frac{10}{9}\eta^2$. But from Figure 1.3 it is seen that the hardening behavior dominates in the Duffing response indicating that indeed $\gamma > \frac{10}{9}\eta^2$ for optically actuated graphene nanodrum resonators. This is an important result as it indicates that in order to fit a Duffing response to an experimentally obtained curve we can ignore the effect of quadratic nonlinear stiffness and build a model with a dominant cubic stiffness nonlinearity.

It is seen that the effect of nonlinearity is to bend the amplitude curve and distort the phase curve. The profound difference between the nonlinear and linear oscillator is that in the nonlinear case the response is multivalued meaning there can be as much as three different response amplitudes for a driving frequency. This is consequence of the fact that the equation B.4 is cubic in a^2. This multivaluedness leads to well known *jump phenomenon.* Which is briefly discussed in the next section.

Jump Phenomena

The multivaluedness of the response curves due to nonlinearities has a significance from physical point of view because it leads to jump phenomena. In order to understand this,
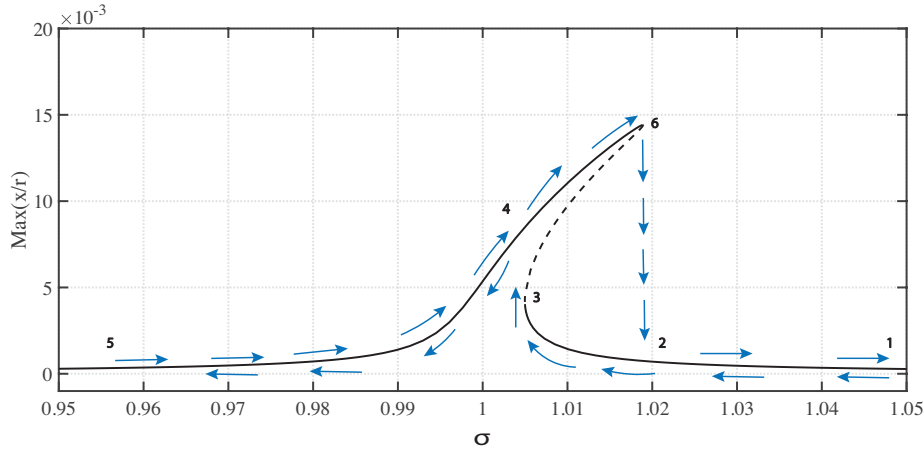
Figure B.1: Duffing primary response showing jump phenomenon and hysteresis

consider an experiment is conducted in which the amplitude of the excitation is held fixed and the frequency of excitation is slowly varied forward and reverse the natural frequency of the resonator and the amplitude of the response is observed. The experiment is started at a frequency corresponding to 1 in Figure B.1. As the frequency is reduced σ decreases and the amplitude a increase slowly through point 2 until point 3 is reached. As σ is decreased further, a jump from point 3 to point 4 takes place with an accompanying increase in amplitude a and a large shift in the phase ϕ and then the amplitude a decreases with decreasing σ. If the experiment is started at point 5 and σ is increased then the amplitude a increases through point 4 till point 6 is reached. As σ increases further, the amplitude a jumps from point 6 to point 2 with a large change in ϕ and further decreases with increasing σ. The transitions from the upper branch to the lower branch and vice versa occur at different values of the driving frequency, and as a consequence, depending on how the specific driving frequency is reached in the range of $\sigma_1 < \omega_0 < \sigma_2$, the response is different since it depends on the initial conditions; this phenomenon is called *hysteresis*.

B.1.1. SECONDARY OR SUPERHARMONIC RESONANCES

As seen in Figure 1.3, in addition to the standard Duffing response we see additional super-harmonics at $\omega = \frac{\omega_0}{2}$ and $\omega = \frac{\omega_0}{3}$ corresponding to the quadratic and cubic nonlinearities. The solution to such non integer excitation frequency has been studied in detail in many literature [46, 49]. Hence, in this section, we will briefly discuss the solutions that are obtained by using method of multiple scales. In order to study the dynamics of such superharmonic resonances, the perturbation parameter (ϵ) needs to be adjusted such that the direct excitation occurs in the same time scheme as the free oscillation part of the solution and the damping appears in the same perturbation equation as the quadratic and cubic nonlinearities.

For quadratic nonlinearity

$$\Omega = \frac{1}{2} + \epsilon\sigma$$

The equation of motion is given by,

$$\ddot{x} + \epsilon 2\zeta\dot{x} + x + \epsilon\eta x^2 + \epsilon^2\gamma x^3 = f\cos\Omega\tau \tag{B.6}$$

The solution to the first approximation is obtained by using method of mutliple scales and by grouping all the secular terms in the order $\mathscr{O}(\epsilon)$ to zero,

$$x = \frac{\frac{F}{m}}{\omega_0^2 - \Omega^2} \cos(\omega t) - a\sin(2\omega t - \phi) + \mathscr{O}(\epsilon) \tag{B.7}$$

Where a is given by,

$$a = \frac{\eta F^2}{4m^2\omega_0(\omega_0^2 - \Omega^2)^2(\zeta^2 + \sigma^2)^{1/2}} \tag{B.8}$$

Similarly, to obtain the superharmonic resonance corresponding to cubic nonlinearity the damping is now made to appear in the same perturbation equation as the cubic nonlinearity and the direct excitation appears in the same equation as the free oscillation part.

For cubic nonlinearity

$$\Omega = \frac{1}{3} + \epsilon\sigma$$

The equation of motion is given by,

$$\ddot{x} + \epsilon 2\zeta\dot{x} + x + \eta x^2 + \epsilon\gamma x^3 = f\cos\Omega\tau \tag{B.9}$$

The solution to the first approximation is obtained by using method of mutliple scales and by grouping all the secular terms in the order $\mathscr{O}(\epsilon)$ to zero,

$$x = \frac{\frac{F}{m}}{\omega_0^2 - \Omega^2} \cos(\omega t) + a\cos(3\omega t - \phi) + \mathscr{O}(\epsilon) \tag{B.10}$$

Where a is given by,

$$\left[\zeta^2 + \left(\sigma - 3\frac{\gamma\Lambda^2}{\omega_0} - \frac{3\gamma}{8\omega_0}a^2\right)^2\right]a^2 = \frac{\gamma^2\Lambda^6}{\omega_0^2}$$

$$\Lambda = \frac{\frac{F}{m}}{\omega_0^2 - \Omega^2}$$

From the above equations, we see that when $\omega = \frac{\omega_0}{2}$ and $\omega = \frac{\omega_0}{3}$ the free oscillation term does not decay to zero in spite of presence of damping and is in contrast with the linear case. Moreover, the nonlinearities adjusts the frequency of free oscillation term to exactly twice and thrice the frequency of excitation so that the response is periodic. Since the frequency of the generated free oscillation term is higher multiple of excitation frequency they are termed as superharmonic or secondary resonances. This explains the reason behind the appearance of such secondary resonances seen in Figure 1.3.

B.1.2. POSITIVE GEOMETRIC IMPERFECTION

The procedure to derive the mathematical model is similar to that shown in section 4.2.1 with the difference that the transverse displacement function now includes a w_0, the deviation of the membrane in the positive z-direction from flat configuration.
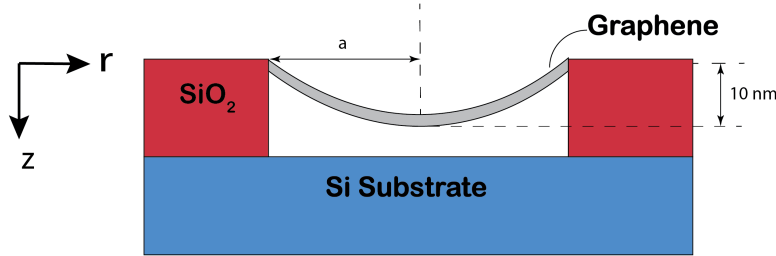
Figure B.2: Positive initial imperfection modeled as first vibrational mode shape

For an axisymmetric model the radial displacement field is given by equation 3.8 and the transverse displacement equation from 2.7 can be rewritten as,

$$u_z(r,\theta,z,t) = w(r,t) + w_0(r)$$

Where w_0 represents the initial geometric imperfection. The positive sign is taken as per the conventions indicated in 4.2 and from here on referred as positive initial geometric impefection. For simplifying the model the spatial distribution of the geometric imperfection is assumed to resemble the first vibration mode shape of the circular membrane.

$$u_z = x(t) J_0\left(\alpha_0 \frac{r}{a}\right) + \delta J_0\left(\alpha_0 \frac{r}{a}\right) \tag{B.11}$$

Where, $\delta = 10\,\text{nm}$ and $\alpha_0 = 2.40483$.

The strains and stresses for the axisymmetric model can be obtained from equation 2.16 and equation 2.10 respectively. The rest of the procedure to derive the equations of motion is the same as shown in section 4.2.1. Figure B.3 shows the frequency response curve obtained by numerically simulating the SDOF model with positive geometric imperfection. As seen from the figure the qualitative dynamics of the system remains the same as seen in the case of negative geometric imperfection.
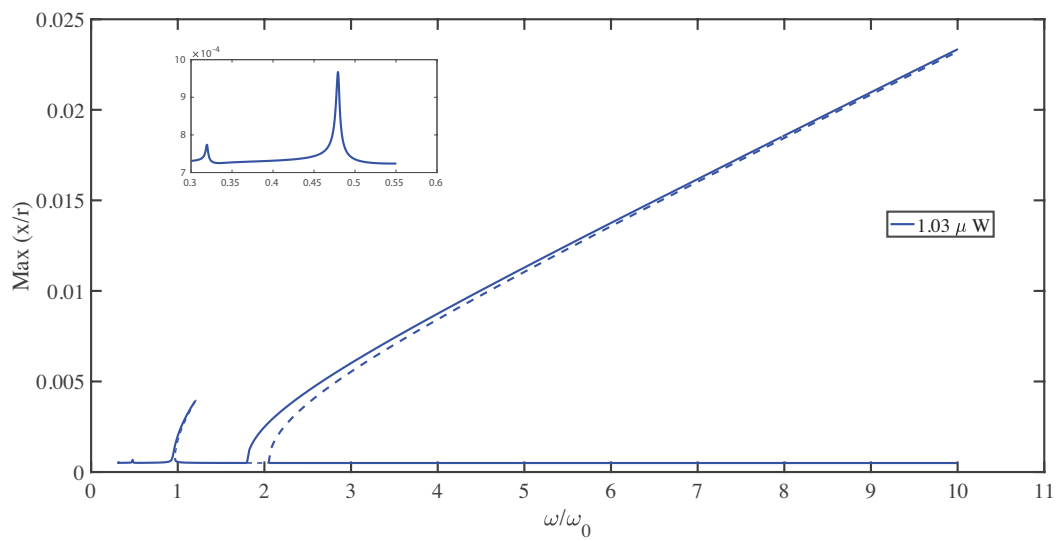
Figure B.3: Frequency response of SDOF model with positive initial imperfection showing direct, parametric and superharmonic responses

C

EFFECT OF HIGHER ORDER NONLINEARITIES

In order to understand the effect of other higher order nonlinearities and different damping mechanisms playing a role in the system dynamics, simulations are carried out with these different terms by adding them explicitly into the main equation of motion given by 5.13.

1. Damping of the form $\dot{x}^2$: General heat propagation in a membrane is given by 2.5,

$$k\nabla^2\Delta T + Q = \rho c_p \frac{\partial \Delta T}{\partial t} + \underbrace{\frac{E\alpha\Delta T}{1-2\nu}\frac{\partial e}{\partial t}}_{\text{Thermoelastic coupling term}}$$

Where, e is the dilatation.

The thermoelastic coupling term is ignored in the model simulated in previous section due to the small strength of such a coupling in MEMS/NEMS devices. When the thermoelastic coupling term is included in the Lagrange formualtion it introduces a thermoelastic damping term proportional to $\dot{x}^2$. By including such a term in the model explicitly, we obtain the equation of motion give by equation C.1.

$$\ddot{x} + \mu\dot{x} + \eta x^2\dot{x} + \psi\dot{x}^2 + x + \delta\cos(\Omega\tau)x + \gamma x^3 = f\cos(\Omega\tau) \tag{C.1}$$

Simulating the above equation of motion we obtain the frequency response curve shown in Figure C.1. In the figure, the coefficient of the thermoelastic damping term is increased to see the effect on system dynamics. As seen from the figure the thermoelastic damping term is a symmetry breaking nonlinearity that causes the curve to bend away from the experimental response. The thermoelastic damping does little to bridge the gap between the bifurcation points marked with a red dashed rectangle. By comparing the experimental and theoretical curves it could be concluded that the strength of thermoelastic coupling term is too weak to affect the dynamics of the system. This is in agreement with the initial modeling assumptions.

81
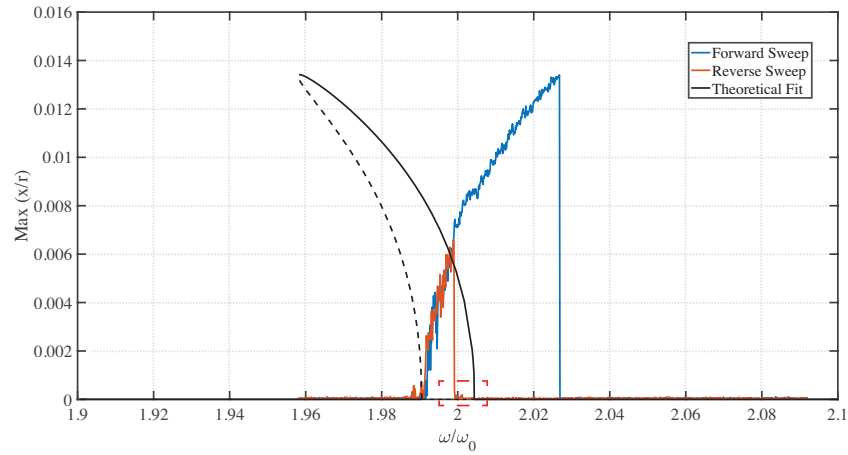
Figure C.1: Frequency response dominated by term $\dot{x}^2$.

2. Damping of the form $\dot{x}^3$: This type of damping arises from the macroscopic damping mechanisms such as friction. It can be derived by considering the nonlinear mechanical interaction of a Duffing type oscillator with a thermal bath made out of harmonic degrees of freedom [18, 32]. By incorporating this nonlinear damping term in the equation of motion we obtain equation C.2.

$$\ddot{x} + \mu\dot{x} + \eta x^2\dot{x} + \kappa\dot{x}^3 + x + \delta\cos(\Omega\tau)x + \gamma x^3 = f\cos(\Omega\tau) \tag{C.2}$$

Simulating the above equation of motion, we obtain the frequency response curve shown in Figure C.2. As seen from the figure, the nonlinear damping term ($\kappa\dot{x}^3$) can be used to limit the response of the parametric response similar to the material damping term ($\eta\dot{x}x^2$) but the term has little effect in decreasing the gap between the bifurcation points marked with a red dashed rectangle. Furthermore, it is seen that $\kappa\dot{x}^3$ damping term need to have large coefficient compared to linear damping ($\mu\dot{x}$) and material damping ($\nu x^2\dot{x}$). This indicates that, higher the damping terms the less effective they are in limiting the parametric response when compared to lower order damping terms.
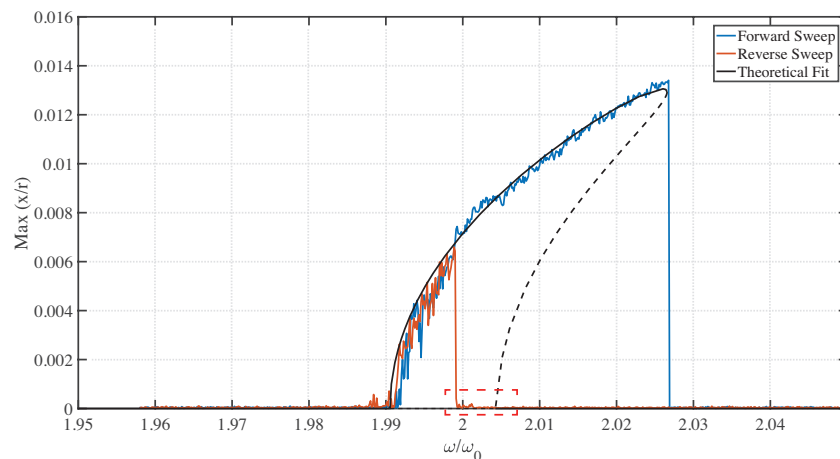
Figure C.2: Frequency response by including term $\dot{x}^3$ in equation of motion.

The following higher order damping terms are included in the model purely from a mathematical point of view to understand the effect on the dynamics of the system.

Currently it is not known what is the origin or physical mechanism that could explain their appearance in equation of motion. But nevertheless, they could be easily obtained by modeling the power absorbed as a function of spatial distribution and also by considering the interaction of the mechanical oscillator with thermal bath.

3. Damping of the form $\dot{x}^2 x$: The term $\dot{x}^2 x$ has the same effect as the material damping term $\dot{x}x^2$. It limits the unbound parametric response and also renormalizes to the cubic stiffness nonlinearity. By incorporating this nonlinear damping term in the equation of motion we obtain equation C.3.

$$\ddot{x} + \mu\dot{x} + \eta x^2 \dot{x} + \xi \dot{x}^2 x + x + \delta \cos(\Omega\tau)x + \gamma x^3 = f\cos(\Omega\tau) \tag{C.3}$$

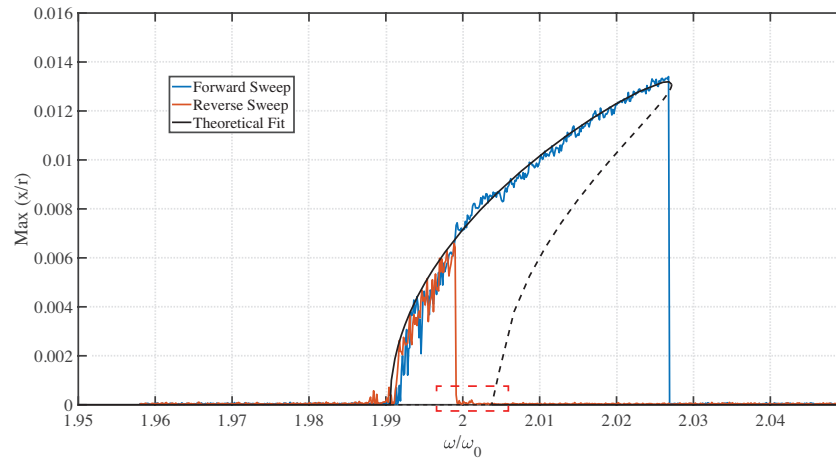Simulating the above equation of motion we obtain the frequency response curve shown in Figure C.2. The damping term $\dot{x}^2 x$ does not decrease the gap between the predicted and experimental bifurcation points.
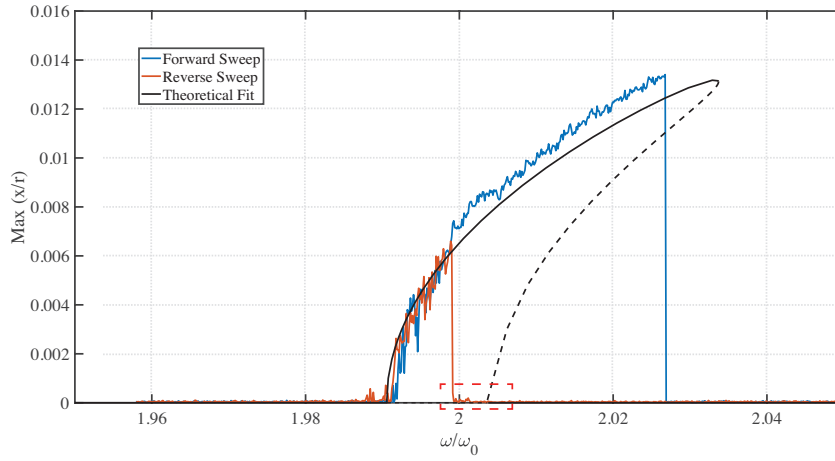
Figure C.3: Frequency response by including term $\dot{x}^2 x$ in equation of motion.

4. Damping of the form $\dot{x}x$: The damping proportional to $\dot{x}x$ can be modeled by considering the interaction between a Duffing oscillator and a thermal bath made out of harmonic degrees of freedom. By incorporating this nonlinear damping term in the equation of motion we obtain equation C.4.

$$\ddot{x} + \mu\dot{x} + \eta x^2 \dot{x} + \xi \dot{x}^2 x + x + \delta \cos(\Omega\tau)x + \gamma x^3 = f\cos(\Omega\tau) \tag{C.4}$$

Simulating the above equation of motion, we obtain the frequency response curve shown in Figure C.4. This damping term behaves as a symmetry breaking nonlinearity and causes the theoretical response curve to bend away from the experimental response. The damping does little to affect the bifurcation points of the response.
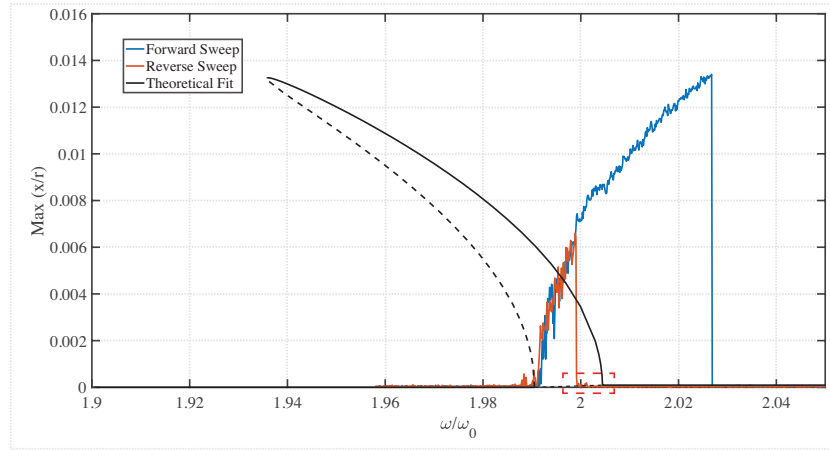
Figure C.4: Frequency response dominated by term $\dot{x}x$.

5. Damping of the form $\dot{x}x^4$: This damping is introduced from a mathematical perspective by assuming the material damping to be a series function proportional to even powers of oscillation amplitude, it can be written in the form $\nu\dot{x}x^2 + \Lambda\dot{x}x^4 + \ldots$.

    In order to balance the equation of motion an additional quintic stiffness term is added, it is given by Πx^5. The equation of motion formed is given by C.5,

    $$\ddot{x} + \mu\dot{x} + \eta x^2\dot{x} + \Lambda\dot{x}x^4 + x + \delta\cos(\Omega\tau)x + \gamma x^3 + \Pi x^5 = f\cos(\Omega\tau) \qquad \text{(C.5)}$$

Figure C.5: Frequency response by including term $\dot{x}x^4$ and x^5 in equation of motion.

Simulating the above equation of motion, we obtain the frequency response curve shown in Figure C.4. The terms added renormalizes the stiffness of the system but dont change the gap between the bifurcation points. Furthermore the term $\Lambda\dot{x}x^4$ also has limiting effect on the parametric response. But as seen in the previous case with the damping term proportional to the $\dot{x}^3$, the coefficient of Λ is almost three orders different from the term η. Which further bolsters the conclusion that higher nonlinear damping terms have relatively less effect on limiting the response of parametrically excited systems.

From the above simulations, it can be concluded that adding these higher order damping terms does not alter the response curves that are described in the previous chapters in a fundamental way. They merely conspire to renormalize the effective values of coefficients used in the original equation of motion. Thus, without any particular model and physical reason at hand, it is difficult to discern the existence of such terms in the equation.

DYNAMICS OF DUFFING-MATHIEU MODEL WITH NONLINEAR DAMPING

As discussed in chapter 3 section 3.4, the linear damping has limited effect on the amplitude of parametric response which causes the system response to grow exponentially. But in reality, this is not physically possible and as seen in experiments the amplitude of parametric response reaches a limit point and decreases rapidly with increase in frequency. In this chapter, we study the effects of nonlinear damping on both direct and parametric resonance and build a theoretical model to simulate the experimental behavior. The derivation closely follows the works of reference [31, 60].

D.1. DYNAMICS OF DIRECTLY DRIVEN DUFFING OSCILLATOR WITH NONLINEAR DAMPING

In this section, we consider a single degree of freedom Duffing oscillator with nonlinear damping that is driven by an external periodic force. The symmetry breaking terms like (x^2) are ignored and briefly discussed at the end of the chapter. A nonlinear damping term ($x^2\dot{x}$) is introduced externally into the equation of motion to represent the dissipation caused by material damping. The equation of motion is given by,

$$m\ddot{\tilde{x}} + c_1\dot{\tilde{x}} + k\tilde{x} + k_2\tilde{x}^2 + c_2\tilde{x}^2\dot{\tilde{x}} + k_3\tilde{x}^3 = F\cos\omega t \qquad \text{(D.1)}$$

where, m is the mass of the resonator, k_1 is the linear stiffness, k_3 is the cubic stiffness due to geometric nonlinearity, c_1 is the linear damping, c_2 is the nonlinear damping which increases with the amplitude of the oscillation and is obtained from the material, F is the amplitude of external excitation. Since we are interested in the effects on the nonlinear damping on the system, the unnecessary physical parameters are rescaled leaving only those that are significant. This is done by scaling the time with respect to the period of the resonant mode (t=$\omega_0\tau$), the amplitude of the oscillator is rescaled as (x = $\tilde{x}\sqrt{\frac{k_3}{m\omega_0^2}}$) and finally the entire equation is divided by the coefficient of the mass ($\omega_0^3\sqrt{\frac{m^3}{k_3}}$). This yields the following scaled equation of motion.

$$\ddot{x} + Q^{-1}\dot{x} + x + x^2 + \eta x^2\dot{x} + x^3 = f\cos\Omega\tau \qquad \text{(D.2)}$$

Where the overhead dots denotes the differentiation with respect to the dimensionless time τ, the dimensionless parameters are related to the physical parameters by table D.1

$Definition$	Non-dimensional parameter
$(\dot{\bullet}) = \frac{d(\bullet)}{d\tau}$	Scaled time derivative
$\Omega = \frac{\omega}{\omega_0}$	Non-dimensional excitation frequency
$\frac{1}{Q} = \frac{c_1}{m\omega_0}$	Quality factor
$\eta = \frac{c_2\omega_0}{k_3}$	Scaled Nonlinear damping coefficient
$f = \frac{F}{\omega_0^3}\sqrt{\frac{k_3}{m^3}}$	Scaled direct excitation amplitude

Table D.1: Non-dimensional parameter definitions

D.1.1. Dynamics Analysis of Equation of Motion using Averaging Methods

A perturbation technique is used to obtain the solution for the equation D.2. The solution is obtained in the limit of weak oscillations where the expansion of the force is truncated after the third power of x. This is done by requiring that the cubic force x^3 be a factor of ϵ smaller than the linear force or equivalently by ensuring the deviation from equilibrium x to be on the order of $\sqrt{\epsilon}$. Where ϵ is a perturbation parameter. Furthermore, the system is assumed to have weak linear damping which is of the order of the perturbation parameter $Q^{-1} = \epsilon << 1$. This reduces the equation of motion to,

$$\ddot{x} + \epsilon\dot{x} + x + x^2 + \eta x^2\dot{x} + x^3 = \epsilon^{3/2}f\cos(1 + \epsilon\sigma\tau) \tag{D.3}$$

Where, the non-dimensional driving frequency is taken to be of the form $\Omega = 1 + \epsilon\sigma$ to simulate behavior near resonance. σ represents *external detuning*.

Assuming the solution to equation D.3 of the form,

$$x(\tau) = \frac{\sqrt{\epsilon}}{2}(A(T)e^{i\tau} + c.c.) + \epsilon^{3/2}x_1(\tau) + ... \tag{D.4}$$

Where c.c. represents complex conjugate and the time scale T is given by $T = \epsilon\ \tau$. A(T) represents the slowly varying amplitude used to ensure that the higher order corrective terms don't diverge at singularities. Substituting the equation D.4 in to equation D.3 and grouping the terms of $\epsilon^{3/2}$ we have,

$$\ddot{x}_1 + x_1 = \left(-iA\prime - i\frac{1}{2}A - \frac{3+i\eta}{8}|A|^2A + \frac{f}{2}e^{i\sigma T}\right)e^{i\tau} - \frac{1+i\eta}{8}A^3e^{3i\tau} + c.c. \tag{D.5}$$

In the above equation the terms corresponding to $e^{i\tau}$ act like forces driving the system into resonance. These are called *secular terms* and by requiring that these terms equal to zero. A

solvability condition is imposed on the system which causes the solution to converge. The slowly varying amplitude is obtained from solvability condition as follows,

$$-iA' - i\frac{1}{2}A - \frac{3+i\eta}{8}|A|^2 A + \frac{f}{2}e^{i\sigma T} = 0 \tag{D.6}$$

Assuming there exists a steady state solution with amplitude of the form,

$$A(T) = ae^{i\sigma\tau} \equiv |a|e^{i\phi}e^{i\sigma\tau} \tag{D.7}$$

Substituting the equation D.7 into equation D.6 we obtain the frequency response equation to system D.3 of the form,

$$f = \left[\left(\frac{3}{4}|a|^2 - 2\sigma\right) + i\left(1 + \frac{\eta}{4}|a|^2\right)\right]a \tag{D.8}$$

The amplitude and phase of the response are then given by,

$$|a|^2 = \frac{g^2}{\left(2\sigma - \frac{3}{4}|a|^2\right)^2 + \left(1 + \frac{\eta}{4}|a|^2\right)^2} \tag{D.9}$$

$$\tan\phi = \frac{1 + \frac{\eta}{4}|a|^2}{2\sigma - \frac{3}{4}|a|^2} \tag{D.10}$$

The solution to the first order approximation to system D.3 is given by,

$$x(\tau) = \epsilon^{1/2} a\cos(\Omega\tau + \phi) + \mathcal{O}(\epsilon^{3/2}) \tag{D.11}$$

Rescaling the above equations in terms of physical parameters using table D.1, we obtain the physical solution as follows,

$$\tilde{x}(t) = \tilde{x}_0 \cos(\omega t + \phi)$$

where,

$$\tilde{x}_0 = a\sqrt{\frac{c_1\omega_0}{k_3}}$$

The amplitude and phase are given by,

$$\tilde{x}_0^{\;2} = \frac{\left(\frac{F}{2m\omega_0}\right)^2}{\left(\frac{\omega-\omega_0}{\omega_0}\right)^2 + \left(\frac{1}{2Q} + \frac{1}{8}\frac{c_2}{m\omega_0}\tilde{x}_0^{\;2}\right)^2} \tag{D.12}$$

$$\tan\phi = \frac{\frac{c_1}{2} + \frac{c_2}{8}\tilde{x}_0^{\;2}}{m\omega - m\omega_0 - \frac{3k_3}{8\omega_0}\tilde{x}_0^{\;2}} \tag{D.13}$$
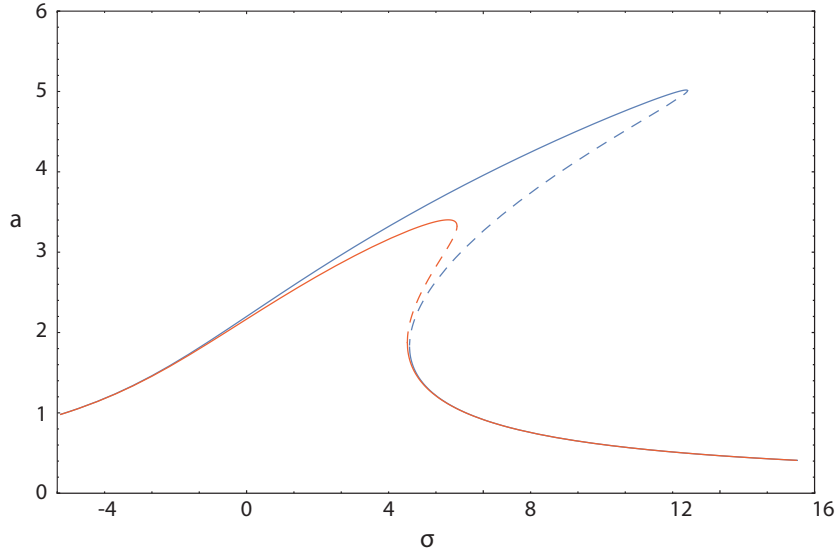
Figure D.1: Frequency response of a Duffing oscillator with (red curve) and without (blue curve) nonlinear damping

The scaled response function D.9 is plotted in figure D.1 without and with nonlinear damping. Due to the stiffening Duffing nonlinearity, the curves bend towards the right as the driving amplitude increases. The response amplitude of a driven resonator therefore increases with increasing frequency until it reaches a saddle node bifurcation point and drops abruptly to zero.

When the drive amplitude is f is sufficiently strong, we can use equation D.8 to find the bifurcation points, where the number of solution changes. These are the points of vertical tangencies which are obtained using the condition that $\frac{d\sigma}{da^2} = 0$. This yields a quadratic equation in σ which is solved to obtain the frequencies at which bifurcations occur.

$$\sigma^{\pm} = \frac{3}{4}|a|^2 \pm \frac{1}{2}\sqrt{\frac{3}{16}(3-\eta^2)|a|^4 - \eta|a|^2 - 1} \tag{D.14}$$

From the equation D.8, a linear stability analysis shows that two branches (upper and lower) are stable and a middle branch ($\sigma^- < \sigma < \sigma^+$) is unstable. When the drive amplitude is decreased sufficiently, one can see that these two bifurcation points merge into an inflection point. The critical drive amplitude for creating an instability or in other words the critical force required to obtain a Duffing response in presence of nonlinear damping is given by equation D.15 and is shown in figure. D.2. It can be seen from the figure that the critical amplitude required for having a bistable region increases with η ,

$$f_c = \frac{32}{27}\frac{9+\eta^2}{(\sqrt{3}-\eta)^3} \tag{D.15}$$

Thus from the above equation we see that for nonlinear damping $\eta > \sqrt{3}$, the equation D.14 always has a negative discriminant thus prohibiting the existence of bistable region.
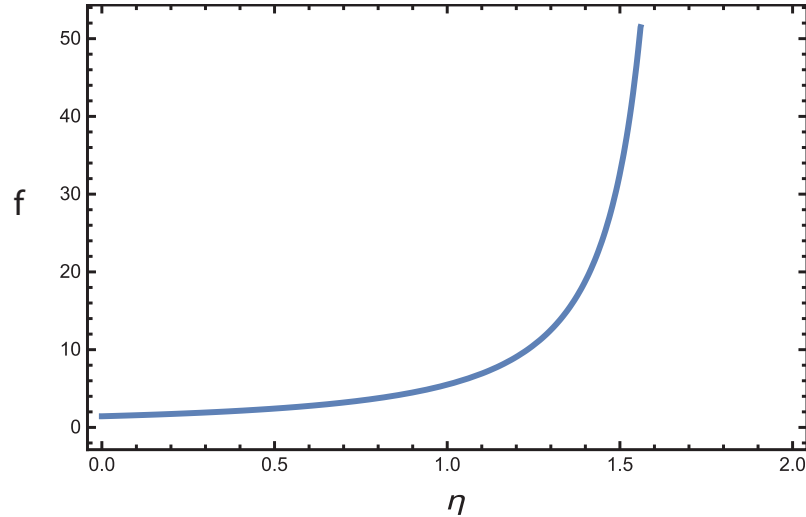
Figure D.2: Critical driving amplitude f_c for the onset of bistability in the response of Duffing oscillator as a function of nonlinear damping η

D.1.2. EFFECT OF NONLINEAR DAMPING ON THE RESPONSE AMPLITUDE

As seen from equation D.9 , when the nonlinear damping is appreciable it gives rise to an effective damping rate for oscillations with magnitude (a) given by,

$$C_{eff} = 1 + \frac{1}{4}\eta a^2$$

In terms of physical parameters,

$$C_{eff} = c_1 + \frac{1}{4}c_2 \tilde{x}_0^2$$

When looking at response given in Figure D.1, it is difficult to distinguish between the contributions of linear and nonlinear damping to the overall response of the system. The resonance peaks still lie on the same backbone regardless of the presence of nonlinear damping. Hence in order to distinguish between the effects of linear and nonlinear damping, one has to look at the responsivity function of the resonator which is defined as the amplitude scaled with respect to the direct drive *f*. From figure D.3 it is seen that without nonlinear damping all the curve has their peaks at the same height of 1.0. In the presence of nonlinear damping, there is a clear decrease in the responsivity as the forcing amplitude is increased. This is shown in figure D.4.
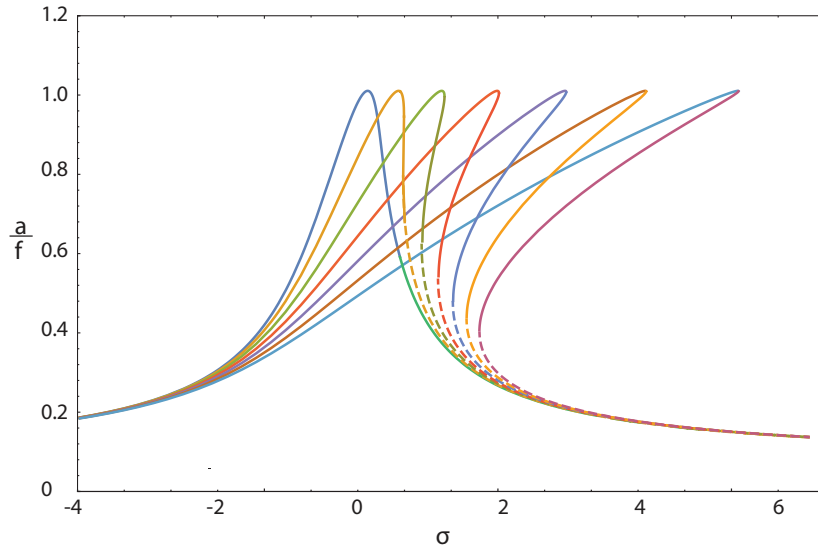
Figure D.3: Responsivity $\frac{a}{f}$ without nonlinear damping.
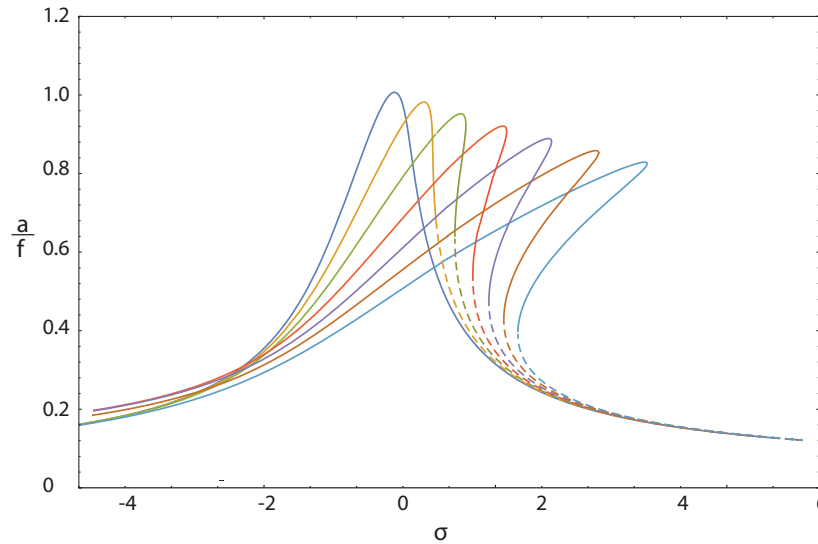
Figure D.4: Responsivity $\frac{a}{f}$ with nonlinear damping.

D.2. Dynamics of Parametrically Driven Duffing Oscillator with Nonlinear Damping

In this section, we study the dynamics of a Duffing oscillator with nonlinear damping which is actuated parametrically. The equation of motion of such a system is given by,

$$m\ddot{\tilde{x}} + c_1\dot{\tilde{x}} + k\tilde{x} + F_p\cos(\omega_p t)\tilde{x} + k_2\tilde{x}^2 + c_2\tilde{x}^2\dot{\tilde{x}} + k_3\tilde{x}^3 = F\cos\omega_d t \tag{D.16}$$

where, F_p is the strength of the parametric drive. ω_p and ω_d are the parametric and direct external excitation frequencies also called pump and drive frequencies. In the case of optically actuated resonators we have $\omega_p = \omega_d = \omega$. But in order to understand the dynamics better in the following section different detunings are introduced. The equation of motion is scaled as shown in section D.1 which leads to the dimensionless equation of motion,

$$\ddot{x} + Q^{-1}\dot{x} + x[1 + f_p \cos(\Omega_p \tau)] + x^2 + \eta x^2 \dot{x} + x^3 = f \cos(\Omega_d \tau) \tag{D.17}$$

Where, $f_p = \frac{F_p}{k}$ is the scaled parametric drive amplitude. $\Omega_p = \frac{\omega_p}{\omega_0}$ is the nondimensional parametric pump frequency and $\Omega_d = \frac{\omega_d}{\omega_0}$ is the nondimensional direct drive frequency.

D.2.1. Dynamics Analysis of Equation of Motion using Averaging Methods

The approach to obtaining a solution to equation D.17 follows the same procedure as shown in section D.1. In order to study the effect of nonlinear damping on parametric resonance, we look at the dynamics of the above equation at its largest excitation effect, this occurs when the parametric pump frequency is exactly twice that of the natural frequency of the graphene resonator. Taking the pump frequency to be an amount $\epsilon\sigma_p$ away from twice the resonant frequency and taking the parametric drive amplitude to scale as the damping i.e $f_p = \epsilon\delta$. Furthermore, on the right hand side of the equation, the direct drive frequency is taken to be an amount $\epsilon\sigma_d$ away from the resonant frequency and the direct drive amplitude is scaled as shown in section D.1. Representing the above mathematically,

$$\ddot{x} + \epsilon\dot{x} + x[1 + \epsilon\delta\cos((2 + \epsilon\sigma_p)\tau)] + x^2 + \eta x^2\dot{x} + x^3 = \epsilon^{3/2} f \cos((1 + \epsilon\sigma_d)\tau + \phi) \tag{D.18}$$

Where, ϕ is the phase difference between the direct and parametric excitation. Following the same procedure as in section D.1, the standard solution to the equation D.18 is assumed to be of the form,

$$x(\tau) = \frac{\sqrt{\epsilon}}{2}(A(T)e^{i\tau} + c.c.) + \epsilon^{3/2} x_1(\tau) + ... \tag{D.19}$$

Where, c.c. represents complex conjugate and the time scale T is given by $T = \epsilon\tau$. A(T) represents the slowly varying amplitude used to ensure that the higher order corrective terms don't diverge at singularities. By assuming the direct drive to be turned off i.e, f = 0 and substituting the equation D.19 in to equation D.18 and grouping the terms of $\epsilon^{3/2}$ we have,

$$\ddot{x}_1 + x_1 = \left(-iA' - i\frac{1}{2}A - \frac{3+i\eta}{8}|A|^2 A + \frac{f}{2}e^{i\sigma T} - \frac{1}{4}\right)e^{i\tau} - \frac{1+i\eta}{8}A^3 e^{3i\tau} + c.c. \tag{D.20}$$

In the above equation, the terms corresponding to $e^{i\tau}$ act like forces driving the system into resonance. These are called *secular terms* and by requiring that these terms equal to zero a *solvability condition* is imposed on the system which causes the solution to converge. The slowly varying amplitude is obtained from solvability condition as follows,

$$-iA' - i\frac{A}{2} - i\frac{\delta}{4}A * e^{i\sigma_p T} - \frac{3+i\eta}{8}|A|^2 A + \frac{f}{2}e^{i\sigma_d T} = 0 \tag{D.21}$$

Where, $A^* = A\cos((2 + \sigma_p)\tau)$ Assuming there exists a steady state solution with amplitude of the form,

$$A(T) = ae^{i\frac{\sigma_p}{2}\tau} \equiv |a|e^{i\phi}e^{i\frac{\sigma_p}{2}\tau} \tag{D.22}$$

Substituting the equation D.22 into equation D.21, we obtain the frequency response equation to system D.18 of the form,

$$\frac{-\delta a*}{2} = \left[\left(\frac{3}{4}|a|^2 - \sigma_p\right) + i\left(1 + \frac{\eta}{4}|a|^2\right)\right]a \tag{D.23}$$

From the above equation, we see that zero motion state i.e., a = 0 is always a possible solution to the equation irrespective of the excitation frequency σ_p. The nontrivial response and phase equations are obtained from equation D.23 and are given by,

$$\frac{\delta^2}{4} = \left(\sigma_p - \frac{3}{4}|a|^2\right)^2 + \left(1 + \frac{\eta}{4}|a|^2\right)^2 \tag{D.24}$$

$$tan(2\phi) = \frac{1 + \frac{\eta}{4}|a|^2}{\frac{3}{4}|a|^2 - \sigma_p} \tag{D.25}$$

Figure D.5 shows the parametric response of a Duffing oscillator with nonlinear damping. As compared to figures in chapter 3 where the response amplitude grew exponentially with increasing excitation frequency, the parametric response amplitude with nonlinear damping saturates at a maximum frequency.
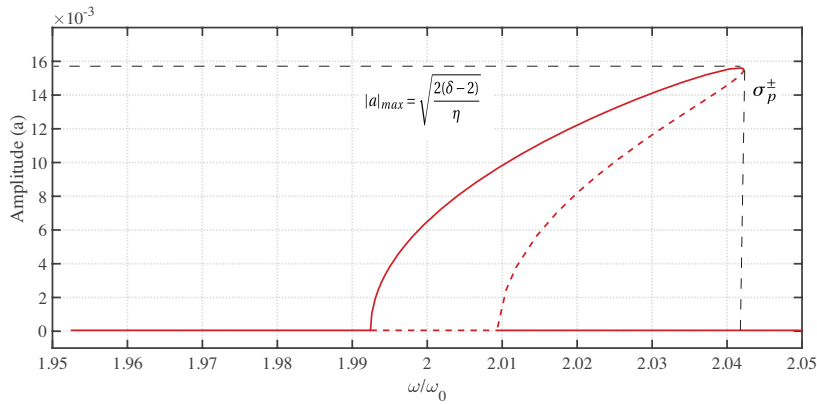
Figure D.5: Parametric response

This maximum peak amplitude and the corresponding frequency is given by,

$$|a|_{max} = \sqrt{\frac{2(\delta - 2)}{\eta}} \tag{D.26}$$

$$\sigma_p^\pm = \frac{\delta}{2}\sqrt{1 + \left(\frac{3}{\eta}\right)} - \frac{3}{\eta} \tag{D.27}$$

where, $\sigma_p^\pm$ indicates the points where the stable and unstable nontrivial solutions meet. From frequencies above $\sigma_p^\pm$ the only solution available is the zero amplitude solution, a = 0.

LINEAR INSTABILITY: CRITICAL PARAMETRIC DRIVE THRESHOLD FOR RESONANCE

The critical threshold required for linear instability to occur in parametrically excited system is calculated from equation D.24. In order to understand the underlying physics better the

main equation of motion D.18 is renormalized such that the linear damping coefficient (μ) is present along with the nonlinear damping (η) as follows,

$$\ddot{x} + \mu\dot{x} + x[1 + f_p\cos(\Omega_p\tau)] + x^2 + \eta x^2\dot{x} + x^3 = f\cos(\Omega_d\tau)$$

The equation D.24 now can be re-written as,

$$\frac{\delta^2}{4\mu^2} = \left(\frac{\sigma_p}{\mu} - \frac{3}{\mu}|a|^2\right)^2 + \left(1 + \frac{\eta}{\mu}|a|^2\right)^2 \tag{D.28}$$

The critical threshold parametric amplitude δ_{cr} required to push the system into linear instability is obtained by simply solving the above equation by substituting a=0. This leads to,

$$\delta > 2\mu = \frac{2}{Q} \tag{D.29}$$

The above equation is same as the expression obtained in chapter 3 section 3.3.2. This is an important result which shows that, the critical parametric drive threshold is mainly governed by the presence of linear damping in the system and nonlinear damping acts as a amplitude saturation nonlinearity. Without nonlinear damping and linear damping being small, one would have to go for higher orders of perturbation theory in search of physical mechanism that could provide such a saturation.

Accordingly as shown in chapter 3, by using a linear stability analysis an expression for period doubling bifurcations is given by,

$$\sigma_{PD} = \pm\sqrt{(\delta/2)^2 - 1} \tag{D.30}$$

The above result is the same as calculated in equation 3.25 for parametrically excited system with linear damping. Where σ_{PD} indicates the points where the trivial and nontrivial solutions meet.

D.3. Dynamics of Parametric Excitation at Second Instability Tongue

In this section, we study the dynamics of a Duffing oscillator with nonlinear damping which is actuated parametrically at it second instability tongue and look at the difference in dynamics with respect to the first instability tongue. The derivation closely follws the works of reference [60]. The equation of motion of such a system is given by,

$$m\ddot{\tilde{x}} + c_1\dot{\tilde{x}} + k\tilde{x} + F_p\cos(\omega_p)\tilde{x} + k_2\tilde{x}^2 + c_2\tilde{x}^2\dot{\tilde{x}} + k_3\tilde{x}^3 = F\cos\omega_d t \tag{D.31}$$

where, F_p is the strength of the parametric drive. ω_p and ω_d are the parametric and direct external excitation frequencies also called pump and drive frequencies colloquially. In the case of optically actuated resonators ($\omega_p = \omega_d = \omega$). But in order to understand the dynamics

better in the following section different detunings are introduced. The equation of motion is scaled as shown in section D.2 which leads to the dimensionless equation of motion,

$$\ddot{x} + Q^{-1}\dot{x} + x[1 + f_p \cos(\Omega_p \tau)] + x^2 + \eta x^2 \dot{x} + x^3 = f \cos(\Omega_d \tau) \tag{D.32}$$

Where, $f_p = \frac{F_p}{k}$ is the scaled parametric drive amplitude. $\Omega_p = \frac{\omega_p}{\omega_0}$ is the nondimensional parametric pump frequency and $\Omega_d = \frac{\omega_d}{\omega_0}$ is the nondimensional direct drive frequency.

D.3.1. Dynamics Analysis of Equation of Motion using Averaging Methods

The approach to obtaining a solution to the above equation of motion follows the same procedure as shown in section D.2. For parametrically excited systems the higher order instabilities are obtained at excitation frequencies,

$$\omega = \frac{\omega_0}{n} \tag{D.33}$$

Where n is an integer.

Hence, in order to study the dynamics at the second instability tongue the system is parametrically excited at a frequency $\omega = \omega_0$. Taking the pump frequency to be an amount $\epsilon \sigma_p$ away from the resonant frequency and taking the parametric drive amplitude to scale as the damping i.e $f_p = \sqrt{\epsilon} \delta$. Furthermore to simplify the dynamics the direct drive is assumed to be turned off i.e., $f_d = 0$. Representing the above mathematically,

$$\ddot{x} + \epsilon \dot{x} + x[1 + \sqrt{\epsilon} \delta \cos((1 + \epsilon \sigma_p)\tau)] + x^2 + \eta x^2 \dot{x} + x^3 = 0 \tag{D.34}$$

Following the same procedure as in section D.2, the standard solution to the equation D.34 is assumed to be of the form,

$$x(\tau) = \frac{\sqrt{\epsilon}}{2}(A(T)e^{i\tau} + c.c.) + \epsilon x_{1/2}(\tau) + \epsilon^{3/2} x_1(\tau) + ... \tag{D.35}$$

Where c.c. represents complex conjugate and the time scale T is given by $T = \epsilon \tau$. A(T) represents the slowly varying amplitude used to ensure that the higher order corrective terms don't diverge at singularities. Substituting the equation D.4 in to equation D.34 and grouping the terms of $\epsilon^{3/2}$ we obtain an expression for the secular terms (solvability condition) from which the amplitude A(T) can be determined. The solvability condition is given by,

$$iA' + i\frac{A}{2} + i\frac{\delta^2}{8}\left(\frac{2}{3}A + A * e^{i2\sigma_p T}\right) - \frac{3 + i\eta}{8}|A|^2 A = 0 \tag{D.36}$$

Where, $A* = A\cos((1 + \sigma_p)\tau)$ and $A' = \frac{dA}{dT}$

Assuming there exists a steady state solution with amplitude of the form,

$$A(T) = ae^{i\sigma_p \tau} \equiv |a|e^{i\phi}e^{i\frac{\sigma_p}{2}\tau} \tag{D.37}$$

Substituting the equation D.37 into equation D.36 we obtain the frequency response equation to system D.34 of the form,

$$\frac{-\delta^2 a*}{2} = \left[\left(\frac{3}{4} |a|^2 - 2\sigma_p - \frac{\delta^2}{6} \right) + i \left(1 + \frac{\eta}{4} |a|^2 \right) \right] a \qquad \text{(D.38)}$$

From the above equation we see that zero motion state i.e a = 0 is always a possible solution to the equation irrespective of the excitation frequency σ_p. The nontrivial response and phase equations are obtained from equation D.38 and are given by,

$$\frac{\delta^4}{16} = \left(\frac{3}{4} |a|^2 - 2\sigma_p - \frac{\delta^2}{6} \right)^2 + \left(1 + \frac{\eta}{4} |a|^2 \right)^2 \qquad \text{(D.39)}$$

$$tan(2\phi) = \frac{1 + \frac{\eta}{4} |a|^2}{\frac{3}{4} |a|^2 - 2\sigma_p} \qquad \text{(D.40)}$$

The amplitude has the form of a distorted ellipse in the (σ_p, a^2) plane.

D.3.2. Comparison of Frequency Response of a Parametrically Excited System at First and Second Instability Tongues

In this section, we look at the dynamic response of the system excited at first and second instability tongues. Figure D.6 shows the nontrivial dynamic response of a system excited at its first instability tongue given by the amplitude equation D.24. Figure D.7 shows the nontrivial dynamic response of a system excited at its second instability tongue given by the amplitude equation D.39. It can be seen that although the dynamics look similar a closer look reveals a difference in slope of the ellipse.
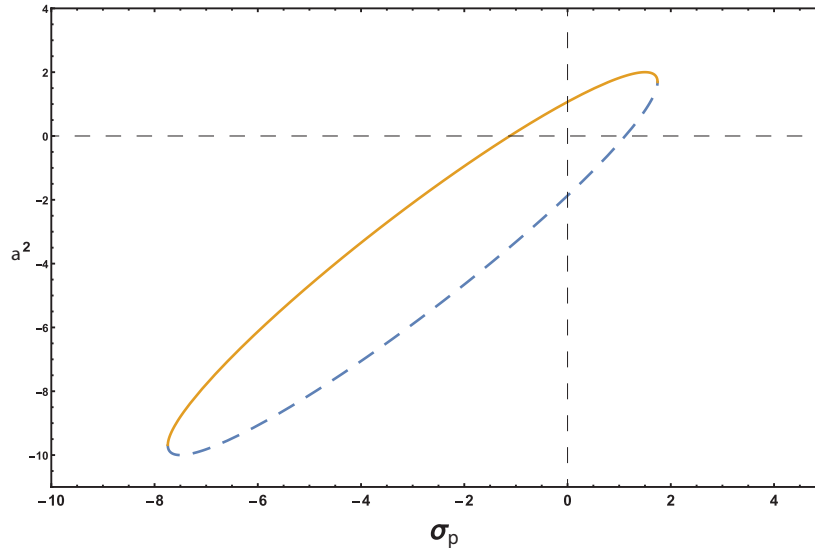
Figure D.6: Dynamic response of a parametrically excited system at first instability tongue
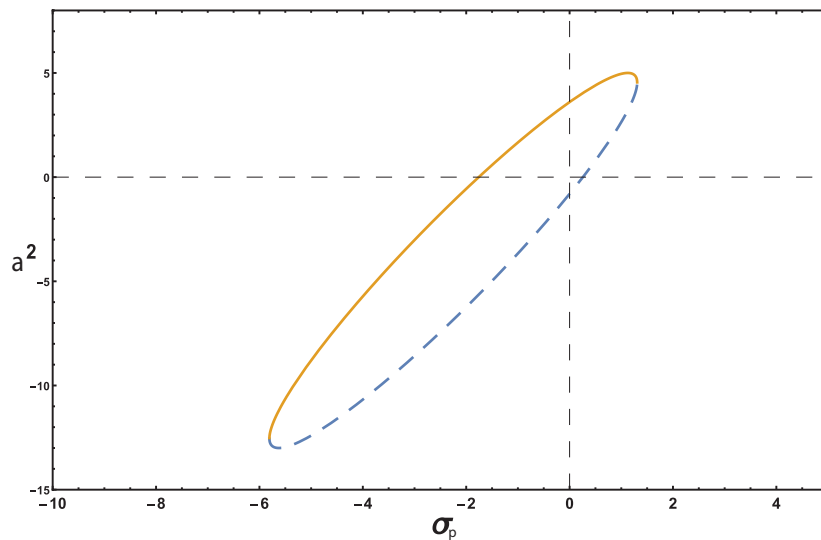
Figure D.7: Dynamic response of a parametrically excited system at second instability tongue

Equations D.24 and D.39 represent only the nontrivial part of the solutions. But it is much more interesting to study the combination of both trivial and nontrivial solutions. Hence in figure D.8 and D.9, we look at the part of the response where both trivial and nontrivial solutions interact. In this figure the difference in slope along with the difference in the response amplitude becomes apparent for the $\eta = 0$ case indicated by black lines. Again figures D.8 and D.9 represents the responses taken at first and second instability tongues.
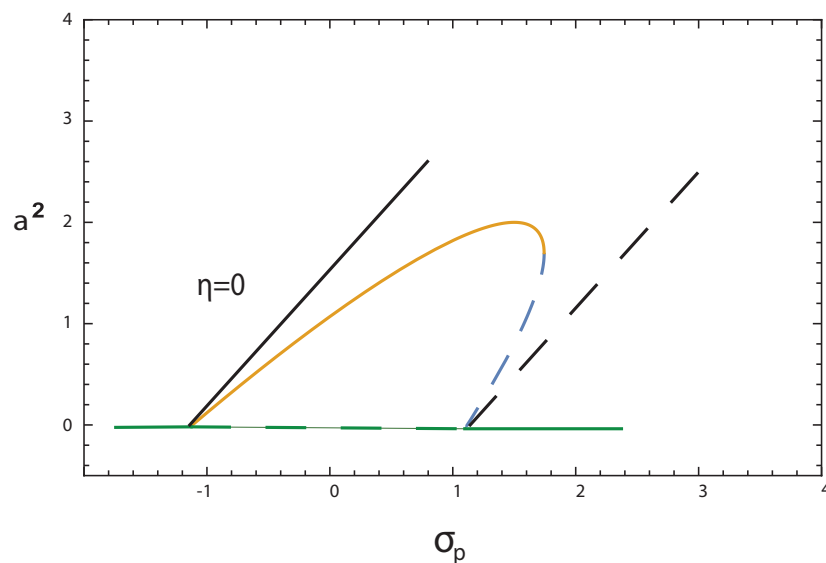
Figure D.8: Trivial and nontrivial response of a parametrically excited system at its first instability tongues. The black lines indicate solution with zero nonlinear damping ($\eta = 0$).
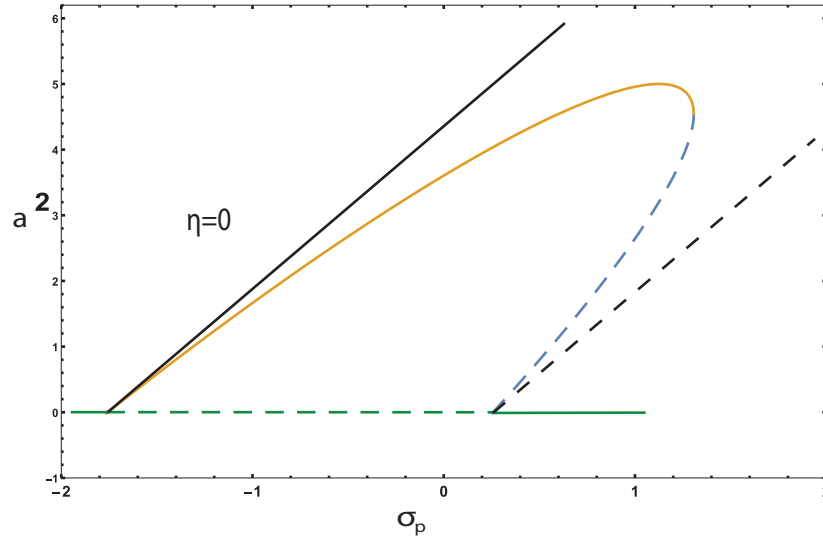
Figure D.9: Trivial and nontrivial response of a parametrically excited system at its first instability tongues. The black lines indicate solution with zero nonlinear damping ($\eta = 0$)

There are mainly two important difference in the responses shown above. The first is that the orientation of the ellipse, indicated by the slope of the curves for $\eta = 0$, is different. The slope for response at second instability tongue is 8/3, whereas for the first instability tongue the slope is 4/3. The second is that f_p scales as the square root of the linear damping rate μ. This is consistent with the well known result that the minimal amplitude for the instability of the nth tongue scales as $\mu^{1/n}$.

D.4. Simulation of Parametric Resonance at Second Instability Tongue in Graphene Nanodrum resonators

In this section a brief insight is provided regarding the parametric excitation at second instability tongue. The Duffing-Mathieu model with nonlinear damping given by equation 5.13 is used for simulation. Excitation at second instability tongue is done by taking the excitation frequency the same as response frequency. i.e $\omega = \omega_0$. The simulations are carried out with the same coefficient values used for fitting the experimental response obtained at $V_{rms} = 0.4462$ V in section 5.6.

The equation of motion is given by,

$$\ddot{x} + \epsilon\dot{x} + x[1 + \sqrt{\epsilon}\delta\cos((1 + \epsilon\sigma_p)\tau)] + x^2 + \eta x^2\dot{x} + x^3 = 0$$

Where, ϵ is a perturbation parameter. Figure D.10 shows the frequency response of a parametrically excited system at its second instability tongue. Although the dynamics looks similar, the slope of the response differs by a factor of 2 when the nonlinear damping is turned off (η=0) as explained in section D.3.2. The period doubling bifurcation occurs around $\omega = 1 + \sigma$, σ being the external detuning.

Figure D.11 shows the transition curve or second instability tongue of the system. As seen from the figure the curve is not symmetrical as compared to the first instability tongue
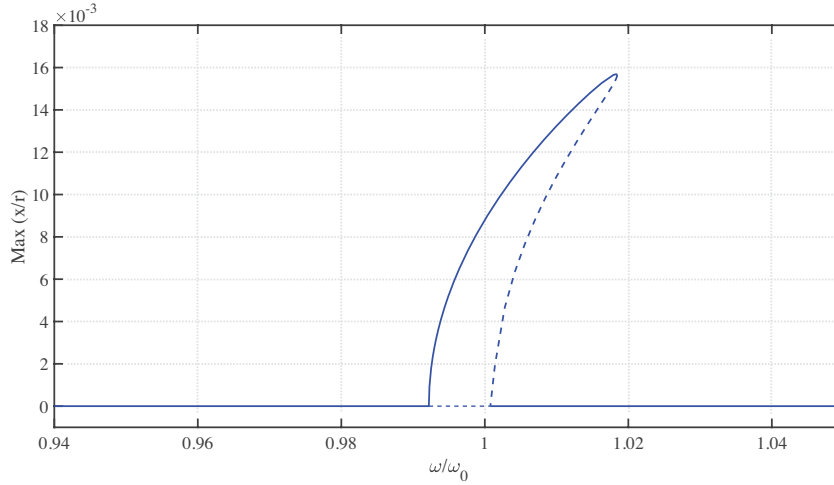
Figure D.10: Frequency response of a parametrically excited system at its second instability tongue.

seen in section 3.4. This is due to the fact that the strength of parametric drive required for creating linear instability grows proportional to $\sqrt{\mu}$, where μ is the linear damping present in the system. This is consistent with the well known result that the minimal amplitude for the instability of the nth tongue scales as $\mu^{1/n}$ and is in agreement with the theory discussed in section D.3.2.
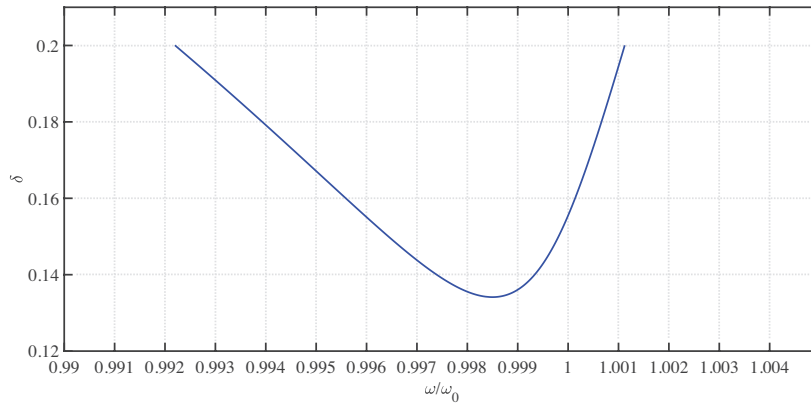
Figure D.11: Second instability tongue of a parametrically excited system

Although it is possible to theoretically simulate higher order parametric resonances, in reality it is much more difficult to excite such higher order resonances. The higher order instability regions grow thin as the order n increases and even a small amount of noise can knock the system out of instability. Furthermore, it is difficult to excite higher order parametric resonances in optically actuated graphene nanodrum resonators because the parametric and direct driving signals cannot be separated as compared to electrostatically actuated resonators.

D.5. CONCLUSION

In this chapter, dynamics of directly and parametrically driven Duffing resonator with nonlinear damping is studied. The equations of motion and the corresponding amplitude

and phase responses for both direct and parametric excitation are derived and elucidated based on secular perturbation theory. The effect of nonlinear damping on the responsivity of the direct resonance is delineated and the proportional relation between the direct driving amplitude and nonlinear damping is explained. The saturating effect of nonlinear damping on the amplitude of parametric response is explained through simulations and equations and shown to be in agreement with the experimental observations. Furthermore, the critical threshold amplitude required for linear instability is shown to be dependent only on the linear damping present in the system.

In the second half of the chapter, the dynamics of parametric excitation at second instability tongue is discussed and the equations governing the system are derived. A comparison is made between the response curves of first and second instability tongue and the significant differences are delineated. Furthermore, the resonance at second instability tongue is simulated for graphene resonators and is proved to agree with the theory. In the end conclusion is drawn on the limitation of optothermal actuation to excite higher order parametric resonances in experiments.

E

CURVE FITTING SECOND EXPERIMENTAL DATA SET

In this chapter, the theoretical fits for the second experimental data set is discussed. The Duffing and parametric experimental curves are given by figures E.1 and E.2 respectively.
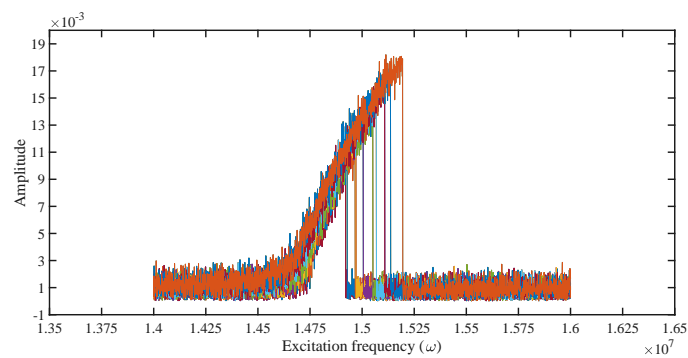
(a) Forward sweep
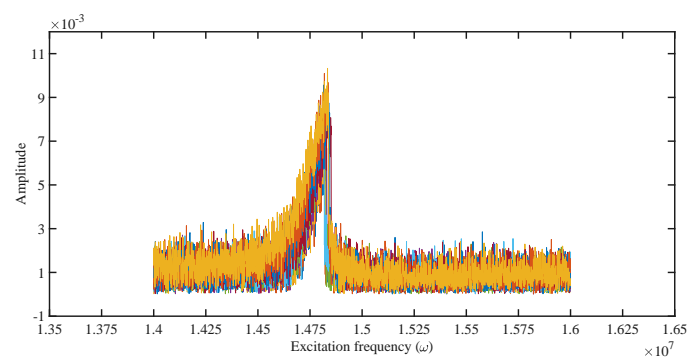
(b) Backward sweep.

Figure E.1: Duffing experimental response curves for second data set.
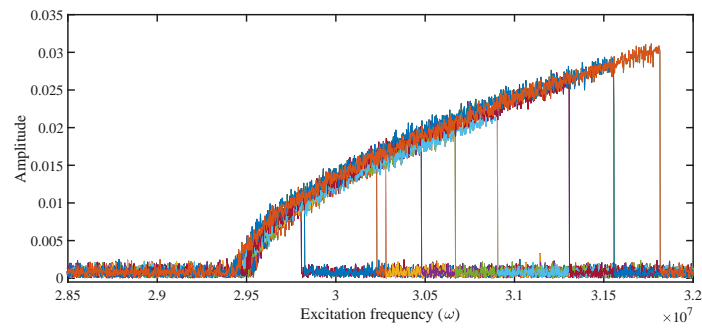
(a) Forward sweep
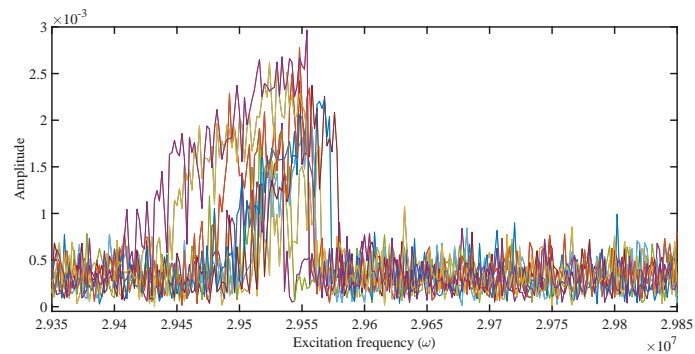
(b) Backward sweep.

Figure E.2: Parametric experimental response curves for second data set.

The Duffing-Mathieu model given by equation 5.13 is used to fit the experimental response obtained from a 5 micron diameter graphene nanodrum resonator with a fundamental frequency of $\omega_0 = 14.713$MHz.

Table E.1 shows the coefficients used in the equation of motion for fitting the experimental response curves. Here the subscript d and p represent the values used to fit the Duffing and parametric responses. It should be noted that the average values of $\nu = 35$ and $\gamma = 247$ can be used to fit the experimental response with reasonable accuracy. The maximum variation for the nonlinear damping coefficient (ν) is 10.8% and minimum variation is 2.7%. Similarly for cubic stiffness coefficient the maximum variation is 2.0 %. These variations are attributed to measurement inaccuracies.

Duffing response fit					Parametric response fit		
Curve at V_{rms} (V)	μ	ν_d	γ_d	$f \times 10^{-5}$	ν_p	γ_p	$\delta \times 10^{-2}$
0.1494	0.003	36	250	1.42	36	250	0.74
0.1677	0.003	37	245	1.6	36	250	1.01
0.1881	0.003	37	245	2.0	34	250	1.18
0.2111	0.003	37	245	2.5	34	250	1.31
0.2369	0.003	37	250	2.8	33	250	1.46
0.2658	0.003	36	250	3.3	34	245	1.81
0.2982	0.003	35	250	3.9	35	245	2.05
0.3346	0.003	35	250	4.5	35	250	2.25

Table E.1: Table of coefficients used for numerical simulation.

The dynamics is similar to as seen in section 5.6. Figure E.3 shows the simple harmonic response obtained at low driving power, an oscillator model is fitted to this curve to get an initial approximation of the quality factor of the system.
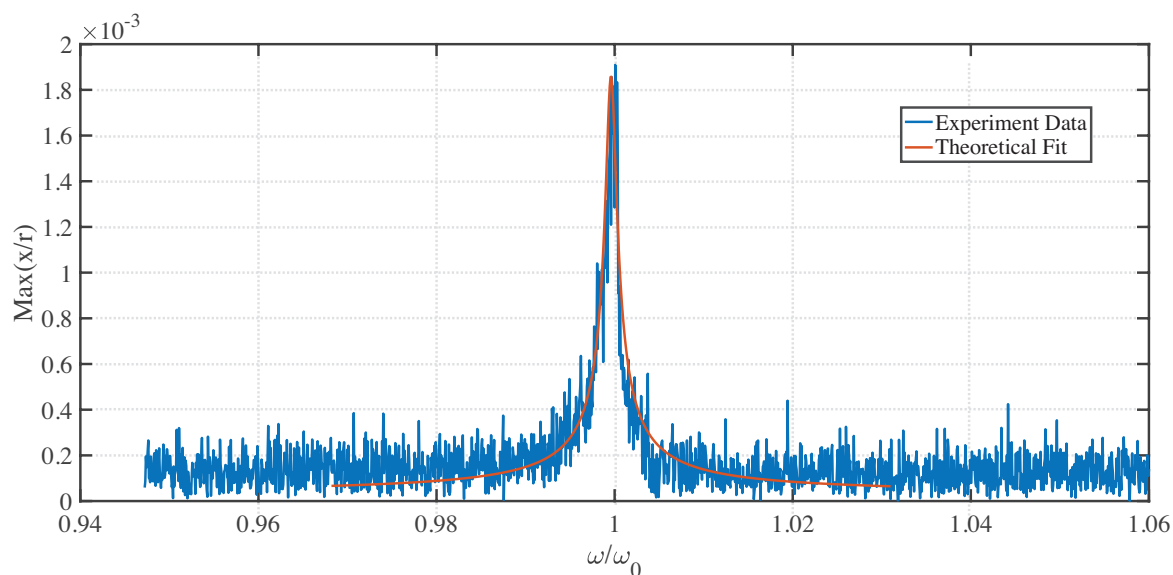
Figure E.3: Simple harmonic resonance at V_{rms}=0.0224 V

The theoretical fitting of large amplitude response curves are given by figures E.4, E.5, E.6, E.7, E.8, E.9, E.10, E.11. As seen from the figures, the model can fit the forward and backward sweeps of Duffing response with a high degree of accuracy at low powers. But the backward sweeps show a discrepancy with respect to the points of bifurcations. Similar to the first experimental data set, the theoretical model predicts a higher frequency jump in the response as compared to the experiments.
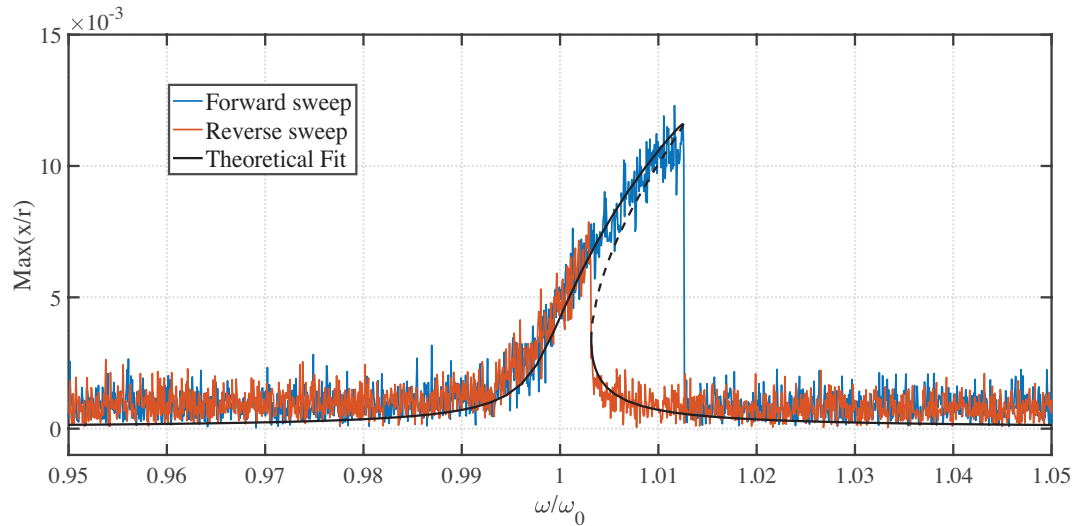
(a) Duffing response.
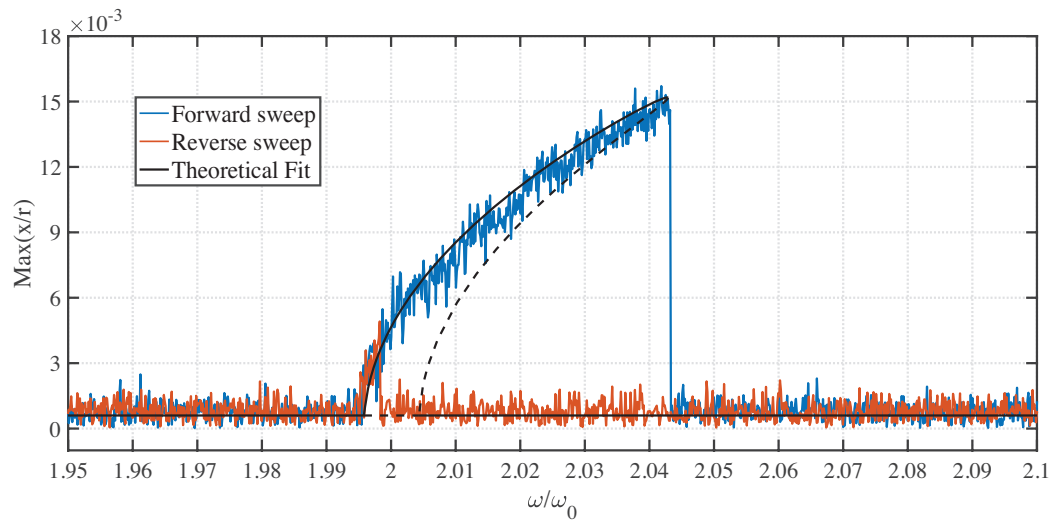
(b) Parametric response.

Figure E.4: Theoretical fit of experimental response at V_{rms}= 0.1494 V using Duffing-Mathieu model with nonlinear damping.
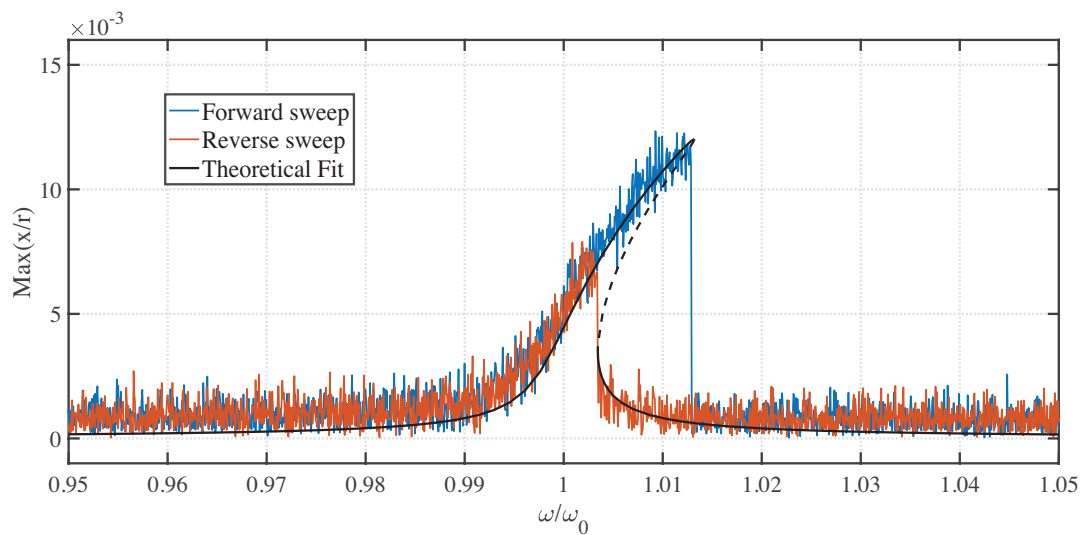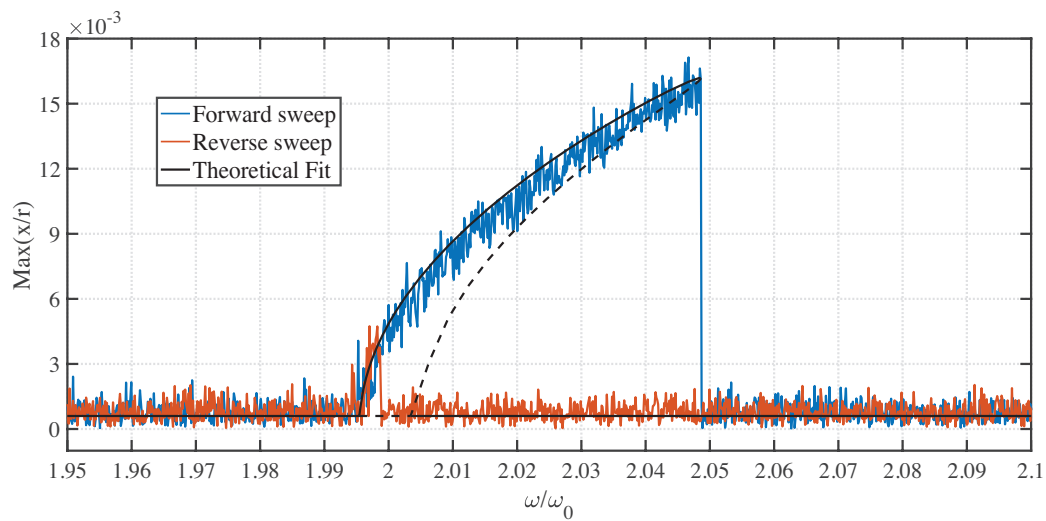
(a) Duffing response.

(b) Parametric response.

Figure E.5: Theoretical fit of experimental response at V_{rms} = 0.1677 V using Duffing-Mathieu model with nonlinear damping.
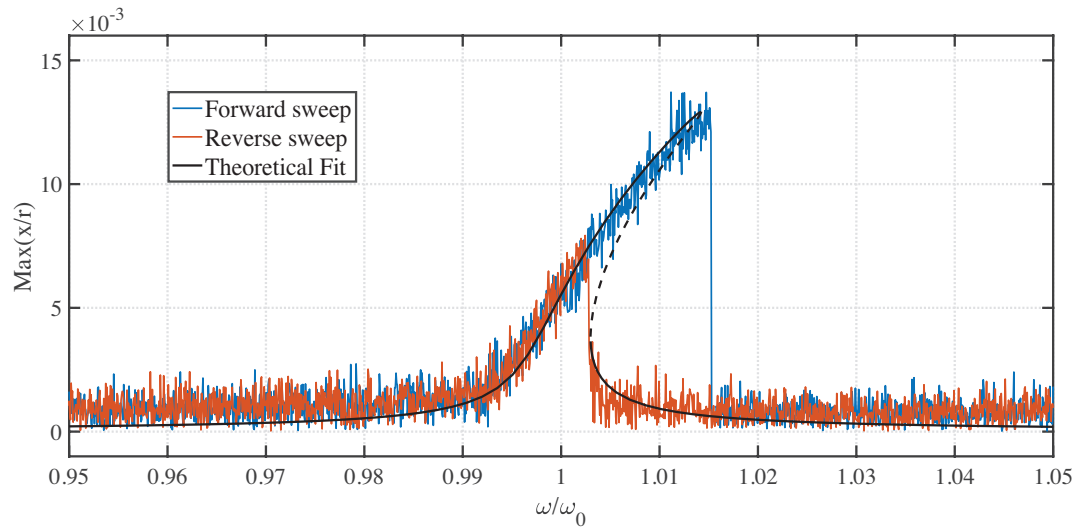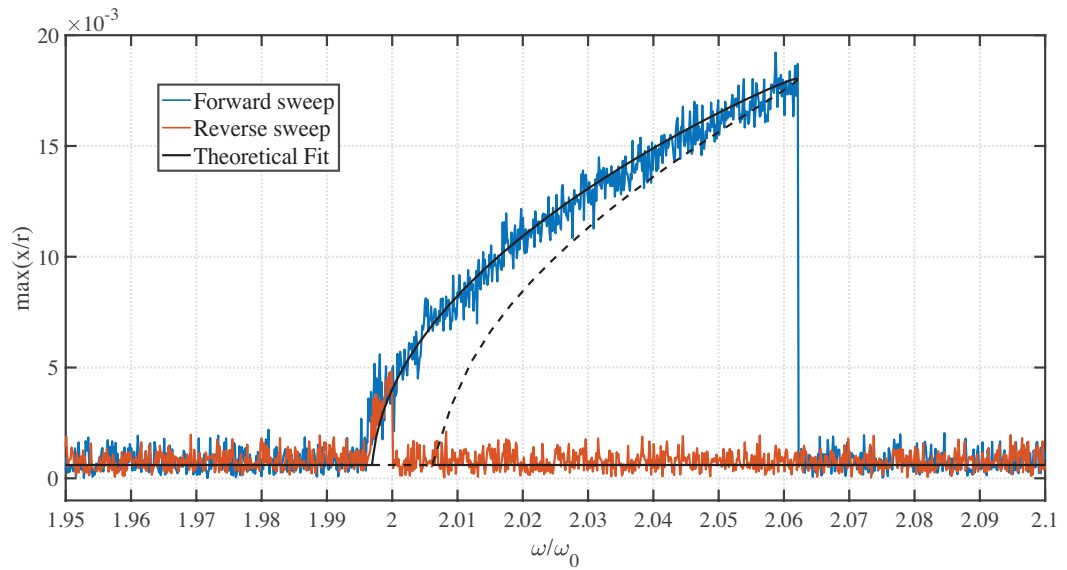
(a) Duffing response.

(b) Parametric response.

Figure E.6: Theoretical fit of experimental response at V_{rms}= 0.1881 V using Duffing-Mathieu model with nonlinear damping.
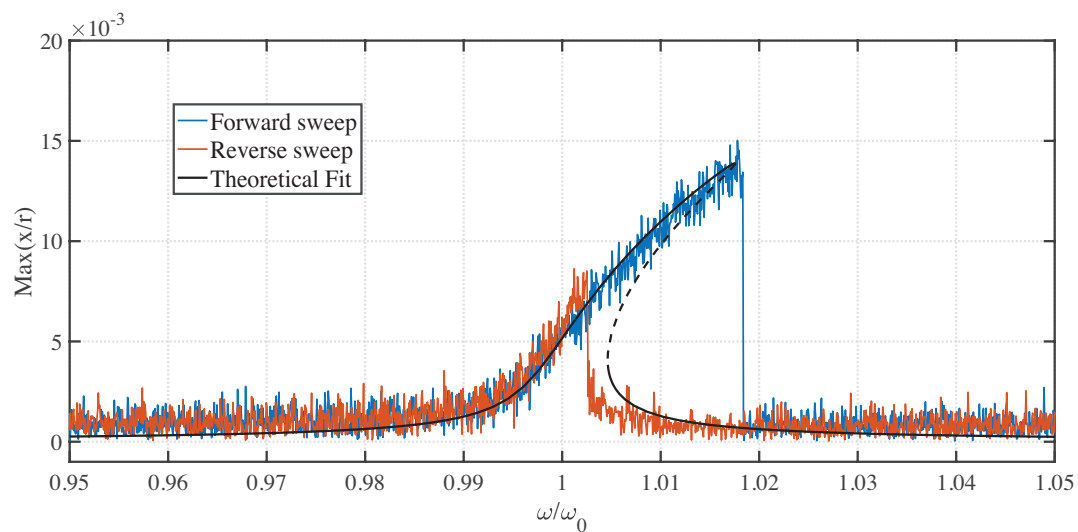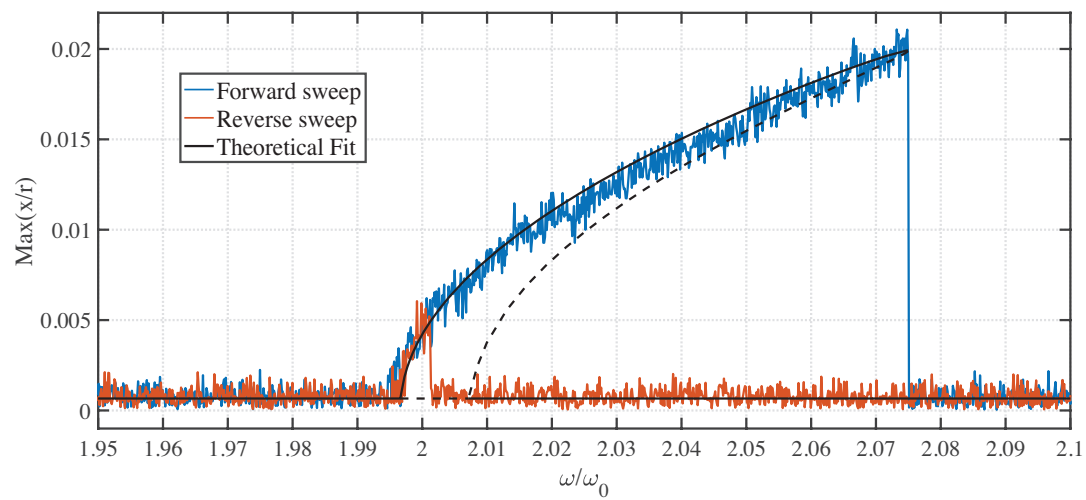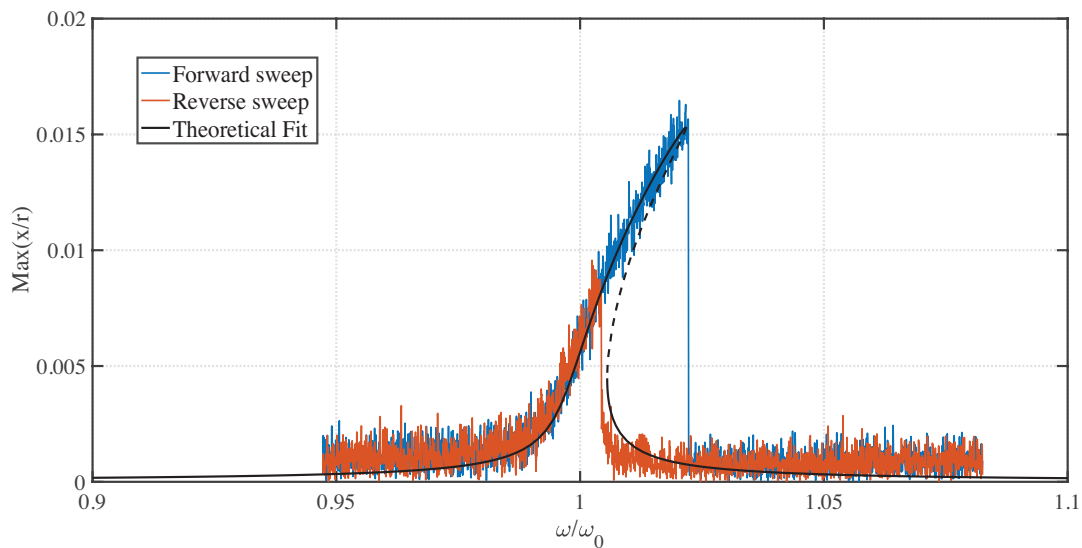
(a) Duffing response.

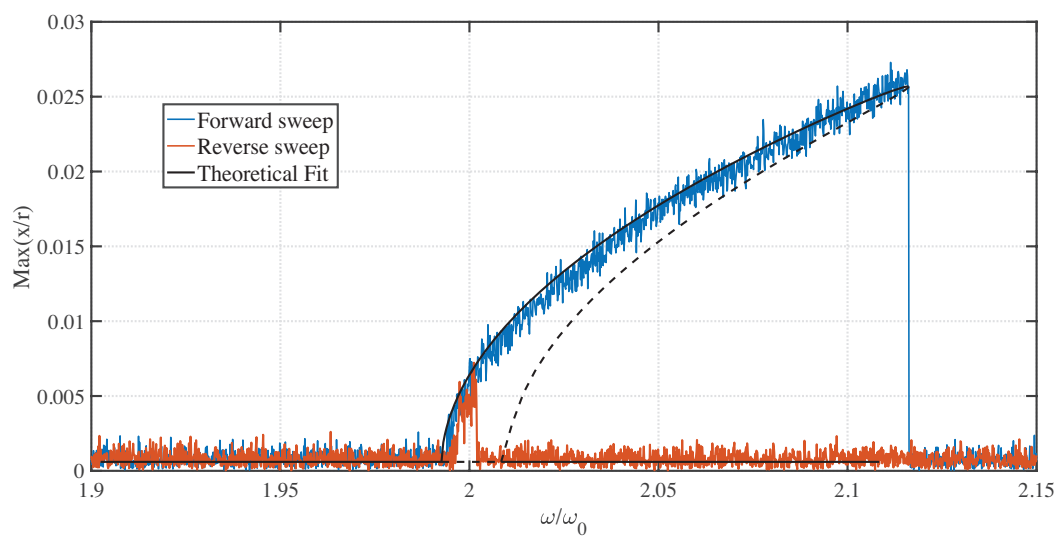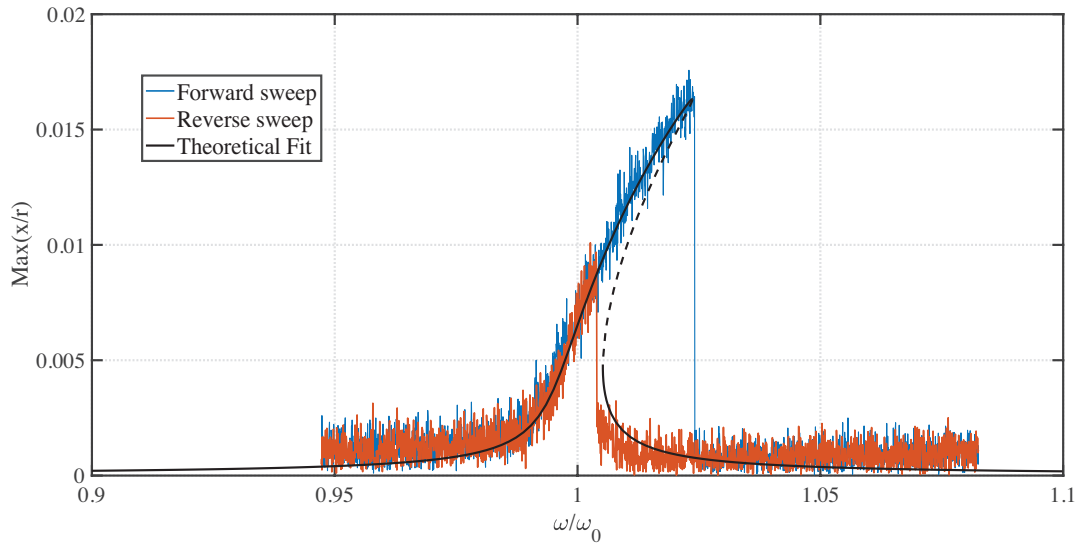(b) Parametric response.

Figure E.7: Theoretical fit of experimental response at V_{rms} = 0.2111 V using Duffing-Mathieu model with nonlinear damping.
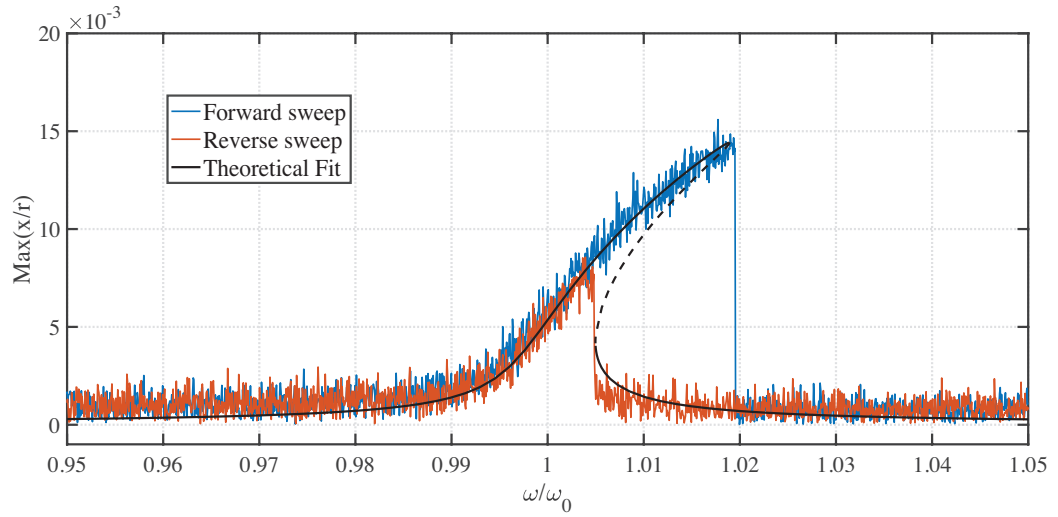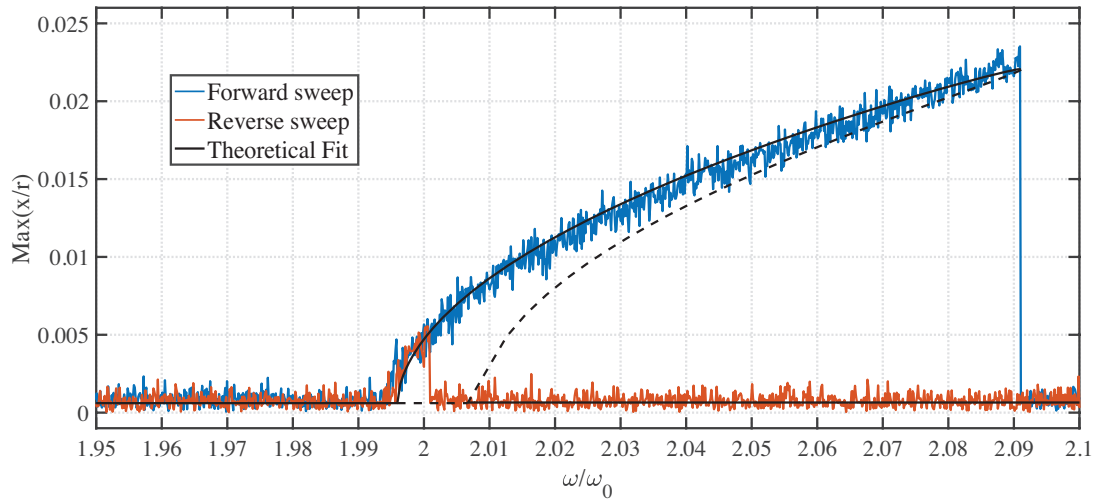
(a) Duffing response.

(b) Parametric response.

Figure E.8: Theoretical fit of experimental response at V_{rms}= 0.2369 V using Duffing-Mathieu model with nonlinear damping.
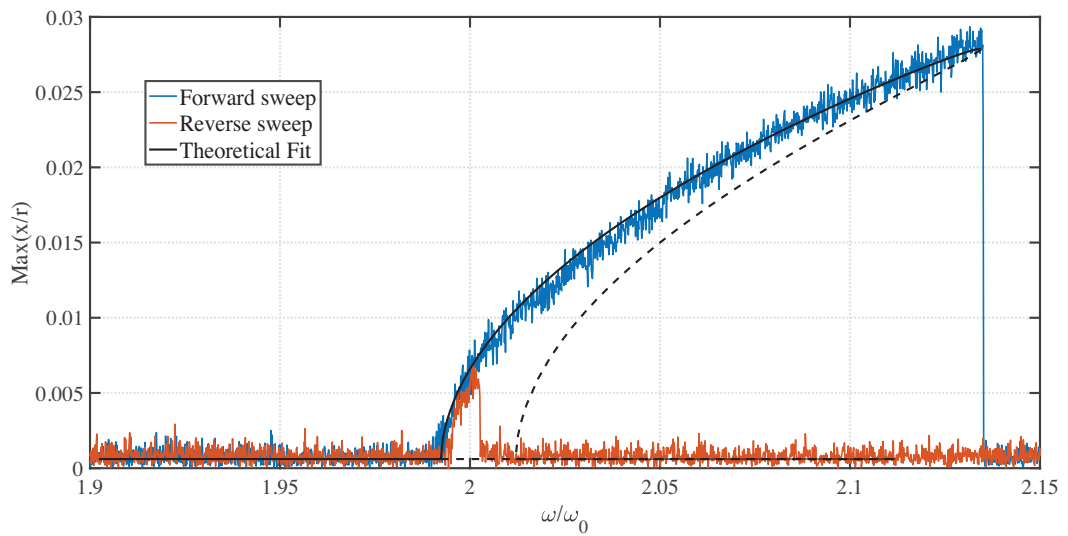
(a) Duffing response.

(b) Parametric response.

Figure E.9: Theoretical fit of experimental response at V_{rms}= 0.2658 V using Duffing-Mathieu model with nonlinear damping.
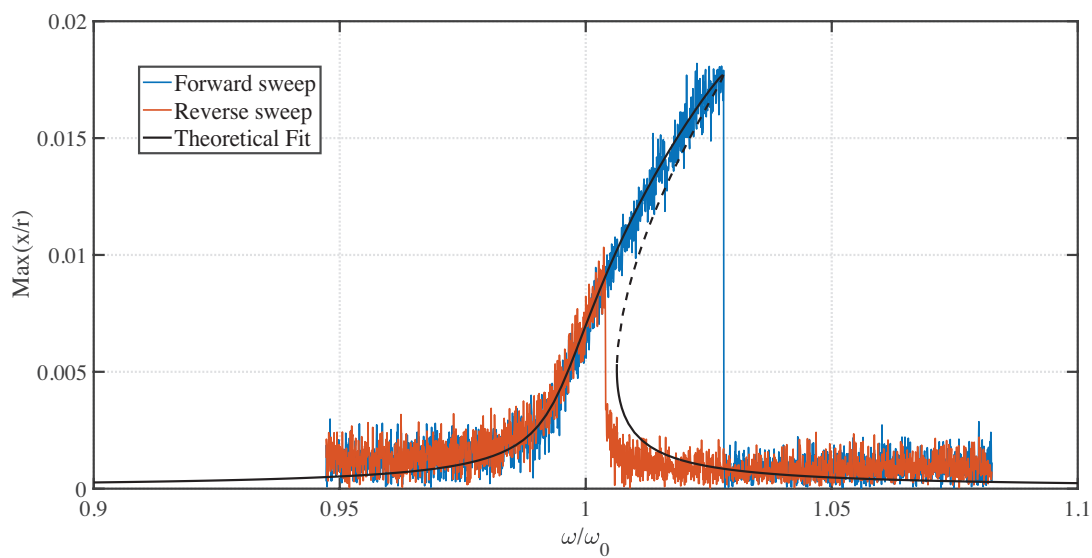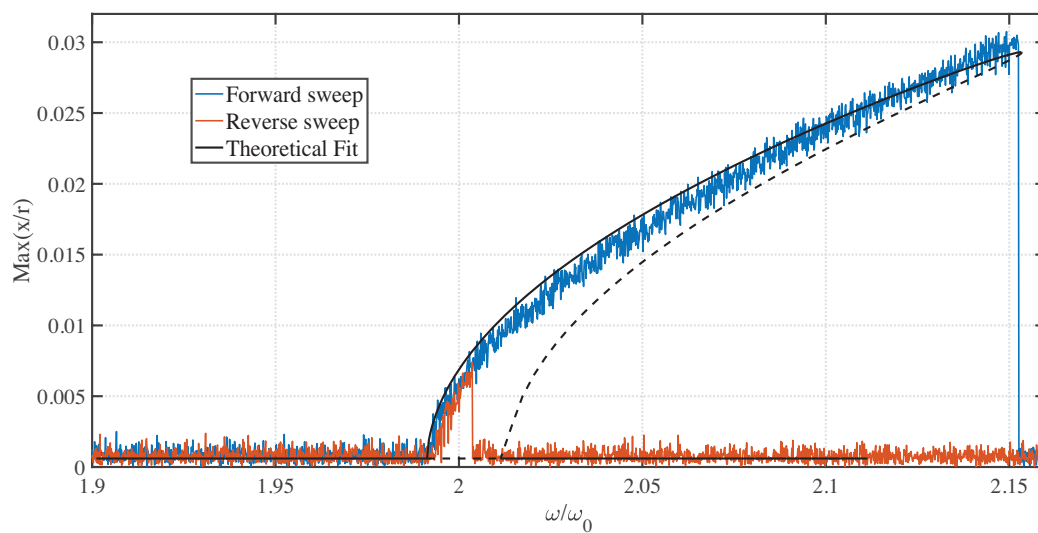
(a) Duffing response.

(b) Parametric response.

Figure E.10: Theoretical fit of experimental response at V_{rms}= 0.2982 V using Duffing-Mathieu model with nonlinear damping.

(a) Duffing response.

(b) Parametric response.

Figure E.11: Theoretical fit of experimental response at V_{rms}= 0.3346 V using Duffing-Mathieu model with nonlinear damping.